Faculty of Civil Engineering, Institute of Hydraulic Engineering and Technical Hydromechanics

PARAMETER STUDY OF A NUMERICAL DUNE EROSION MODEL UNDER EXTREME HYDRAULIC CONDITIONS ON THE BALTIC COAST

A Master's Thesis

In partial fulfilment of the requirements for the degree of

M.Sc. in Hydro Science and Engineering

Submitted by: Madhav Khatri
Matriculation Number: 5125523
Born on: 29.01.1998 in Arghakhanchi, Nepal

Supervisor: Dipl.-Ing. Dirk Fleischer (IWD)
First Examiner: Univ.-Prof. Dr.- Ing. Jürgen Stamm
Second Examiner: Dr.-Ing. Torsten Heyer

Date of Submission: 18.09.2025, Dresden

This page is intentionally left blank

TECHNISCHE UNIVERSITÄT DRESDEN

Fakultät Bauingenieurwesen — Institut für Wasserbau und Technische Hydromechanik

IWD Institut für Wasserbau und Technische Hydromechanik

Task sheet for Master Thesis

Name:	Madhav Khatri
Matriculation No.:	5125523
Study Course:	Hydro Science and Engineering

Topic: **Parameter study of a numerical dune erosion model under extreme hydraulic conditions on the Baltic coast**

Paramterstudie eines numerischen Dünenerosionsmodells unter hydraulischen Extrembedinungen an der Ostseeküste

Motivation and Objective:

As a peripheral sea of the North Sea with a complex bathymetry and frequently changing wind exposure, the Baltic Sea poses a significant challenge for coastal planning. Current climate projections also predict a sea level rise of 80-100 cm by the year 2100, which is expected to significantly increase the frequency of critical storm surges.

The research project ResCAD focuses on the hydromorphodynamic processes at coastal protection dunes along the Baltic Sea coastline of Mecklenburg-Western Pomerania, using numerical and statistical methods. Traditionally, coastal protection dunes are considered wearing structures, but due to their natural character, they can also be classified as a "nature-based solution." The prediction of required sand volumes and the development of optimized standard cross-sections are key topics of current research. Hydromorphodynamic models are used to simulate the development of a coastal section from time X1 (before a hydraulic event) to time X2 (after the event). The models used in ResCAD are based on statistically determined storm surge scenarios with variations in duration, water levels, and wave parameters.

The goal of this master's thesis is an in-depth analysis of the numerous simulation parameters at the Ahrenshoop site using the numerical simulation software XBeach, which is specifically designed to calculate hydraulic erosion processes caused by extreme events. Wave conditions, boundary conditions, and morphodynamic processes will be parameterized using different approaches and value ranges. The thesis aims to identify and systematically analyze complex relationships between these parameters.

Using the extensive literature on XBeach and the results of the simulations, the discussion will focus in particular on the influence of these parameters on dune erosion and erosion volumes. Additionally, the study will investigate the extent to which individual parameters can be aggregated into global parameters to simplify the calibration of local models.

Scope:

As part of the master's thesis, the following work packages are to be completed:

1. Research and training on the software to be used, focusing on:
   - XBeach simulation parameters for dune erosion models
   - Comparable projects, previous work conducted by the IWD, as well as relevant publications and studies
   - Data analysis and visualization using QGIS, MATLAB, or Python
2. Structuring and development of a simulation program
   - Implementation of an automated simulation workflow using the XBeach version (netCDF-MPI), including input and boundary conditions, control files, and computational grids (see also Windows PowerShell/Matlab)
   - Selection of simulation parameters and the value ranges to be investigated, based on sensitivity analysis, expert knowledge, and existing studies
3. Planned execution of the simulation workflows and organization of simulation results
4. Discussion of the results with recommendations for the selection of simulation parameters for comparable boundary conditions and objectives
5. Documentation of the workflows and preparation of the results in a scientific report (see template for theses provided by the IWD)

Clarifications regarding the scope of the tasks are to be coordinated regularly with the academic supervisor during the course of the project.

The data and information required for the study will be provided to the student by the supervisor but may be supplemented, if necessary, with well-justified assumptions.

Miscellaneous:

The report must be submitted in printed form in at least two copies to the Examination Office of the Department of Hydro Sciences at TUD Dresden University of Technology. Along with or after submitting the thesis, a poster (refer to the Poster IWD template) must be created in a digital format (PDF, PowerPoint). Additionally, a digital version of the thesis, including the digital appendix, must be made accessible (via the IWD server or USB). The guidelines for the master's thesis and examination regulations of the Department of Hydro Sciences at TUD, as well as the instructions of the supervising institute, must be followed. Furthermore, at least one consultation with the supervisor must be arranged every two weeks.

Supervisor, IWD:
Dipl.-Ing. Dirk Fleischer (IWD)

ausgehändigt am:

einzureichen bis:

Univ.-Prof. Dr.-Ing. Jürgen Stamm

First Examiner

Dr.-Ing. Torsten Heyer

Second Examiner

This page is intentionally left blank

Declaration of Independent Work

I hereby declare that this master's thesis is the result of my own work and has been completed independently, without the use of sources and aids other than those indicated. All sources of information used in this thesis have been properly cited and acknowledged.

Signature	.....
	Madhav Khatri
Location, Date:	Dresden, 18.09.2025

This page is intentionally left blank

Acknowledgements

I would like to express my deepest gratitude to my supervisor, Dipl.-Ing. Dirk Fleischer, for his continuous support and guidance throughout the course of this research. His expertise, insightful feedback and critical evaluation were instrumental in shaping this thesis and have significantly enhanced the quality of my work. I am also sincerely thankful to Dipl.-Ing. Matthias Ehrig for his valuable support at the computer pool during the initial stages of this study.

Furthermore, I extend my heartfelt appreciation to my parents, my sister Neeta, roommates and friends for their unwavering support throughout this journey. Their love, patience, and encouragement, especially during challenging times, have been my greatest source of strength.

Abstract

The Baltic Sea's complex bathymetry and shifting wind climate, together with projected sea-level rise (≈ 80 –100 cm by 2100) and increased storm-surge risk demand proper calibration of process-based dune-erosion models like XBeach. This thesis conducts a parameter study with XBeach (netCDF–MPI) at Ahrenshoop by varying grid and hydrodynamic parameters to assess morphodynamic responses. Fifty parameter sets were generated with Latin Hypercube Sampling (LHS) method across default ranges for *facua*, *gamma*, *gamma2* and *por*. Simulations were screened using the Brier Skill Score (BSS) to identify behavioural runs and the Generalized Likelihood Uncertainty Estimation (GLUE) framework was applied to assign likelihood weights, quantify parameter-induced uncertainty and rank sensitivities via the Kolmogorov–Smirnov D-statistic (K–SD). GLUE indicated *gamma* as most sensitive (K–SD = 0.389), followed by *facua* (0.195) and *gamma2* (0.175), though inference was limited by the small behavioural ensemble.

Because long runtimes (18 h/run) and crashes limited the number of simulations that could be completed, the workflow pivoted to one-at-a-time tests with grid optimisation and morphological acceleration (morfac = 15–20). Lower values of *facua* (≈ 0.16–0.17) raised BSS but intensified dune scarping. With morfac = 20, the best calibrated run reached BSS = 0.8081 (RMSE = 0.1676). The parameter *gamma* showed an optimum near 0.47–0.50, yielding the highest skill on the reduced grid (BSS = 0.8562; RMSE = 0.1526) while *gamma2* exerted secondary influence with credible values around 0.38–0.40. Directional resolution parameter (*dtheta*) showed best performance around 14°–16° whereas coarser *dtheta* (20°) degraded model performance. The angle with which the waves attack the model grid perpendicular to the shore normal (*theta*) was also varied and oblique angles consistently amplified erosion and alongshore redistribution till ± 40°. This study indicates that, for the Ahrenshoop sector of the Baltic Sea and under the tested storm conditions, the most credible calibration ranges are *facua* ≈ 0.12–0.16, *gamma* ≈ 0.50, and *gamma2* ≈ 0.38–0.40 with *morfac* = 15–20 and directional resolution (*dtheta*) of ≈ 14°−16°, yielding the best compromise between high BSS and physically realistic dune erosion.

Keywords: XBeach; dune erosion; sensitivity analysis; Baltic Sea; Coastal protection

This page is intentionally left blank

Bibliographic Record

Research Institution

Technische Universität Dresden
Faculty of Civil Engineering
Institute of Hydraulic Engineering and Technical Hydromechanics

Author: Madhav Khatri

Title of the Thesis:

Parameter study of a numerical dune erosion model under extreme hydraulic conditions on the Baltic coast

Paramterstudie eines numerischen Dünenerosionsmodells unter hydraulischen Extrembedinungen an der Ostseeküste

Year of Publication: 2025
Number of Pages: XXII, 110
Number of Figures: 71
Number of Tables: 18
Number of References: 64

Keywords: XBeach; dune erosion; sensitivity analysis; Baltic Sea; Coastal protection

Table of Contents

Declaration of Independent Work v

Acknowledgements vii

Abstract viii

Bibliographic Record x

List of Symbols xviii

List of Abbreviations xxi

1 Introduction 1

1.1 Sea Level Rise and Coastal Flooding . . . 1
1.2 Baltic Region and the German Baltic Coast . . . 2
1.3 Coastal Protection Approaches in Mecklenburg-Vorpommern . . . 4
1.4 Motivation and Objectives . . . 6
1.5 Structure of the Thesis . . . 7

2 Theoretical Background and Data 8

2.1 Description of Coastal Region . . . 8
2.2 Definition of a Wave . . . 10
2.3 Wave Classification . . . 12
2.4 Wave Transformation . . . 13
2.5 Coastal Morphodynamics in the German Baltic Sea . . . 15
2.6 Hydrodynamic Forcing in the Baltic Sea . . . 16
2.7 Storm Surges in the Baltic Sea . . . 16
2.8 Morphological and Hydrodynamic data . . . 17

3 Literature Review 19

3.1 Software and Simulations Program . . . 19
3.2 Hydrodynamics Options in XBeach . . . 20
3.3 XBeach Modules . . . 20
3.3.1 Flow Module . . . 20
3.3.2 Wave Module . . . 22
3.3.3 Sediment Transport Module . . . 25
3.3.4 Morphology module . . . 25
3.4 Sensitivity Analysis . . . 27
3.5 Latin Hypercube Sampling Method . . . 27
3.6 Selected XBeach parameters for this Study . . . 29

4 Methodology 31

4.1 Generalized Likelihood Uncertainty Estimation (GLUE) . . . 31
4.2 Parameter Sensitivity Analysis based on Statistics . . . 34
4.3 Generalized Sensitivity Analysis (GSA) . . . 34
4.4 XBeach Model Setup . . . 34
4.5 Pre-Processing Phase . . . 35

4.5.1 Topo Bathymetry 35
4.5.2 Grid Construction 35
4.6 Hydrodynamic Input 40
4.7 Specification of the Boundary Conditions 42
4.7.1 Specification of Offshore Wave Boundary Conditions 42
4.7.2 Specification of Flow Boundary Conditions 43
5 Results and Discussion **45**
5.1 Parameter Sensitivity Analysis based on Statistics 48
5.2 Application of GLUE Methodology for Sensitivity Analysis 50
5.3 Application of OAT Method 52
5.3.1 Variation of facua 53
5.3.2 Variation of gamma 57
5.3.3 Variation of gamma2 60
5.3.4 Change of morfac Value to 20 60
5.3.5 Change in Dimension of Model Grid 63
5.3.6 Variation of dtheta 66
5.3.7 Variation of Angle of Wave Incidence 72
6 Conclusion and Outlook **79**
6.1 Sensitivity based on Statistics 79
6.2 GLUE-based Parameter Sensitivity 79
6.3 Application of OAT Method 79
6.3.1 Variation of gamma and gamma2 80
6.3.2 Change of morfac Value to 20 80
6.3.3 Change in Dimension of Model Grid 81
6.3.4 Variation of dtheta 81
6.3.5 Variation of theta 81
6.4 Limitations 82
6.5 Conclusion 82
6.6 Outlook 83
References **85**
Appendices **90**
Appendix A: Script used for generating LHS samples 90
Appendix B: Script used for setting up the model 90
Appendix C: Parameter Combinations obtained from Latin Hypercube Sampling 103
Appendix D: Typical example of a `params.txt` file 104
Appendix E: Overview of simulation runs when facua, gamma and gamma2 were varied 107

Appendix F: Change of morfac to 20 109
Appendix G: Overview of the Simulations for varying dtheta 110
Appendix H: Results after varying angle of wave incidence (theta) 110

List of Figures

Figure 1.1 Annual averages of the water level at the WSA gauge in Rostock-Warnemünde (Saathoff et al., 2020) 2
Figure 1.2 Location of German Baltic coast in the world map 2
Figure 1.3 Coastline lengths of the state of Mecklenburg-Vorpommern. After (StALU, 2009). 3
Figure 1.4 Characteristic structure of a beach section protected by dunes and groynes. After (Fleischer, n.d.) 4
Figure 1.5 Methods of Coastal Protection. Standard cross-section of a dike (top) and standard cross-section of a full protection dune (bottom). After StALU (2009) 5
Figure 2.1 Schematization of the coastal region, including the positions of the various shoreface zones. After Dashtgard et al. (2012) 8
Figure 2.2 Plan view of the coastal area and the involved coastal processes (Bosboom & Stive, 2023) 9
Figure 2.3 The definition of a wave in a time record of the surface elevation with downward zero-crossings (upper panel) or upward zero-crossings (lower panel). After (Holthuijsen et al., 1989) 10
Figure 2.4 Simple representation of a wave 11
Figure 2.5 Particle paths illustrated for three different water depths. After Andersen & Frigaard (2011) 12
Figure 2.6 Classification of waves based on wavelength(top line), wave-generating force (middle line) and restoring force (bottom line). After Munk (1951) and Kinsman (1984). 13
Figure 2.7 Propagation of waves towards the surf zone. After Earle (2015) 13
Figure 2.8 Breaker types according to Battjes (1974). After Bosboom & Stive (2023) . . 14
Figure 2.9 Main coastal topographic features and the morphodynamic processes of erosion and accretion at the Baltic Sea shore. After Weisse et al. (2021) . . . 15
Figure 3.1 Component modules in XBeach. After Daly (2009) 19
Figure 3.2 XBeach wave model options (left) and Principal sketch of relevant wave processes (right) 21
Figure 3.3 Application area of XBeach by coastal section and type of energy transformation, where green color suggests suitability, red color suggests unsuitability 21
Figure 3.4 Visual representation of Latin Hypercube Sampling. After (Arkel, 2016) . . . 28
Figure 4.1 Flow chart of GLUE process. After Bae et al. (2022) 31
Figure 4.2 Methodology adopted for the initial set of simulations 33

Figure 4.3 Stages of Modeling in XBeach. After Abdelaal & Oumeraci (2016) 35
Figure 4.4 Basic concept of computational grids in XBeach, adapted from ResCAD A . 36
Figure 4.5 Observation of grid fitting with Matlab 38
Figure 4.6 Hydrodynamic criteria for minimum water depth. Left: Significant wave height ∼ 2.5 m, right: Peak period ∼ 10 s. After ResCAD project 38
Figure 4.7 Extended and optimized computational grid 39
Figure 4.8 Constructed bathymetry (size varying) from existing measurement data in 3D 40
Figure 4.9 Modified and expanded bathymetry in 3D 40
Figure 4.10 Hydrodynamic input used in the simulation 41
Figure 4.11 Mean wave directions over time 42
Figure 4.12 Study area with bathymetry and boundary conditions 43
Figure 5.1 Cross-sectional profile for facua = 0.02, gamma= 0.783, gamma2 = 0.494 and por = 0.42 (n = 144) 46
Figure 5.2 Cumulative erosion / sedimentation at the end of simulation for facua = 0.02, gamma= 0.783, gamma2 = 0.494 and por= 0.42 47
Figure 5.3 Cross-sectional profile for facua = 0.2854, gamma = 0.7716, gamma2 = 0.2985 and por = 0.3025 47
Figure 5.4 Cumulative erosion / sedimentation at the end of simulation for facua = 0.2854, por = 0.3025, gamma = 0.7716 and gamma2 = 0.2985 48
Figure 5.5 Linear regressions between XBeach input parameters and model performance metrics 49
Figure 5.6 Pearson correlation matrix between XBeach input parameters and model performance metrics 50
Figure 5.7 K-SD statistic based on GLUE methodology 52
Figure 5.8 Relationship between facua and other output metrics 54
Figure 5.9 Observation of change in bed level for facua value of 0.1575 55
Figure 5.10 Observation of change in bed level for facua value of 0.1872 55
Figure 5.11 Bed level change for each value of facua 56
Figure 5.12 Change in bed level in 2D for facua value of 0.1575 56
Figure 5.13 GLM velocity at cell center at time step 402 for facua value of 0.1575 57
Figure 5.14 Relationship between BSS and variation of input Parameters 58
Figure 5.15 Observation of GLM velocity direction at nt = 408 and alond different alongshore grid for two values of gamma 59
Figure 5.16 Cross sectional profile for according to different values of gamma 60
Figure 5.17 Observation of facua vs BSS for morfac value of 20 at higher value of gamma (0.6) 61

Figure 5.18 Observation of facua vs CumVdt for morfac value of 20 at higher value of gamma (0.6) 62
Figure 5.19 Profile Analysis Plot for morfac value of 20 63
Figure 5.20 Change in longshore length of the model grid 64
Figure 5.21 Relationship between gamma and BSS for reduced grid size 65
Figure 5.22 Profile analysis plot when longshore length was reduced 65
Figure 5.23 Observation of BSS and cumulative erosion volume with variation of dtheta 67
Figure 5.24 Variation of erosion and accretion with dtheta 68
Figure 5.25 Simulated bed levels for each value of dtheta 69
Figure 5.26 Observation in change in bed level (dtheta = 20 °) 69
Figure 5.27 Observation in change in bed level (dtheta = 14 °) 70
Figure 5.28 Observation in change in bed level (dtheta = 2 °) 70
Figure 5.29 Observation in change in bed level for dtheta value of 2°,14° and 20° 71
Figure 5.30 Observation of flow velocities at observation point 1 for different values of dtheta 72
Figure 5.31 Illustration of angle of wave incidence - theta 73
Figure 5.32 Bathymetry used for the variation of theta 73
Figure 5.33 Hydrodynamic input used for the variation of theta 74
Figure 5.34 Magnitude of erosion and accretion volumes in accordance with angle of wave incidence (θ) 75
Figure 5.35 Erosion and accretion volumes left and right of shore normal 75
Figure 5.36 Change in bed level with respect to change in θ 76
Figure 5.37 Observation of cumulative sedimentation/erosion for theta = −40° 77
Figure 5.38 Observation of cumulative sedimentation/erosion for theta = 40° 77
Figure 5.39 GLM velocities at cell centre showing direction of sediment transport for theta value of −40° and 40° 78
Figure E.1 Relationship between BSS and variation of input Parameters 108

List of Tables

Table 2.1 Deep and shallow water waves 12
Table 2.2 Classification of storm surges according to BSH 17
Table 3.1 Different wave breaking formulations implemented 24
Table 3.2 Characteristics of selected sensitivity methods based on Arkel (2016) 28
Table 3.3 Definition, range and default value of selected parameters 30
Table 4.1 Model performance based on BSS 32
Table 4.2 Information contained in a wave.txt file 41
Table 4.3 Files needed for XBeach model setup 44
Table 4.4 Modeling - Input Data 44
Table 5.1 Selected Parameters for LHS-based Simulation 45
Table 5.2 Selected LHS-based Parameter Combinations used in XBeach Simulations . 45
Table 5.3 Selected LHS-based Parameter Combinations for Sensitivity Analysis (BSS > 0) 51
Table 5.4 Modeling - Input Data for OAT method 53
Table C.1 Generated values of LHS-based Parameter Combinations Used in the study 103
Table E.1 Overview of simulation runs when facua, gamma and gamma2 were varied 107
Table F.1 Overview of simulation runs for morfac value of 20 109
Table G.1 Overview of simulation scenario for variation of dtheta 110
Table H.1 Overview of simulation scenario for variation of wave incidence angle theta 110

List of Symbols

Symbol	Unit	Description
a	m	amplitude of a linear wave
A	-	wave action density
A_s	-	wave asymmetry parameter
A_{sb}	-	bed-load coefficient used in Van Thiel-Van Rijn equations
A_{ss}	-	suspended load coefficient used in Van Thiel-Van Rijn equations
c	m/s	phase velocity
c_g	m/s	group velocity
c_θ	m/s	wave propagation speed in θ - space
c_x	m/s	wave propagation speed in x-direction
c_y	m/s	wave propagation speed in y-direction
D_*	-	non-dimensional grain size used in Van Thiel-Van Rijn equations
D_{50}	m	median grain size at which 50% of the sediment sample is finer and 50% is coarser
D_{90}	m	coarse grain size at which 90% of the sediment sample is finer and 10% is coarser
D_f	W/m²	wave dissipation due to bottom friction
D_v	W/m²	wave dissipation due to vegetation
E_w	J /m²	short-wave energy
F_x	N/m²	wave-induced stress in x-direction
F_y	N/m²	wave-induced stress in y-direction
f	s^{-1}	Coriolis coefficient
f_{T_s}	-	adaptation time factor
f_{Sk}	-	Wave skewness calibration factor
f_{As}	-	Wave asymmetry calibration factor
hPa	Pascal (Pa)	Atmospheric pressure, 1 hPa = 100 pascals (Pa)
H	m	wave height of a linear wave
H_{max}	m	maximum wave height
H_{rms}	m	root mean square wave height

Symbol	Unit	Description
H_{sig}	m	arithmetic mean of the highest one-third of the wave height distribution
H_{m0}	m	significant wave height based on spectral method
h	m	water depth
k	-	wave number
k_x	m^{-1}	x-component of wave number
k_y	m^{-1}	y-component of wave number
L	m	wave length
L_m	m	Mean wave length
m_{cr}	-	critical wet or dry slope
n	-	ratio of group velocity to phase velocity
ν_t	m^2/s	horizontal viscosity
Q_b	-	fraction of wave breaking
S_k	-	wave skewness parameter
S_w	Jm^{-2}	wave energy density in each directional bin
T	s	Wave period of a wave
T_{rep}	s	representative time period
T_s	s	adaptation time used in advection-diffusion equation
$T_{\mathrm{s,min}}$	s	minimum adaptation time
U_{crc}	m/s	critical velocity for currents
U_{crw}	m/s	critical velocity for waves
u^E	m/s	Eulerian velocity in x-direction
u^L	m/s	depth-averaged Lagrangian velocity in x-direction
u^S	m/s	Stokes drift in x-direction
u_{rms}	m/s	Root-mean square velocity
v^E	m/s	Eulerian velocity in y-direction
v^L	m/s	depth-averaged Lagrangian velocity in y-direction
v^S	m/s	Stokes drift in y-direction
w_s	m/s	sediment fall velocity
z_m	m	observed post-storm depth
z_p	m	simulated post-storm depth
z_r	m	pre-storm reference depth
δ	rad	initial phase angle

Symbol	Unit	Description
δH_{rms}	m	fraction of wave height
η	m	Surface elevation of a linear wave
γ	-	breaker index
γ_2	-	secondary breaker index threshold
ρ	kg/m³	water density
σ	Hz	intrinsic wave frequency
τ_{bx}	N/m²	bed shear stress in x-direction
τ_{by}	N/m²	bed shear stress in y-direction
τ_{sx}	N/m²	surface shear stress in x-direction
τ_{sy}	N/m²	surface shear stress in y-direction
τ^E_{sx}	N/m²	Eulerian surface shear stress in x-direction
τ^E_{sy}	N/m²	Eulerian surface shear stress in y-direction
θ	rad	wave angle relative to x-axis
ω	Hz	angular frequency
ξ	-	Iribarren parameter

List of Abbreviations

ALS	Airbone Laser Scanning
BEAR	Baltic Earth Assessment Report
BSH	Bundesamt für Seeschifffahrt und Hydrografie
BSS	Brier Skill Score
CDF	Cumulative Distribution Function
CFL	Courant–Friedrichs–Lewy
DEM	Digitial Elevation Model
DHHN2016	Deutsches Haupthöhennetz 2016
EOMAP	Earth Observation Mapping
EPSG	European Petroleum Survey Group)
ESL	extreme sea level
ETRS89	European Terrestrial Reference System 1989
GLM	Generalized Lagrangian Mean
GLUE	Generalized Likelihood Uncertainty Estimation
GMSL	Global mean sea level
GNSS	Global Navigation Satellite System
GSA	General Sensitivity Analysis
HISWA	Hindcasting Shallow Water Waves
IG	Infragravity
JONSWAP	Joint North Sea Wave Project
K-SD	Kolmogorov–Smirnov D-statistic
LHS	Latin Hypercube Sampling
LiDAR	Light Detection and Ranging
MATLAB	MATrix LABoratory
MV	Mecklenburg-Vorpommern
NHN	Normalhöhennull
NetCDF	Network Common Data Form
OET	Open Earth Tools
PDF	Probability Density Function
RMSE	Root Mean Square Error
RTK	Real-Time Kinematic
ResCAD	Research Project on Coastal Dune Dynamics
SH	Schleswig-Holstein
SLR	Sea-level rise
UAV	Unmanned Aerial Vehicle
UTM	Universal Transverse Mercator

This page is intentionally left blank

1 Introduction

Coastal zones worldwide are increasingly exposed to the impacts of global climate change. Rising sea levels, more frequent extreme events and intensifying storm surges pose severe risks to ecosystems, settlements and infrastructure. These challenges are particularly relevant for the southern Baltic Sea, where coastal morphology and limited tidal influence amplify vulnerability (Aakjær & Buch, 2022; Wolski et al., 2014).

1.1 Sea Level Rise and Coastal Flooding

The rise of the Global mean sea level (**GMSL**) is a well-recognized indicator of global climate change, primarily driven by the melting of land-based ice and the thermal expansion of seawater (Hibbard et al., 2007). Increasing sea levels directly accelerate coastal erosion, elevate flood risks and threaten communities and infrastructure worldwide (Cazenave & Cozannet, 2014). Projections suggest that Sea-level rise (**SLR**) will also increase the frequency and intensity of extreme sea levels, thereby heightening the probability of destructive flooding events with serious socioeconomic consequences (Hinkel et al., 2021; Kirezci et al., 2020).

Within Europe, the Baltic Sea and the North Sea are among the regions expected to experience the strongest increases in extreme sea levels (**ESLs**) towards the end of the century (Vousdoukas et al., 2017). For Germany and other littoral states of the Baltic Earth Assessment Report (**BEAR**), this implies a substantial increase in coastal flood damage (Rutgersson et al., 2021). Moreover, current dike design heights along the German Baltic Sea may become insufficient under high-SLR scenarios, particularly in the case of extreme storm surges (Kiesel et al., 2023).

Observational data confirm that sea levels are already rising along the German Baltic coast. Between 1900 and 2015, the southwestern Baltic recorded an increase of 1.0 –1.7 mm/year, while the global mean between 2006 and 2015 reached approximately 3.6 mm/year (Jensen et al., 2019). At the Rostock-Warnemünde gauge, mean sea level has risen by about 15 cm since 1953 (Figure 1.1), illustrating the persistent upward trend (Saathoff et al., 2020).

In addition to gradual SLR, storm surges remain the dominant hazard for coastal flooding worldwide (Bernier et al., 2024). This is especially critical in the Baltic Sea, where tidal amplitudes are minimal but storm surges can reach considerable heights in the southwestern basin (Aakjær & Buch, 2022; Wolski et al., 2014). Together, SLR and intensified storm surges present the greatest challenges for coastal defense in the German Baltic region (Meinke & Reckermann, 2012).

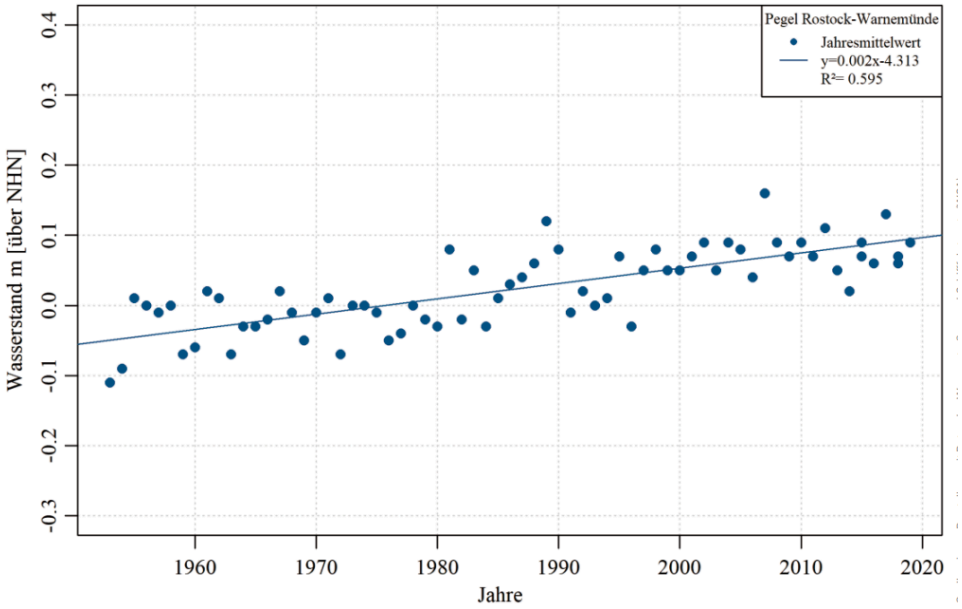

Figure 1.1: Annual averages of the water level at the WSA gauge in Rostock-Warnemünde (Saathoff et al., 2020)

1.2 Baltic Region and the German Baltic Coast

The Baltic Sea is a semi-enclosed, non-tidal intra-continental shelf sea with a narrow connection to the North Sea through Kattegat and Skagerrak (Figure 1.2). As part of the eastern North Atlantic, it is subject to both anthropogenic pressures and natural hazards (Reusch et al., 2018; Rutgersson et al., 2021).

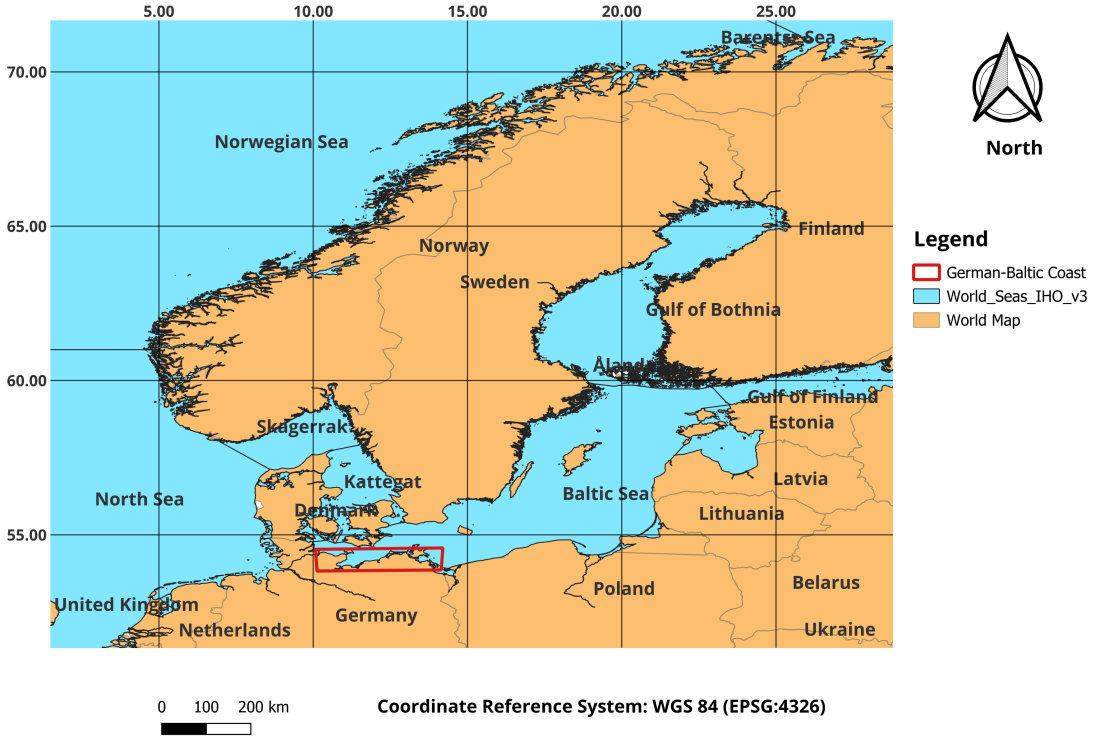

Figure 1.2: Location of German Baltic coast in the world map

The German Baltic Sea coast extends over 2582 km across two federal states: Mecklenburg-Vorpommern (**MV**) and Schleswig-Holstein (**SH**) (Figure 1.3). A significant portion of this shoreline is protected by state-maintained coastal protection dunes (StALU, 2009). These soft-engineered structures combine ecological and protective functions by preserving quasi-natural beaches while acting as primary barriers against storm surges (Kaehler et al., 2022). A typical aerial view of such structure is shown in Figure 1.4.

Figure 1.3: Coastline lengths of the state of Mecklenburg-Vorpommern. After (StALU, 2009).

The southern Baltic shoreline consists of two characteristic landforms: dune coasts, formed from Holocene marine and aeolian sands, and cliff coasts, composed of unconsolidated Pleistocene deposits, primarily glacial tills and sands (Dudzińska-Nowak, 2022). Both types are highly susceptible to erosion, particularly during extreme hydrodynamic events. Indeed, the onset of the Littorina Transgression around 8400 years ago initiated continuous cliff retreat along the German Baltic coast (Fleming et al., 1998). Today, the most

severe erosion events occur under storm surge conditions, where high winds, elevated waves, and surge-driven water level rises act in combination (Furmańczyk & Dudzińska-Nowak, 2009).

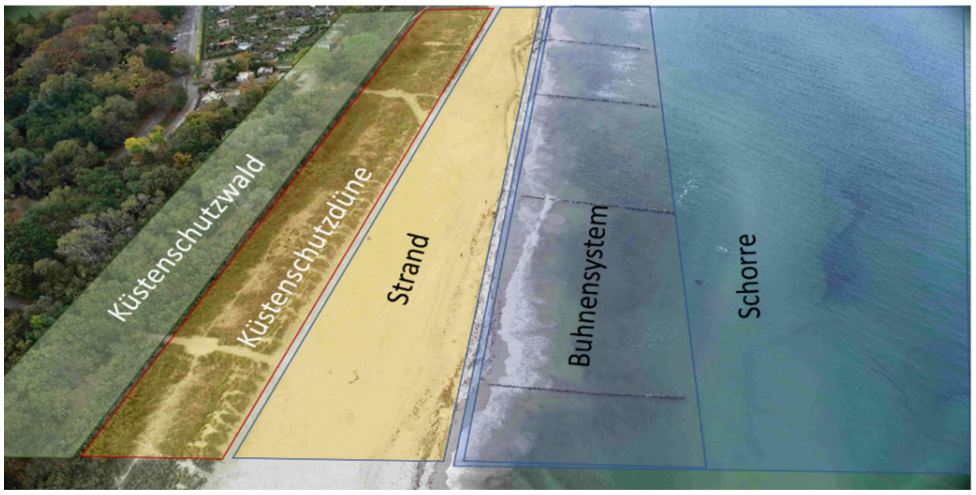

Figure 1.4: Characteristic structure of a beach section protected by dunes and groynes. After (Fleischer, n.d.)

1.3 Coastal Protection Approaches in Mecklenburg-Vorpommern

Coastal protection in MV relies on a combination of hard and soft engineering strategies, with particular emphasis on state-maintained dunes and dikes. Along the 237 km-long outer flat coast, 29 coastal protection dune systems extend across roughly 106 km, providing the first line of defense against storm surges (StALU, 2009). These dunes are differentiated into system protection dunes, which complement other structures, and full protection dunes, designed to withstand severe storm conditions independently. The cross-section of a full protection dune (Figure 1.5, bottom) typically includes a wear zone, a reserve zone, and a safety buffer, ensuring functionality even after partial erosion. In parallel, state coastal protection dikes, totaling more than 218 km in length, safeguard low-lying hinterland areas (Figure 1.5, top). Constructed from compacted earth, they are engineered to prevent overtopping and inland flooding.

Sea dikes, constituting around 21% of the total dike length, form the ultimate barrier against storm surge intrusion into the Bodden and Haff systems. Their design considers local hydrodynamics, including water levels, wave run-up, and foreland conditions. In areas with limited space, combined systems, integrating dunes, dikes, and forested forelands, are deployed to enhance resilience.

In addition to structural defenses, long-term changes in sea level must also be considered. Along the southwestern German coast, including MV, the RSLR typically ranges between +1 and +3 mm/yr (Wolski et al., 2014). This makes the region particularly sensitive to

storm surge intensification and sustained coastal change, highlighting the importance of regionalized modeling for effective protection planning. Climate change is expected to further intensify both cliff and beach erosion, while simultaneously altering sediment supply within the coastal system (Hoffmann & Lampe, 2007). These dynamics will likely increase the financial costs of coastal defense, reduce the sediment available for shoreline maintenance, and threaten both valuable natural habitats and economic assets (Schmidt et al., 2014; Team, 2008).

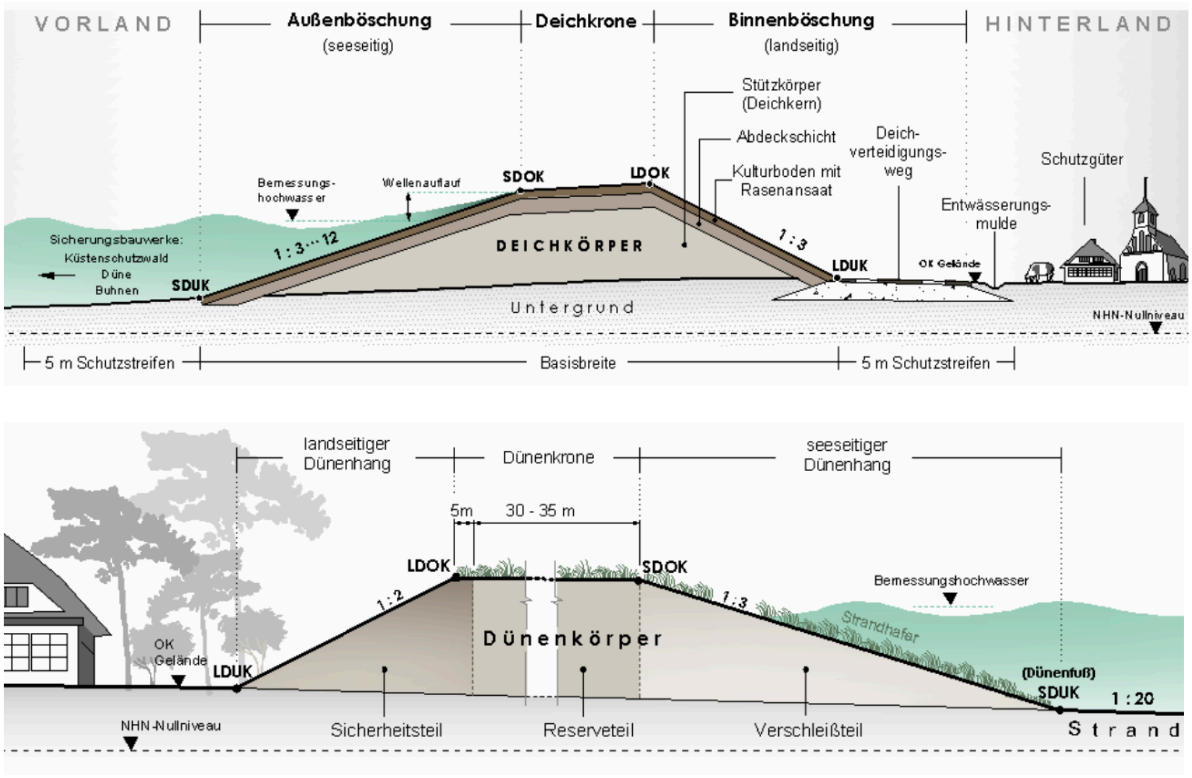

Figure 1.5: Methods of Coastal Protection. Standard cross-section of a dike (top) and standard cross-section of a full protection dune (bottom). After StALU (2009)

Beyond dunes and dikes, MV employs supplementary measures tailored to local geomorphology and hazard exposure. Groynes, often timber-based, are installed perpendicular to the shoreline to reduce longshore sediment transport and encourage beach accretion. Offshore breakwaters dissipate wave energy before it reaches sensitive zones, especially near cliffs or settlements. Longitudinal structures, including stone revetments, seawalls, and gravel embankments, reinforce shorelines against erosion and overtopping. At estuaries and river mouths, closure structures protect inland waters from surge intrusion.

Nature-based approaches complement these engineered defenses. Vegetation measures, such as beachgrass planting, stabilize dunes, while coastal protection forests provide additional wave damping. In urban areas, integrated solutions like flood walls, elevated terrain and mobile barriers ensure protection of densely populated zones. Collectively, this

portfolio of measures represents a multifunctional and adaptive coastal defense strategy that balances safety and ecological integrity.

1.4 Motivation and Objectives

The Baltic Sea, as a peripheral basin of the North Sea, presents significant challenges for coastal protection due to its complex bathymetry and highly variable wind exposure. Storm surges already endanger coastal settlements, ecosystems, and infrastructure, particularly along the sandy low-lying shores of Mecklenburg–Western Pomerania. Here, dunes constitute around 70% of the coastline and serve as essential protective structures against flooding and erosion. While traditionally considered wearing structures, they have increasingly been integrated into state-level coastal protection concepts as nature-based defense elements.

In Mecklenburg–Western Pomerania, the design and management of these dunes has historically been guided by the calculation approach developed by Newe (2013) in the NewDune model. This model provided a practical method for assessing dune erosion under storm surge conditions and significantly advanced the understanding of dune performance as part of regional protection strategies. However, NewDune operates mainly in one dimension, focusing on cross-shore dune profiles. It approximates longshore processes and cannot fully resolve hydrodynamic complexity under extreme events, which limits its applicability for broader design and calibration purposes.

To address these limitations, the **ResCAD** project investigates hydromorphodynamic processes at coastal protection dunes with the goal of predicting future sand requirements and developing optimized cross-sections. Numerical models such as XBeach extend the modelling framework established by NewDune by explicitly simulating storm-induced hydrodynamics and morphodynamics. Yet, XBeach introduces a large number of simulation parameters, the influence of which on model outcomes is still not fully understood. This uncertainty complicates calibration and hampers the reliable application of the model in coastal protection planning.

The primary objective of this master's thesis is therefore to investigate the influence of simulation parameters on dune erosion processes on the Baltic coast (at the Ahrenshoop site) using the numerical model XBeach (netCDF-MPI version). Through a systematic parameter study, the thesis aims to:

1. Identify and analyze key simulation parameters that govern morphodynamic responses under extreme hydraulic events (e.g., storm surges and wave attack).
2. Evaluate the sensitivity of dune erosion and erosion volumes to variations in wave conditions, boundary conditions, and model inputs.

3. Quantify the effect of individual parameters on modeled outcomes and explore the possibility of aggregating them into global parameters to simplify model calibration.
4. Formulate recommendations for parameter ranges that support the design and improvement of dune erosion management strategies in comparable coastal settings.

1.5 Structure of the Thesis

The thesis is organised into six key chapters, each adressing different aspects of the research to provide a comprehensive understanding of the study.

Chapter 1: Introduction presents the motivation, scope and objectives of the thesis. It outlines the problem context and provides an overview of the research structure.

Chapter 2: Theoritical Background and Data explains the fundamental concepts and governing theories relevant to the study. It also explains how data were obtained for this study.

Chapter 3: Literature Review summarizes how sensitivity analysis can be performed for this study. It also briefly introduces the selected parameters for this study.

Chapter 4: Methodology details the modeling framework, tool and procedures employed. It also discusses simulation setup and workflow design.

Chapter 5: Results and Discussion presents the simulation results and compares them with observed data. It provides interpretation, critical evaluation and discussion of findings.

Chapter 6: Conclusion and Outlook summarizes the key outcomes of the research and draws final conclusions in relation to the objectives. It also suggests potential improvements, future research directions and broader implications of the study for the parameter studies in coastal-dune erosion modeling on the Baltic coast.

2 Theoretical Background and Data

In this chapter, the fundamental and important theoretical background related to this study is briefly presented. The related information is mostly extracted from Holthuijsen et al. (1989) and Bosboom & Stive (2023). The information about the data used in this study is also briefly presented.

2.1 Description of Coastal Region

The coastal zone can be subdivided into distinct areas, each with specific characteristics. Various definitions of the coastal region exist in the literature. In this work, the classification by Bosboom & Stive (2023) is adopted. According to their definition, the coastal profile or shoreface refers to the active nearshore zone influenced by wave dynamics (Figure 2.1). This zone extends from water depths of approximately 10–20 meters up to the beach and adjacent dune system. The shoreface itself can be further divided into two parts: the lower shoreface, also known as the shoaling zone, where wave heights increase until breaking occurs and the upper shoreface, which comprises the surf zone, swash zone, beach and the initial dune row or cliff face. On engineering time scales, morphological changes are concentrated primarily within the upper shoreface.

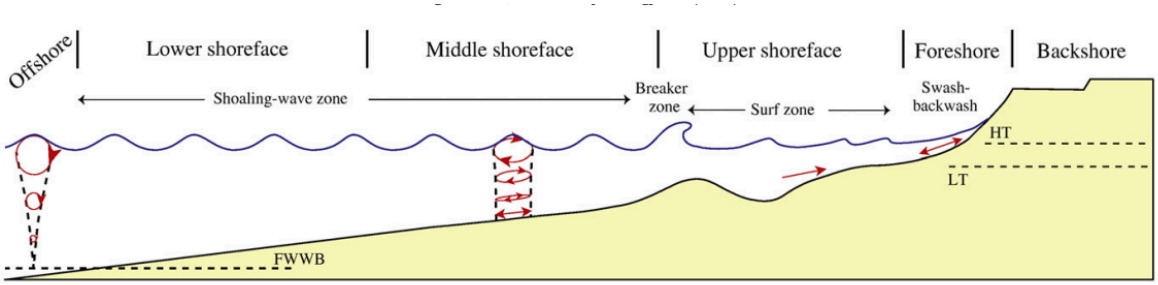

Figure 2.1: Schematization of the coastal region, including the positions of the various shoreface zones. After Dashtgard et al. (2012)

The intertidal zone, which forms part of the upper shoreface, represents the transitional area between land and sea. It is exposed during low tide and submerged during high tide, making it subject to both hydrodynamic forces and wind-driven (aeolian) processes. Similarly, the swash zone functions as a transitional area, alternating between exposure and inundation at the shorter timescales of wind and swell waves. This zone, located between the maximum uprush and backwash of waves, is commonly referred to as the beach face (Puleo et al., 2000).

Figure 2.2 shows a schematic plan view of a coastal area with most of the natural forcing conditions, natural features and some examples of man-made interventions (groynes, revetments, breakwaters, barrier islands, etc.) in a natural coastal system.

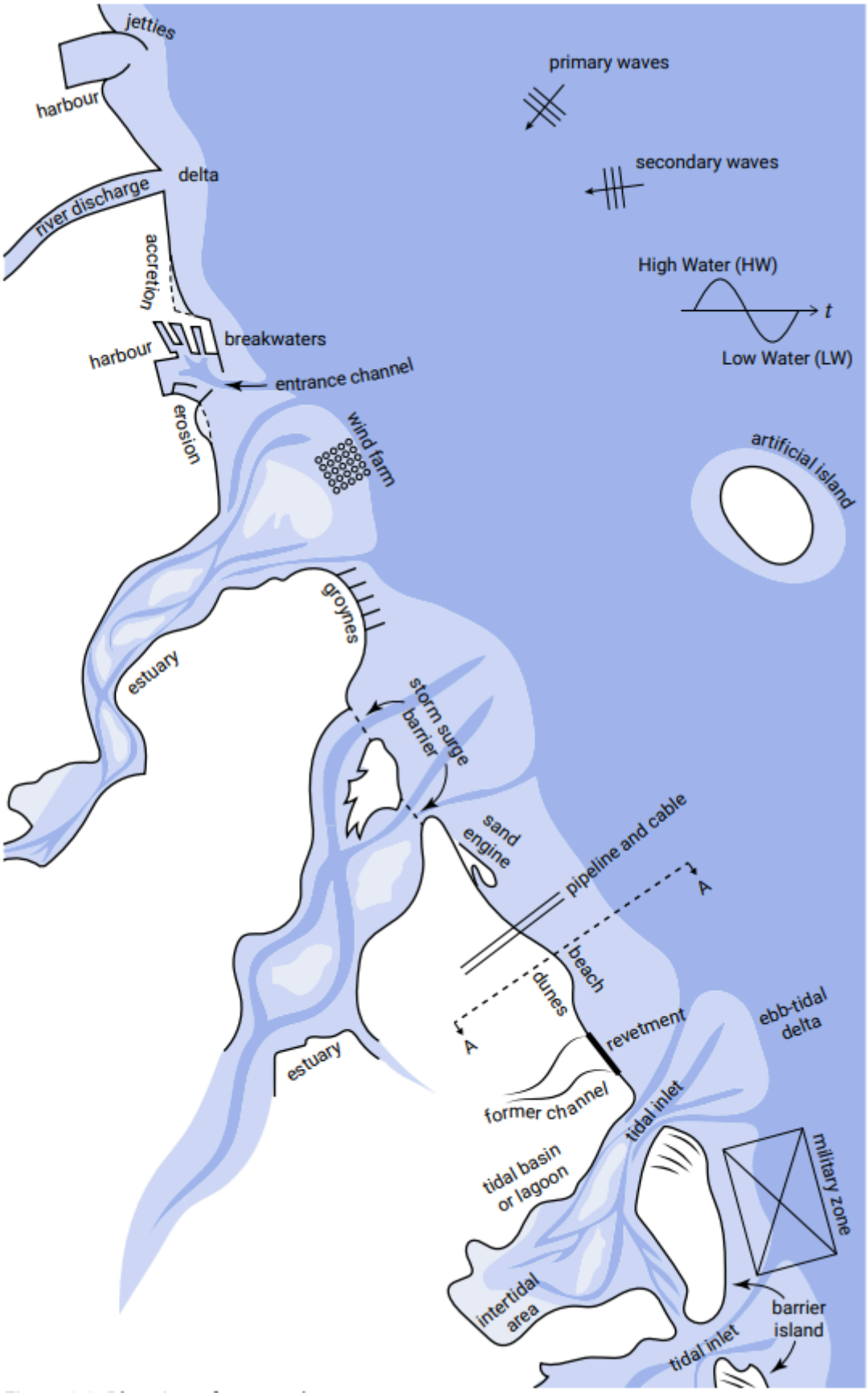

Figure 2.2: Plan view of the coastal area and the involved coastal processes (Bosboom & Stive, 2023)

2.2 Definition of a Wave

In a time record, the surface elevation is the instantaneous elevation of the sea surface (i.e., at any one moment in time) relative to some reference level. In such a record, a wave is the profile of the surface elevation between two successive downward or upward zero-crossings of the elevation (zero = mean of surface elevations) as shown in Figure 2.3. Figure 2.4 shows a simple representation of a wave with the visualization of the terms involved, which is sinusoidal in nature.

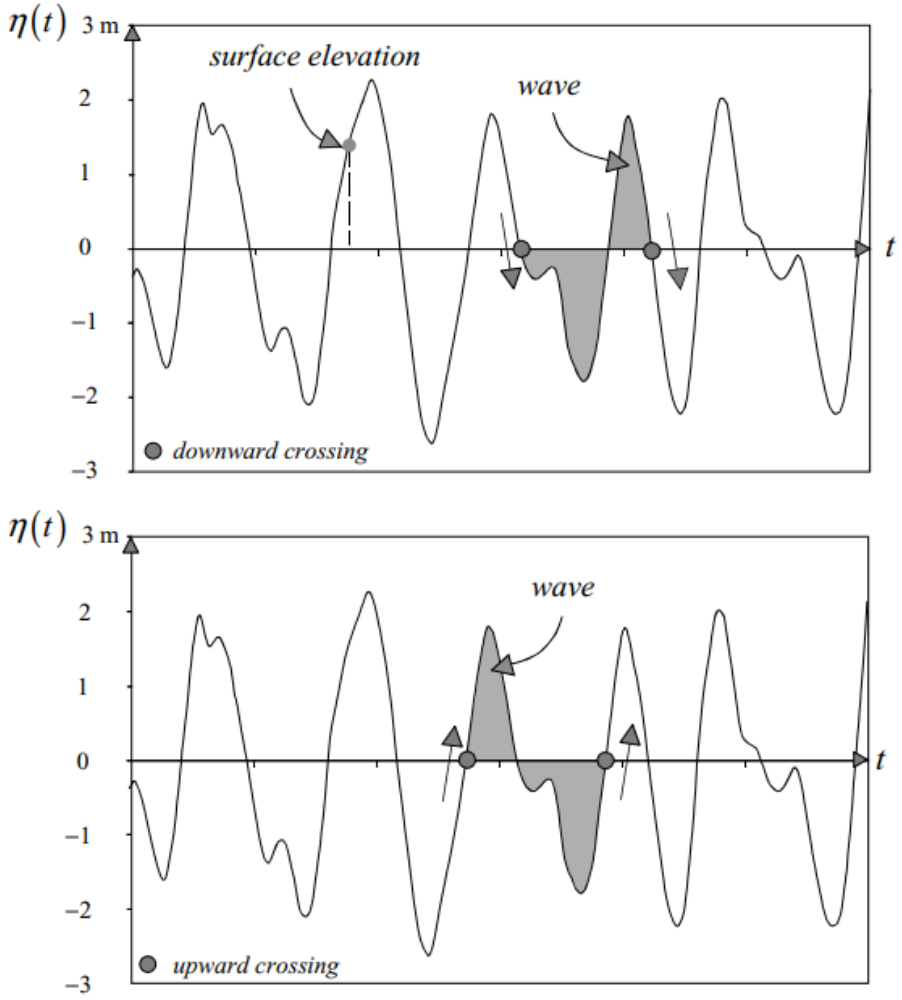

Figure 2.3: The definition of a wave in a time record of the surface elevation with downward zero-crossings (upper panel) or upward zero-crossings (lower panel). After (Holthuijsen et al., 1989)

The surface elevation of a linear wave is:

$$\eta(x,t) = \frac{H}{2}\cos(\omega t - kx + \delta) = a\cos(wt - kx + \delta) \tag{2.1}$$

where H is wave height, $a = \frac{H}{2}$ is amplitude, $\omega = \frac{2\pi}{T}$ is angular frequency, T is wave period, $k = \frac{2\pi}{L}$ is wave number, L is wavelength and δ is intial phase angle. The relationship between wave period and wave length (dispersion relationship) is:

$$L = \frac{gT^2}{2\pi} \tanh\left(\frac{2\pi h}{L}\right) \tag{2.2}$$

where h is the water depth.

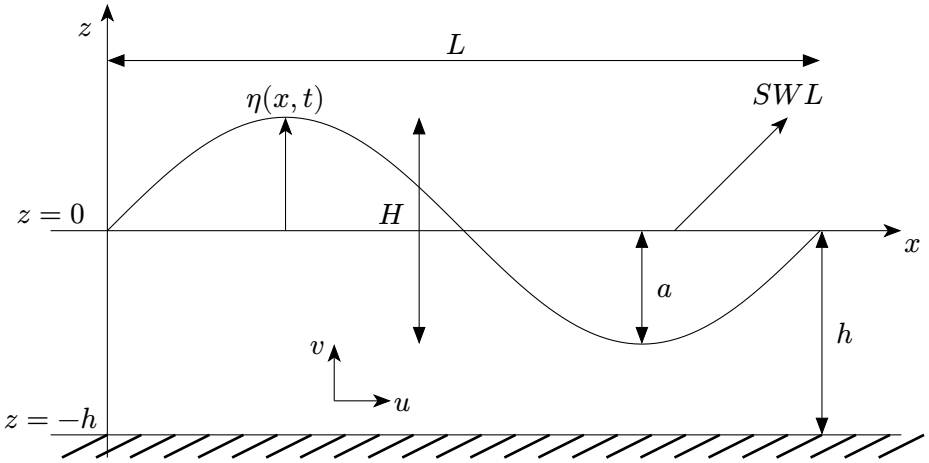

Figure 2.4: Simple representation of a wave

Wave Parameters

Wavelength (L)

Wavelength (L) is the horizontal distance between two points of identical phase in two successive waves, e.g., between two consecutive wave troughs (Figure 2.3). The mean wavelength (L_m) is the arithmetic mean of all recorded wavelengths.

Wave Height (H)

Wave height (H) is the vertical distance between the lowest point of a wave trough and the highest point of the following wave crest (Figure 2.3). The intensity of the measured sea state is usually expressed using the significant wave height (H_{sig}). This is the arithmetic mean of the highest one-third of the wave height distribution and can also be derived as H_{m0} from the wave spectra.

Since the wave energy is proportional to the square of the wave height, most of the time, a quadratically weighted averaged value H_{rms} (root-mean-square) is used. H_{rms} is related to significant wave height (H_{m0}) as shown in Equation (2.3) as per Holthuijsen et al. (1989).

$$H_{\text{rms}} = \frac{1}{2}\sqrt{2}H_{\text{m0}} \tag{2.3}$$

Wave Period (T):

The wave period (T) is the time interval between the start and the end of the wave (the interval between one zero-down crossing and the next (Figure 2.3).

2.3 Wave Classification

Various types of waves can be observed at the sea that generally can be divided into different groups depending on the wavelength, wave-generating force and restoring force as shown in Figure 2.6.

Fundamental Wave Types and Depth Influence

Shallow and deep water waves are classified based on the relationship between the water depth and the wavelength of the wave. Deep water waves occur when the water depth is greater than half the wavelength, so the wave does not feel the ocean bottom and its speed depends only on the wavelength. Shallow water waves occur when the water depth is less than one-twentieth of the wavelength, so the wave is strongly affected by the ocean floor, and its speed depends only on the water depth. This information is also shown in Table 2.1.

Water waves can fundamentally be classified into translatory and oscillatory waves. Oscillatory waves primarily transport energy, whereas translatory waves also carry a significant amount of mass. The type of wave present depends primarily on its origin. For example, tsunamis or surge waves caused by slope failures are classified as translatory waves.

Table 2.1: Deep and shallow water waves

wave type	**condition**
Deep water waves	$h > \frac{L}{2}$
shallow water waves	$h \leq \frac{L}{20}$
Transitional water waves	$\frac{L}{20} < h \leq \frac{L}{2}$

If the water depth is greater than approximately half the wavelength ($h \geq \frac{L}{2}$), the water particles under wind waves move in closed, nearly circular paths (orbital paths) down to that depth. In this case, there is no interaction between the wave and the seabed. These waves are therefore referred to as deep water waves. Particle paths for all the three different type of water depths is also illustrated in Figure 2.5.

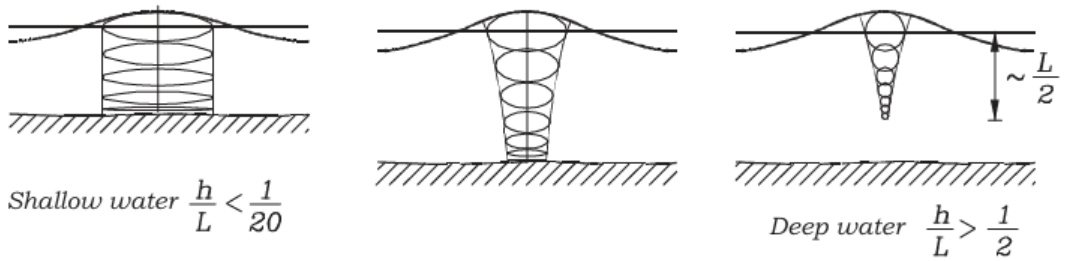

Figure 2.5: Particle paths illustrated for three different water depths. After Andersen & Frigaard (2011)

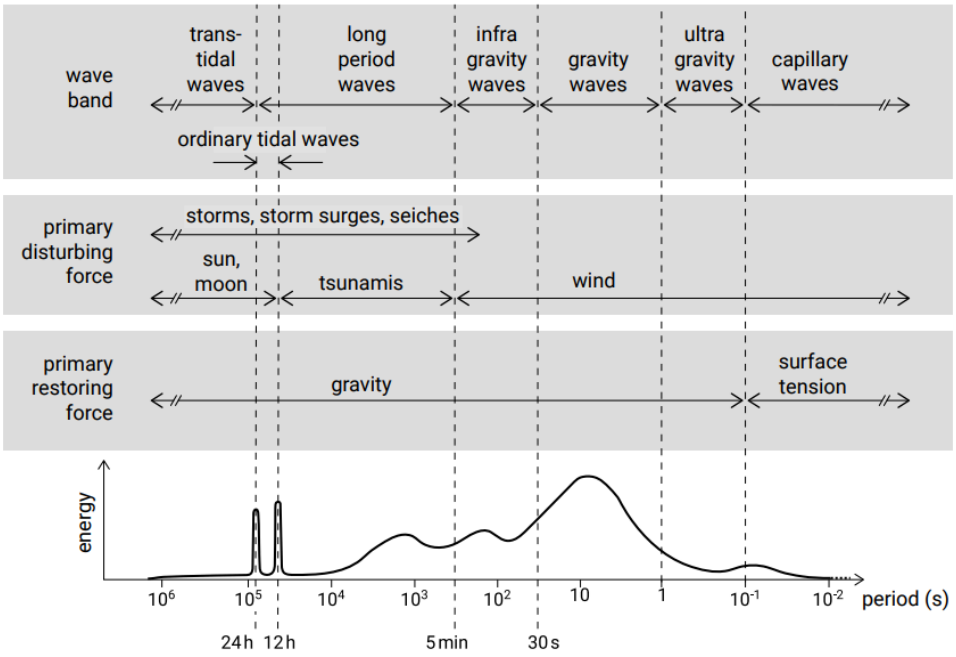

Figure 2.6: Classification of waves based on wavelength(top line), wave-generating force (middle line) and restoring force (bottom line). After Munk (1951) and Kinsman (1984).

2.4 Wave Transformation

When waves propagate from deep into intermediate and shallow water depths, the waves transform, i.e. wave height, length and direction change until the waves finally break and lose their energy. A schematic diagram is shown in Figure 2.7. Wave transformation takes place because the waves are affected by the seabed through processes such as *refraction, shoaling, bottom friction and wave-breaking.*

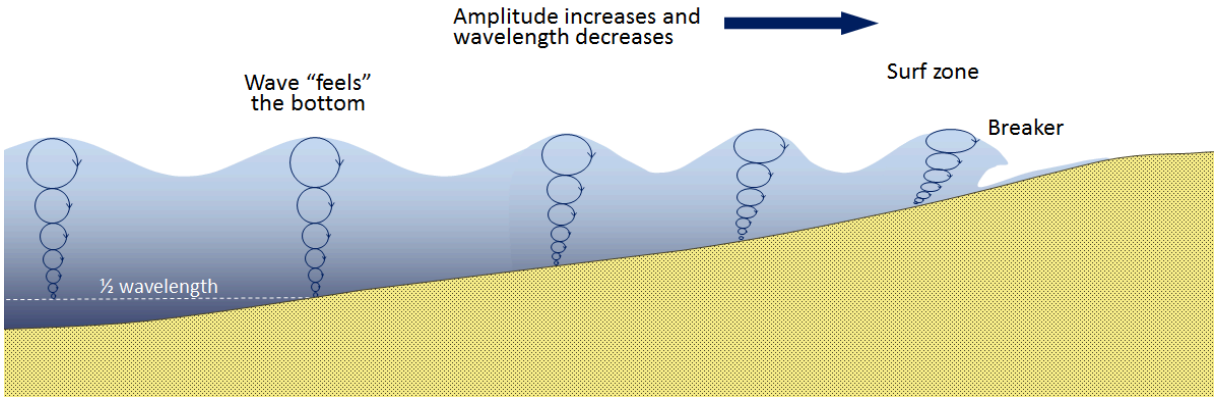

Figure 2.7: Propagation of waves towards the surf zone. After Earle (2015)

As waves move from deep to shallower water ($h \leq \frac{L}{2}$) their frequency stays constant while the phase speed c and wavelength L decrease, so the waves slow and steepen. Because group speed falls, energy flux conservation concentrates energy and the wave height grows and this phenomenon is *shoaling*. If depth varies along a crest, speed gradients cause crests to bend toward regions of lower speed, turning obliquely incident waves shore-

normal. This phenomenon is *refraction*. Around obstacles such as headlands, islands, or breakwaters, waves spread laterally into the sheltered region by *diffraction*, redistributing energy behind the obstruction. In very shallow water, strong near-bed orbital motions interact with bed roughness, and bottom friction gradually dissipates wave energy. Ultimately, increasing steepness and depth limitation make the wave unstable; the crest outruns the trough and the wave breaks, rapidly dissipating energy in the surf zone and driving currents and setup.

The mode of wave breaking depends on both wave characteristics and the slope of the seabed. Battjes (1974) demonstrated that this can be expressed by the **Iribarren parameter** (ξ) defined as:

$$\xi = \frac{\tan \alpha}{\sqrt{\frac{H_0}{L_0}}} \tag{2.4}$$

where $\tan \alpha$ is the steepness of beach and the ratio $\frac{H_0}{L_0}$ is wave steepness for deep water.

Depending on ξ, different breaker types are observed (Figure 2.8), with gradual transitions between them:

1. **Spilling breakers** occur on gentle slopes, breaking gradually over several wavelengths. A foam line develops at the crest, dissipating nearly all wave energy with little reflection.
2. **Plunging breakers** occur on steeper slopes, characterized by the curling of the crest, strong turbulence, and partial reflection of wave energy.
3. **Surging breakers** occur on very steep reflective shores, where waves rush up and down the slope with minimal air entrainment. Energy reflection is high, and the breaker zone is very narrow.
4. **Collapsing breakers** represent an intermediate case between plunging and surging, where the wave collapses without a fully developed curling crest.

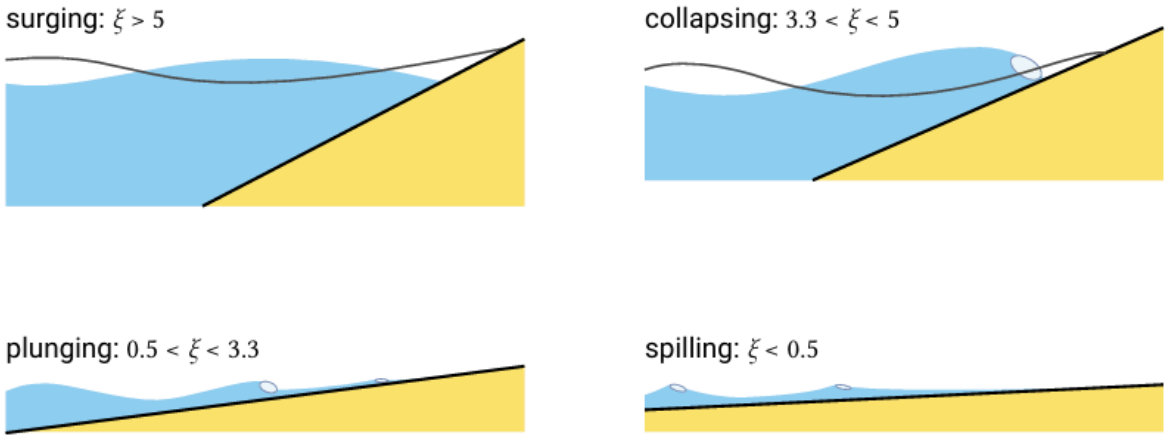

Figure 2.8: Breaker types according to Battjes (1974). After Bosboom & Stive (2023)

2.5 Coastal Morphodynamics in the German Baltic Sea

Coastal morphodynamics in the German Baltic Sea region are shaped by the dynamic interplay of natural forces and human interventions, producing a highly variable and evolving shoreline. The coast features sandy beaches, barrier islands, extensive lagoons (Bodden), and prominent active cliffs, such as those along the Fischland peninsula in Mecklenburg–Western Pomerania. Approximately two-thirds of the shoreline is currently classified as erosional, with average cliff retreat rates between 20–40 cm/year and localized beach erosion rates reaching up to 2.1 m/year in particularly exposed locations (Tiede et al., 2024). In contrast, some sheltered sections experience sediment accumulation of up to 4.0 m/year, reflecting the natural morphodynamic balance between erosional and accretional sectors (Schönthaler et al., 2017). Figure 14 provides a sketch of the main topographic coastal features and processes contributing to erosion and sedimentation at the Baltic Sea shores.

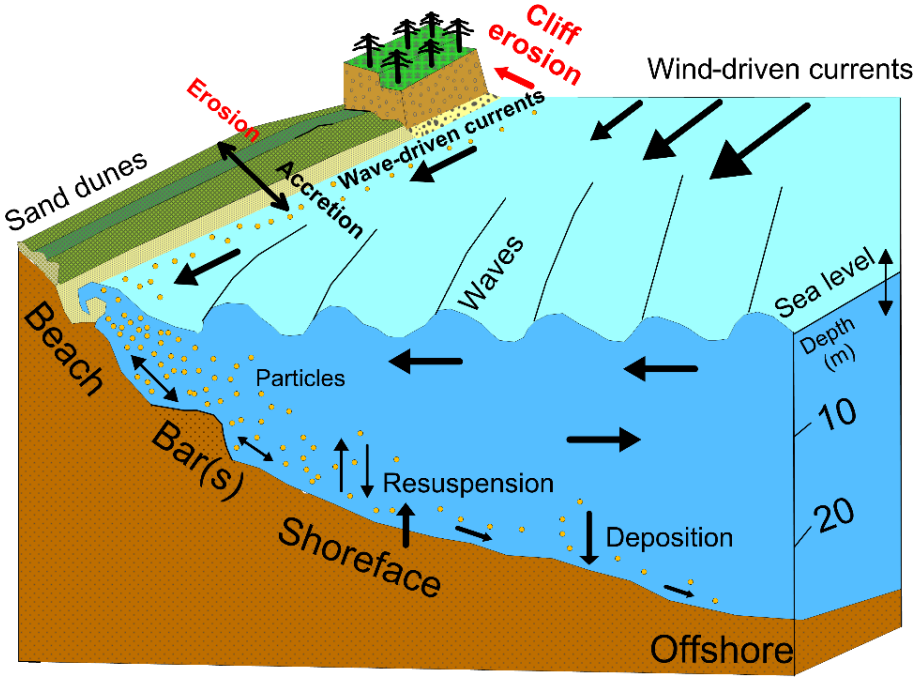

Figure 2.9: Main coastal topographic features and the morphodynamic processes of erosion and accretion at the Baltic Sea shore. After Weisse et al. (2021)

The equilibrium between erosion and accretion is governed by the combined influence of sediment availability, hydrodynamic regime, and antecedent topography, which control coastal responses over decadal to centennial scales Weisse et al. (2021). Among the most critical drivers are extreme sea levels and storm surges, which are discussed in detail in Section 2.6 and Section 2.7. Anthropogenic measures such as groynes, revetments, and beach nourishment further modify sediment pathways and may induce unintended

morphodynamic consequences, including enhanced downstream erosion or sediment trapping.

Human interventions, such as groynes, dikes, and beach nourishment, are implemented to mitigate erosion and flooding but frequently alter the natural morphodynamic equilibrium. These measures can accelerate erosion on adjacent unprotected stretches and disrupt sediment supply, particularly where cliffs, which are important natural sediment sources, are stabilized for agriculture or tourism (Schönthaler et al., Tiede et al.).

2.6 Hydrodynamic Forcing in the Baltic Sea

The Baltic Sea is almost non-tidal, as astronomical tides do not exceed several centimeters due to its semi-enclosed nature and limited water exchange with the North Sea via the Danish Straits (Sutherland et al., 2004). Consequently, wave action and meteorologically driven water level fluctuations dominate as the principal hydrodynamic forcing mechanisms for coastal change (Zeidler et al., 1995).

These fluctuations are mainly controlled by wind and atmospheric pressure anomalies. Persistent wind events lasting more than 10–20 hours can cause considerable regional water level increases (set-up) on downwind coasts, while other areas may simultaneously experience lowering of water levels (Wolski & Wiśniewski, 2021). In addition, low-pressure systems elevate sea levels through the inverse barometer effect, and in combination with wind forcing they may amplify extremes. Furthermore, the sea level of the North Sea influences the mean filling level of the Baltic, preconditioning the basin for subsequent storm surge development.

These mechanisms collectively establish the hydrodynamic boundary conditions that govern coastal morphodynamics and underpin storm surge events, which are described in more detail in the following Section 2.7.

2.7 Storm Surges in the Baltic Sea

Storm surges are the primary cause of coastal flooding along the world's low-lying coasts (Bernier et al., 2024). In the Baltic Sea, where tidal amplitudes are negligible, storm surges generate the most severe water level extremes, particularly in the southwestern regions (Wolski et al., 2014).

Two principal mechanisms drive Baltic storm surges: wind set-up and atmospheric pressure anomalies. Wind-induced surges are most frequent, resulting from persistent high-velocity winds with stable direction acting over the sea surface. These winds generate drift currents that pile up water along downwind coasts, elevating local sea levels. The magnitude of set-up depends on wind speed, duration, fetch length, coastal geometry,

bathymetry, and inter-basin water exchange Wolski & Wiśniewski (2021). Pressure-induced surges, in contrast, stem from the inverse barometer effect, where a 1 hPa pressure drop corresponds to a 1 cm static rise. Under dynamic conditions, moving pressure systems may amplify this two- to fourfold, especially when their translation speed resonates with natural sea surface oscillations. Most extreme events involve a combination of both mechanisms.

Recent case studies illustrate the complexity of storm surge dynamics. Groll et al. (2024) highlight that the 2017, 2019, and 2023 surges differed markedly in forcing: the 2017 event was amplified by prefilling despite moderate winds, the 2019 surge was primarily wind-driven, and the 2023 surge combined strong easterly winds with moderate prefilling to produce the highest levels observed in Flensburg in 66 years. Such events underscore that compound drivers, including wind, prefilling, atmospheric pressure and wave set-up, must be considered jointly in understanding and predicting storm surge hazards in the Baltic Sea.

At the German Baltic coast, four level of storm surges are distinguished as shown in Table 2.2 according to Bundesamt für Seeschifffahrt und Hydrografie (**BSH**).

Table 2.2: Classification of storm surges according to BSH

Storm Surge	**Deviation from MSL**
Storm surge	1.0 m $\leq \Delta h <$ 1.25 m
Small storm surge	1.25 m $\leq \Delta h <$ 1.5 m
Severe storm surge	1.5 m $\leq \Delta h <$ 2.0 m
Moderate storm surge	2.0 m $\leq \Delta h$

2.8 Morphological and Hydrodynamic data

The study area is located at the Baltic Sea coastline near Ahrenshoop, Mecklenburg-Vorpommern, Germany (Figure 1.3). This site was selected due to its high susceptibility to erosion, data availability, and minimal anthropogenic disturbance. A narrow land bridge connects the Baltic Sea and the Saaler Bodden, making this coastal segment particularly critical for flood protection. The selected segment near KKM 183.000 is characterized by dynamic sediment transport processes, with long-term shoreline retreat rates between 1–2 m/year and annual sediment losses of up to 15 m³ per meter of coastline.

As part of the ResCAD project, detailed morphological data were collected through multiple high-resolution surveys. **UAV**-based **LiDAR** and photogrammetric measurements were conducted in March 2023 and April 2024 using a DJI Matrice M300 **RTK** equipped with a Riegl LiDAR sensor. These flights captured dune geometry, beach morphology, and topographic variation with high spatial accuracy, supported by RTK **GNSS** ground control

measurements. Stationary 4D-laserscanning using a Riegl Z420i scanner was tested in July 2023 from the rooftop of "The Grand" hotel in Ahrenshoop to monitor morphological changes in high temporal resolution during storm events.

Bathymetric data were compiled from **EOMAP** satellite-based surveys (October 2021–October 2023), AH5P topographic profiles (2021–2023), and Airbone Laser Scanning (**ALS**) data from March 2022 and September 2023. These were processed into topo-bathymetric Digitial Elevation Models (**DEMs**) using QGIS and open3D, with a target resolution of 1 m in regions with steep dune slopes.

Geotechnical investigations in March 2023 provided sedimentological data, revealing median grain sizes (D_{50}) ranging from 0.26 mm at the dune toe to 0.33 mm on the beach. These values align with previous studies and were used to define sediment transport parameters in the numerical model.

Hydrodynamic boundary conditions were derived from MIKE21 simulations of the Baltic Sea during the October 2023 storm event. Time series for wave height (H_{m0}), peak period (T_p), and wave direction were extracted at seaward boundaries and formatted into Joint North Sea Wave Project (**JONSWAP**) spectra. Maximum significant wave heights of 2.5 m and peak periods around 10 s were simulated for the Ahrenshoop coastline, with wave direction predominantly from the northeast. Water level data for the event were based on modeled and gauged values, reaching a maximum of approximately +1.7 m above Normalhöhennull (**NHN**).

This storm event (19–21 October 2023) caused visible morphological changes, including dune scarping and beach erosion. Photogrammetric surveys conducted immediately afterward revealed dune face angles exceeding 67°, surpassing typical stability thresholds and providing a valuable dataset for model calibration.

3 Literature Review

3.1 Software and Simulations Program

XBeach, developed by Roelvink et al. (2009), is a two-dimensional model designed to simulate wave propagation (including short and long waves), mean flow, sediment transport, and morphological changes in nearshore areas such as beaches, dunes, and back-barrier environments during storm events. The model enables detailed analysis of coastal dynamics under extreme hydraulic conditions.

XBeach is organized into four main modules (Figure 3.1): *Wave, Flow, Sediment Transport and Morphology*, which exchange data in sequence at each time step. The process begins with the short-wave module, which produces radiation stress gradients for the flow module.

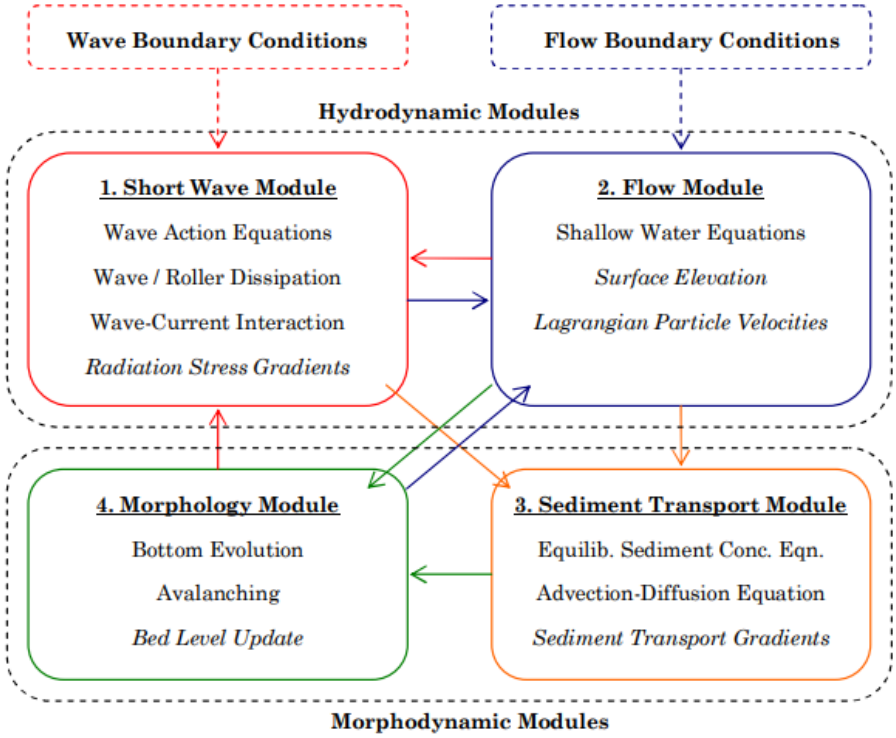

Figure 3.1: Component modules in XBeach. After Daly (2009)

Outputs from both modules, i.e., wave and current outputs, are used by the sediment transport module to calculate sediment movement, after which morphology is updated using flow and sediment transport data. In the following time step, the short-wave module incorporates changes in bed level and surface elevation from the morphology and flow modules. All hydrodynamic calculations are carried out within the short-wave and flow modules. Arrows in Figure 3.1 indicate connectivity, and terms in italics indicate relevant output parameters. The black dotted lines encompass the hydrodynamic (top) and morphodynamic (bottom) modules. Boundary conditions are applied only in the first cycle.

3.2 Hydrodynamics Options in XBeach

XBeach was originally developed as a short-wave averaged but wave-group resolving model. This design allows it to simulate short-wave variations on the scale of wave groups as well as the associated long waves. Since the publication by Roelvink et al. (2009), several additional model modes have been introduced, enabling users to choose the time-scale resolution best suited to their needs:

1. **Stationary wave model** (keyword: `wavemodel = stationary`): It solves wave-averaged equations efficiently while neglecting infragravity waves.
2. **Surfbeat mode** (keyword: `wavemodel = surfbeat)`: It resolves short-wave variations at the group scale and the corresponding long waves.
3. **Non-hydrostatic mode** (keyword: `wavemodel = nonh)`: It combines the non-linear shallow water equations with a pressure correction to simulate the propagation and decay of individual waves.

Reasons for using XBeach Surf-beat Approach in this Study

1. Xbeach works well for beaches where **IG** waves are dominant.
2. It is suitable for relatively deep, nearshore zone where short wave parameterization holds.
3. Surf-beat approach does not work well on steeper beaches and around steep structures. Ahreenshoop has relatively flat beach. So, Surf-beat approach should work well.

It is important to note that all time inputs in XBeach are specified in morphological time. When a morphological acceleration factor (*morfac*) is applied , all time series and time-related parameters are internally divided by this factor. This allows users to provide time values in real (physical) time and adjust the morphological acceleration independently, without modifying the input files `morfacopt = 1`. Figure 3.2 (left) illustrates how the wave models function (from top to bottom: Stationary, Surfbeat and Non-Hydrostatic) and Figure 3.2 (right) shows principle sketch of the relevant wave processes.

The wave models of XBeach deliver their best effectiveness for various application areas. Figure 3.3 shows in green where the strengths of XBeach lie for coastal types according to energy transformation (horizontal axis) and the section considered depending on its position in the cross-shore profile (vertical axis).

3.3 XBeach Modules

3.3.1 Flow Module

For the low-frequency and mean flows, the shallow water equations are used. To account for the wave-induced mass flux and the subsequent (return) flow, these are cast into a

depth-averaged Generalized Lagrangian Mean(**GLM**) formulation (Andrews & McIntyre, 1978; Walstra et al., 2000). In such a framework, the momentum and continuity equations are formulated in terms of the Lagrangian velocity u^L, which is defined as the distance a water particle travels in one wave period, divided by that period. This velocity is related to the Eulerian velocity (the short-wave-averaged velocity observed at a fixed point) by:

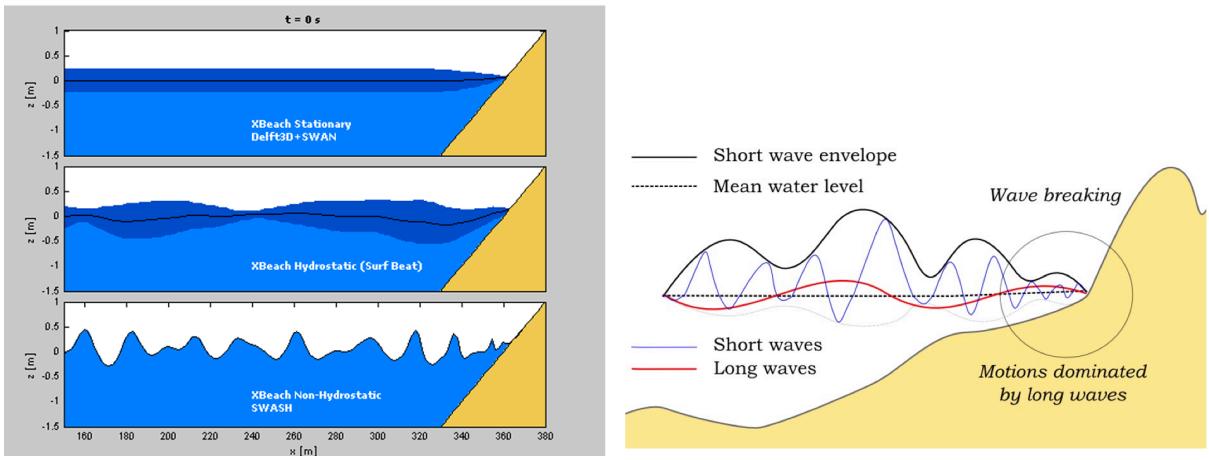

Figure 3.2: XBeach wave model options (left) and Principal sketch of relevant wave processes (right)

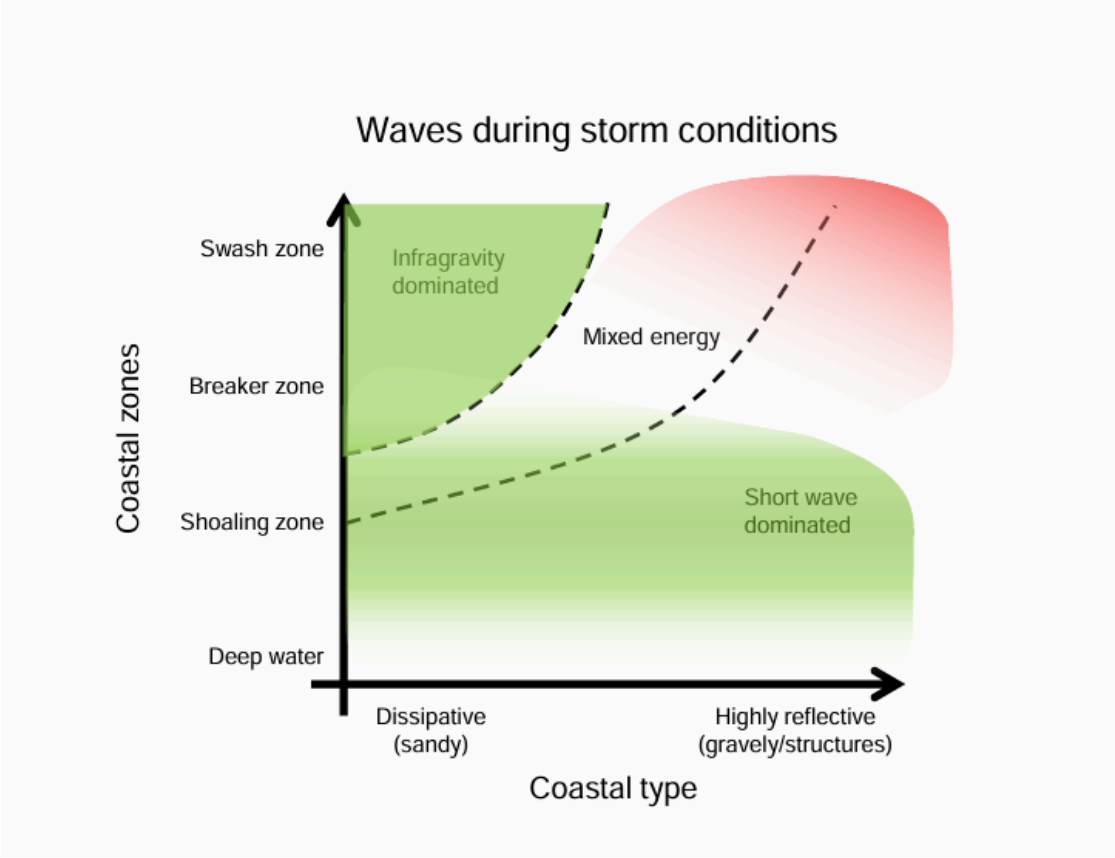

Figure 3.3: Application area of XBeach by coastal section and type of energy transformation, where green color suggests suitability, red color suggests unsuitability

$$u^L = u^E + u^S \text{ and } v^L = v^E + v^S \tag{3.1}$$

Here u^S, v^S reprsent the Stokes drift in x- and y- directions respectively (Phillips, 1977). They are formulated as:

$$u^S = \frac{E_w \cos\theta}{\rho h c} \text{ and } v^S = \frac{E_w \sin\theta}{\rho h c} \tag{3.2}$$

where the wave-group varying short-wave energy and direction are obtained from the wave-action balance Equation (3.7).

The resulting **GLM**-momentum equations are given by:

$$\begin{aligned} &\frac{\partial u^L}{\partial t} + u^L\frac{\partial u^L}{\partial x} + v^L\frac{\partial u^L}{\partial y} - fv^L - \nu_h\left(\frac{\partial^2 u^L}{\partial x^2} + \frac{\partial^2 u^L}{\partial y^2}\right) = \\ &\frac{\tau_{\text{sx}}}{\rho h} - \frac{\tau^E{}_{\text{bx}}}{\rho h} - g\frac{\partial \eta}{\partial x} + \frac{F_x}{\rho h} + \frac{F_{\text{v,x}}}{\rho h} \end{aligned} \tag{3.3}$$

$$\begin{aligned} &\frac{\partial v^L}{\partial t} + u^L\frac{\partial v^L}{\partial x} + v^L\frac{\partial v^L}{\partial y} + fu^L - \nu_h\left(\frac{\partial^2 v^L}{\partial x^2} + \frac{\partial^2 v^L}{\partial y^2}\right) = \\ &\frac{\tau_{\text{sy}}}{\rho h} - \frac{\tau^E{}_{\text{by}}}{\rho h} - g\frac{\partial \eta}{\partial x} + \frac{F_y}{\rho h} + \frac{F_{\text{v,y}}}{\rho h} \end{aligned} \tag{3.4}$$

$$\frac{\partial \eta}{\partial t} + \frac{\partial h u^L}{\partial x} + \frac{\partial h v^L}{\partial y} = 0 \tag{3.5}$$

Here τ_{bx}, τ_{by} are the bed shear stresses, η is the water level, F_x, F_y are the wave-induced stresses, ν_t is the horizontal viscosity and f is the Coriolis coefficient. The bottom shear stress terms are calculated with the Eulerian velocities as experienced by the bed:

$$u^E = u^L - u^S \text{ and } v^E = v^L - v^S \tag{3.6}$$

and not with the GLM velocities.

3.3.2 Wave Module

The model is driven by a time-dependent form of the wave action balance equation in shallow water, analogous to the approach used in the Hindcasting Shallow Water Waves (**HISWA**) model. It considers the directional distribution of the wave action density, while the frequency spectrum is represented by a single, representative frequency. The governing equation for wave action balance is given as:

$$\underbrace{\frac{\partial A}{\partial t}}_{\text{Wave action over time}} + \underbrace{\frac{\partial c_x A}{\partial x} + \frac{\partial c_y A}{\partial y}}_{\text{wave propagation in x and y}} + \underbrace{\frac{\partial c_\theta A}{\partial \theta}}_{\text{Refraction}} = \underbrace{-\frac{D_w + D_f + D_v}{\sigma}}_{\text{Dissipation}} \tag{3.7}$$

where D_w, D_f and D_v are the three short wave dissipation processes in XBeach: wave breaking, bottom friction and vegetation respectively. The wave action (A) is given as:

$$A(x, y, t, \theta) = \frac{S_w(x, y, t, \theta)}{\sigma(x, y, t)} \tag{3.8}$$

where S_w is the wave energy density in each directional bin, θ represents the angle of incidence of the wave with respect to the x-axis and σ is the intrinsic wave frequency. The wave-action propagation speeds in x- and y-directions are given by:

$$c_x(x, y, t, \theta) = c_g \cos\theta + u^L \tag{3.9}$$

$$c_y(x, y, t, \theta) = c_g \cos\theta + v^L \tag{3.10}$$

where u^L and v^L are the cross-shore and alongshore depth-averaged Lagrangian velocities respectively. The propagation speed in θ-space is obtained from:

$$\begin{aligned} c_\theta(x, y, t, \theta) = \frac{\sigma}{\sinh 2kh}\left(\frac{\partial h}{\partial x}\sin\theta - \frac{\partial h}{\partial y}\cos\theta\right) + \\ \cos\theta\left(\sin\theta\frac{\partial u}{\partial x} - \cos\theta\frac{\partial u}{\partial y}\right) + \sin\theta\left(\sin\theta\frac{\partial v}{\partial x} - \cos\theta\frac{\partial v}{\partial y}\right) \end{aligned} \tag{3.11}$$

and the group velocity is obtained from linear wave theory as

$$c_g = nc = \left(\frac{1}{2} + \frac{kh}{\sinh 2kh}\right)\frac{\sigma}{k} \tag{3.12}$$

where n is ratio of group velocity and phase velocity.

The wave number k is obtained from eikonal equations:

$$\frac{\partial k_x}{\partial t} + \frac{\partial \omega}{\partial x} = 0 \tag{3.13}$$

$$\frac{\partial k_y}{\partial t} + \frac{\partial \omega}{\partial y} = 0 \tag{3.14}$$

where the subscripts refer to the direction of wave vector components and ω represents the absolute radial frequency. The absolute radial frequency is then obtained from:

$$\omega = \sigma + k_x u^L + k_y v^L \tag{3.15}$$

And the intrinsic frequency is obtained from the linear dispersion relationship as:

$$\sigma = \sqrt{gk\tanh kh} \tag{3.16}$$

Wave Breaking and Dissipation

Five different wave breaking formulations are implemented in XBeach. The formulations can be selected using the keyword `break` as shown in Table 3.1.

Table 3.1: Different wave breaking formulations implemented

Wave breaking formula	Types of waves	Keyword
Roelvink (1993a	Instationary	`roelvink1`
Roelvink (1993a) extended	Instationary	`roelvink2`
Daly et al. (2010)	Instationary	`roelvink_daly`
Baldock et al. (1998)	Stationary	`baldock`
Janssen & Battjes (2007)	Stationary	`janssen`

The wave energy dissipation due to wave breaking is modelled according to Roelvink (1993) using the default command `break = 3`, which is also written as `break = roelvink2` as

$$\bar{D_{\mathrm{w}}} = 2\frac{\alpha}{T_{\mathrm{rep}}} E_{\mathrm{waves}}\, Q_{\mathrm{break}} \tag{3.17}$$

The fraction of breaking of waves is given by

$$Q_{\mathrm{break}} = 1 - \exp\left(-\left(\frac{H_{\mathrm{rms}}}{H_{\mathrm{max}}}\right)^{n}\right), H = \sqrt{\frac{8E_{\mathrm{waves}}}{\rho g}}, H_{\mathrm{max}} = \gamma.(h + \delta H_{\mathrm{rms}}) \tag{3.18}$$

with $\alpha = O(1)$, T_{rep} the representative wave period, H_{rms} root mean squared wave height, ρ the water density, γ the breaker index and the total wave energy is given by:

$$E_{\mathrm{waves}}\,(x, y, t) = \int_{0}^{2\pi} S_w(x, y, t, \theta) d\theta \tag{3.19}$$

Finally the total wave dissipation distributed proportionally over the wave directions is calculated as

$$D_w(x, y, t, \theta) = \frac{S_w(x, y, t, \theta)}{E_{\mathrm{waves}}} \bar{D_{\mathrm{w}}}(x, y, t) \tag{3.20}$$

Daly et al. (2012) found that Roelvink's equations [Equation (3.17)] and [Equation (3.18)] underestimated wave-breaking dissipation in complex terrains with rapidly increasing water depth. Daly's equation, developed to address this limitation, is identical to Roelvink's except for incorporating a binary wave-breaking probability and an advective–deterministic approach, allowing on–off breaking calculations based on wave height, even in sharply varying depths. It also includes the gamma2 (γ_2) parameter, which sets the threshold at which irregular wave breaking ceases, improving prediction accuracy in such environ-

ments. Experimental validation showed that Daly's equation significantly outperformed Roelvink's in complex bathymetry.

In XBeach 1.24.6057 Halloween version, the default break formulation is `break = 4` or `break = roelvink_daly`, as described by Roelvink et al. (2009). This approach switches breaking on or off according to:

$$\begin{aligned} H_{\text{rms}} > \gamma h \rightarrow Q_{\text{break}} = 1 \\ H_{\text{ rms}} < \gamma_2 h \rightarrow Q_{\text{break}} = 0 \end{aligned} \tag{3.21}$$

where h is local water depth. Breaking therefore occurs only when H/h is between γ and γ_2, avoiding a partial probabilistic estimate of wave breaking.

3.3.3 Sediment Transport Module

XBeach calculates sediment concentration using the water depth-averaged advection-diffusion equation to simulate sediment transport (Galappatti & Vreugdenhil, 1985)

$$\frac{\partial hC}{\partial t} + \frac{\partial hC_u^E}{\partial x} + \frac{\partial hC_v^E}{\partial y} + \frac{\partial}{\partial x}\left[D_h h \frac{\partial C}{\partial x}\right] + \frac{\partial}{\partial y}\left[D_h h \frac{\partial C}{\partial y}\right] = \frac{hC_{\text{eq}} - hC}{T_s} \tag{3.22}$$

where C indicates the instantaneous concentration of the depth- averaged sediment, D_h indicates the diffusion of sediment, h indicates the water depth, u^E and v^E indicate the x and y components in the Euler flow velocity, C_{eq} indicates the equilibrium concentration of sediments, and T_s indicates the reaction time due to entrainment. T_s is given by a simple approximation based on the local water depth (h) and sediment fall velocity w_s as

$$T_s = \max\left(f_{T_s}\frac{h}{w_s}, T_{s,\min}\right)s \tag{3.23}$$

3.3.4 Morphology module

Based on the gradients in the sediment transport, the bed level is updated as:

$$\frac{\partial z_b}{\partial t} + \frac{f_{\text{mor}}}{1-p}\left(\frac{\partial q_x}{\partial x} + \frac{\partial q_y}{\partial y}\right) = 0 \tag{3.24}$$

where p is the porosity, f_{mor} is a morphological acceleration factor and q_x and q_y represent the sediment transport rates in x- and y-directions respectively, given by:

$$\begin{aligned} q_x(x,y,t) = \left[\frac{\partial hCu^E}{\partial x}\right] + \frac{\partial}{\partial x}\left[D_h h \frac{\partial C}{\partial x}\right] \\ q_y(x,y,t) = \left[\frac{\partial hCv^E}{\partial y}\right] + \frac{\partial}{\partial y}\left[D_h h \frac{\partial C}{\partial y}\right] \end{aligned} \tag{3.25}$$

where D_h is the sediment diffusion coefficient and C is the depth-averaged sediment concentration.

The morphological acceleration factor f_{mor} (keyword: *morfac*), typically of order O(1–10) [Reniers et al., 2004], controls the temporal resolution of the bed change. Sediment transport rates in the x- and y-directions, q_x and q_y define the gradients in the second term. Sediment transport can be activated with the keyword *sedtrans*.

The default sediment transport formulations in XBeach 1.24.6057 are the Van Thiel-Van Rijn equations (Roelvink et al., 2009; Walstra et al., 2007) (keyword: `form = vanthiek_vanrijn`). The equilibrium sediment concentrations are calculated according to:

$$\begin{aligned} C_{\text{eq,b}} &= \left(\frac{A_{\text{sb}}}{h}\left(\sqrt{{v^2}_{\text{mg}} + 0.64{u^2}_{\text{rms,2}}} - U_{\text{cr}}\right)\right)^{1.5} \\ C_{\text{eq,s}} &= \left(\frac{A_{\text{ss}}}{h}\left(\sqrt{{v^2}_{\text{mg}} + 0.64{u^2}_{\text{rms,2}}} - U_{\text{cr}}\right)\right)^{2.4} \end{aligned} \tag{3.26}$$

where U_{crc} is critical velocity for currents and U_{crw} is critical velocity for waves. The bed-load and suspended load coefficient (A_{sb} and A_{ss}) are calculated with:

$$A_{\text{sb}} = 0.015h\frac{\left(\frac{D_{50}}{h}\right)^{1.2}}{\left(\Delta g D_{50}\right)^{0.75}}, A_{\text{ss}} = 0.012D_{50}\frac{D_*^-0.6}{\left(\Delta g D_{50}\right)^{1.2}} \tag{3.27}$$

The critical velocity is computed as weighted summation of the separate contributions by currents and waves:

$$U_{\text{cr}} = \beta U_{\text{crc}} + (1-\beta)U_{\text{crcw}} \text{ in which } \beta = \frac{v_{\text{mg}}}{v_{\text{mg}} + u_{\text{rms}}} \tag{3.28}$$

The velocity magnitude (v_{mg}) is calculated as

$$v_{\text{mg}} = \sqrt{\left(u^E\right)^2 + \left(v^E\right)^2} \tag{3.29}$$

And the dimensionless sediment parameter D_* is calculated with the following formulation:

$$D_* = \left(\frac{\Delta g}{\nu^2}\right)^{\frac{1}{3}} D_{50} \tag{3.30}$$

The critical velocity for currents is based on Shields (1936) as below:

$$U_{\text{crc}} = \begin{cases} 0.19 D_{50}^{0.1} \log 10\left(\frac{4h}{D_{90}}\right) \text{ for } D_{50} \leq 0.0005 \\ 8.5 D_{50}^{0.6} \log 10\left(\frac{4h}{D_{90}}\right) \text{ for } D_{50} \leq 0.002 \\ 1.3\sqrt{\Delta g D_{50}}\left(\frac{h}{D_{50}}\right)^{\frac{1}{6}} \text{ for } D_{50} > 0.0005 \end{cases} \tag{3.31}$$

The critical velocity for waves is based on Komar & Miller (1975) is below:

$$U_{\text{crw}} = \begin{cases} 0.24(\Delta g)^{\frac{2}{3}} (D_{50} T_{\text{rep}})^{\frac{1}{3}} \text{ for } D_{50} \leq 0.0005 \\ 0.95(\Delta g)^{0.57} (D_{50})^{0.43} {T_{\text{rep}}}^{0.14} \text{ for } D_{50} > 0.0005 \end{cases} \tag{3.32}$$

Xbeach also models avalanching with sediment exchange between adjacent cells when critical wet and dry slope thresholds (m_{cr}) are exceeded:

$$\begin{aligned} \left|\frac{\partial z_b}{\partial x}\right| &> m_{\text{cr}} \\ \left|\frac{\partial z_b}{\partial y}\right| &> m_{\text{cr}} \end{aligned} \tag{3.33}$$

3.4 Sensitivity Analysis

Sensitivity analysis is a systematic approach used to determine how uncertainty in model outputs can be attributed to different sources of uncertainty in model inputs (Confalonieri et al., 2010). The main goal of sensitivity analysis is to identify which parameters most strongly affect the outcomes, thereby guiding model calibration, prioritizing data collection and quantifying overall uncertainty. An overview of the methods of sensitivity analysis is provided in Table 3.2.

3.5 Latin Hypercube Sampling Method

To decrease the number of model runs needed in a probabilistic sensitivity analysis, variance-reducing techniques can be applied. One such approach is **LHS**. In this method, the range of each variable is divided into N intervals of equal probability (Kurowicka & Cooke, 2006; McKay et al., 2000). It is shown in Figure 3.4. Using the cumulative probability distribution, the probability density function is partitioned into bins of equal probability. From each bin, a single value is randomly chosen for every parameter, after which random combinations of these values are created. Because the sampling procedure is guided in this way, the samples are more evenly distributed compared to crude Monte Carlo sampling. As a result, fewer samples are sufficient (Kurowicka & Cooke, 2006; McKay et al., 2000)

Table 3.2: Characteristics of selected sensitivity methods based on Arkel (2016)

Method	**Description**
One at a Time (**OAT**)	• A single parameter is altered while all others are kept constant.
Morris	• One parameter is altered at a time with variation in the base case, allowing information about linearity and parameter interactions to be obtained.
Factorial Design	• Multiple parameters are systematically varied across all (or a subset of) their possible levels. • Interactions among parameters can be quantified, although this approach may be computationally expensive.
Probabilistic Methods	• Crude Monte Carlo (**MC**): Input parameters are randomly sampled from their probability distributions; large sample sizes are typically required for accuracy. • LHS: A variance-reducing alternative to crude MC, in which samples are uniformly distributed across the parameter range. Each stratum of the distribution is sampled exactly once, ensuring more comprehensive coverage with fewer samples.

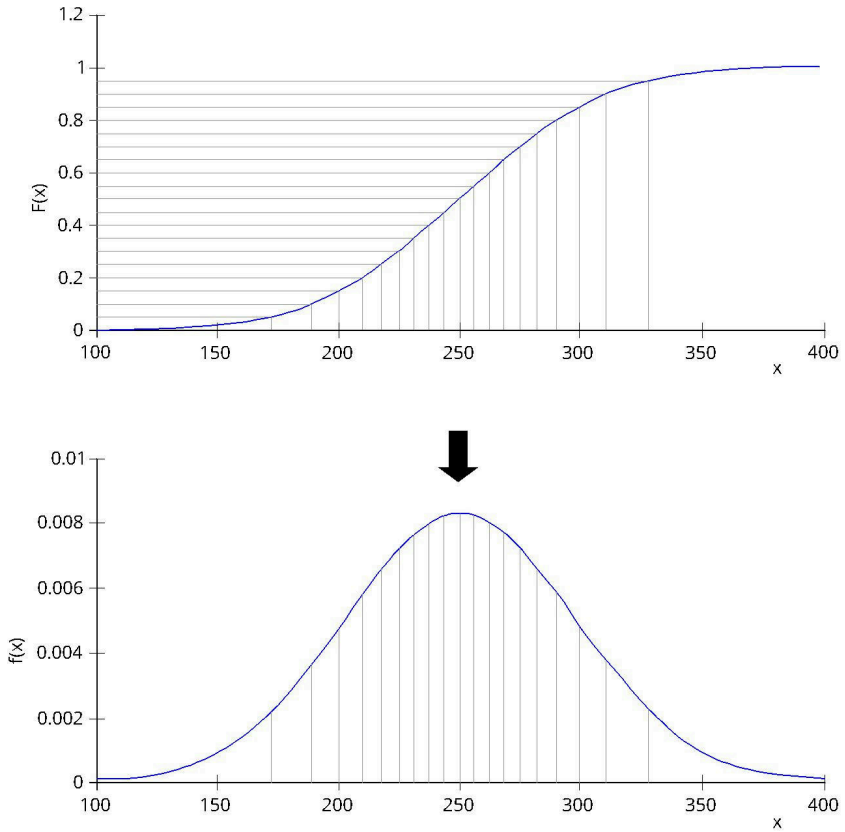

Figure 3.4: Visual representation of Latin Hypercube Sampling. After (Arkel, 2016)

In this study, the LHS method of sensitivity analysis was applied. The reasons for employing this method, based on the study conducted by Arkel (2016), are as follows:

- LHS allows for more efficient and systematic sampling of the input parameter space than crude MC. It ensures that each part of the parameter range is represented, thereby reducing the number of simulations required for reliable results.
- Arkel (2016) reported that LHS is "a factor $\sim$5 faster than the benchmark" (the benchmark being an extensive MC analysis), while maintaining similar accuracy, particularly in terms of output distributions and parameter sensitivity rankings.
- LHS performs better with nonlinear or interacting parameters compared to simpler deterministic approaches, making it suitable for coastal environment models where processes are complex and uncertainties are high.
- Probabilistic methods, particularly LHS, provide more reliable estimates of model output variability and parameter importance (i.e., which inputs most strongly affect outputs), especially when parameters are uncertain and their interactions are significant.

3.6 Selected XBeach parameters for this Study

Several morphodynamic models have been developed to simulate dune erosion, among which SBEACH, CSHORE, and XBeach are widely applied. For the hydro-morphodynamic investigations carried out in this study, the open-source numerical model **XBeach 1.24.6057 Halloween** was employed The XBeach model was developed to simulate the impact of extreme events on dune coasts. It is a process-based model, which makes it more complex and computationally more intense than equilibrium-type models (Ciavola et al., 2014). It has approximately 100 parameters that can be significant and that should be specified in the calibration process. From the model calibration in the study done by Schweiger et al. (2020), the study being a large-scale field experiment at the beach of Rostock-Warnemünde, the most influential parameters were identified as *facua*, the Manning bed friction coefficient n_M, the critical bed slope for wet cells *wetslp*, the break index *gamma* the initial porosity *por* and $h_{\min}$, defining the minimum water depth from which the Stokes drift is included in order to prevent excessively strong return flows during the simulation. So, in this study, the parameters *facua*, *gamma* and *por* were selected. In addition to this, another parameter *gamma2* was selected because the break formulation used by the version of the used XBeach in this study uses *gamma2* also. This approach switches breaking on or off according to Equation (3.21) explained in Section 3.3.2. The parameter related to directional resolution (*dtheta*) and the angle with which waves attack the model domain are also studied. A brief information about the above mentioned parameters is presented in Table 3.3 with default values, short description and the range offered by the adopted version of XBeach in this study.

Table 3.3: Definition, range and default value of selected parameters

Parameter	**Description**	**Range**	**Default value**
facua	The degree to which wave tilt and asymmetry affect sediment transport direction	0.0 - 1.0	0.175
gamma	Breaker parame ter in baldock or roelvink formulation	0.4 −0.9	0.46
gamma2	End of breaking pa rameter in *roelvink_daly* formulation	0.0 - 0.5	0.34
por	Porosity	0.3 - 0.5	0.4
morfac	Morphological acceleration factor	0.0 - 1000.0	10
dtheta	Directional resolution	0.1 - 180.0	10.0

4 Methodology

4.1 Generalized Likelihood Uncertainty Estimation (GLUE)

The **GLUE** methodology, first introduced by Beven & Binley (1992), has become a widely applied framework for uncertainty assessment in environmental and hydrological modeling. Its foundation lies in the concept of equifinality, which acknowledges that multiple parameter sets may yield simulations consistent with observed system behavior. Unlike traditional calibration approaches that focus on a single "best-fit" solution, GLUE accepts a range of parameter sets as behavioural, provided they meet a chosen likelihood measure. This flexibility makes it especially valuable for complex, nonlinear systems such as coastal and catchment models, where uncertainties in parameters, inputs, and model structure are unavoidable. Figure 4.1 shows the flow chart of GLUE process.

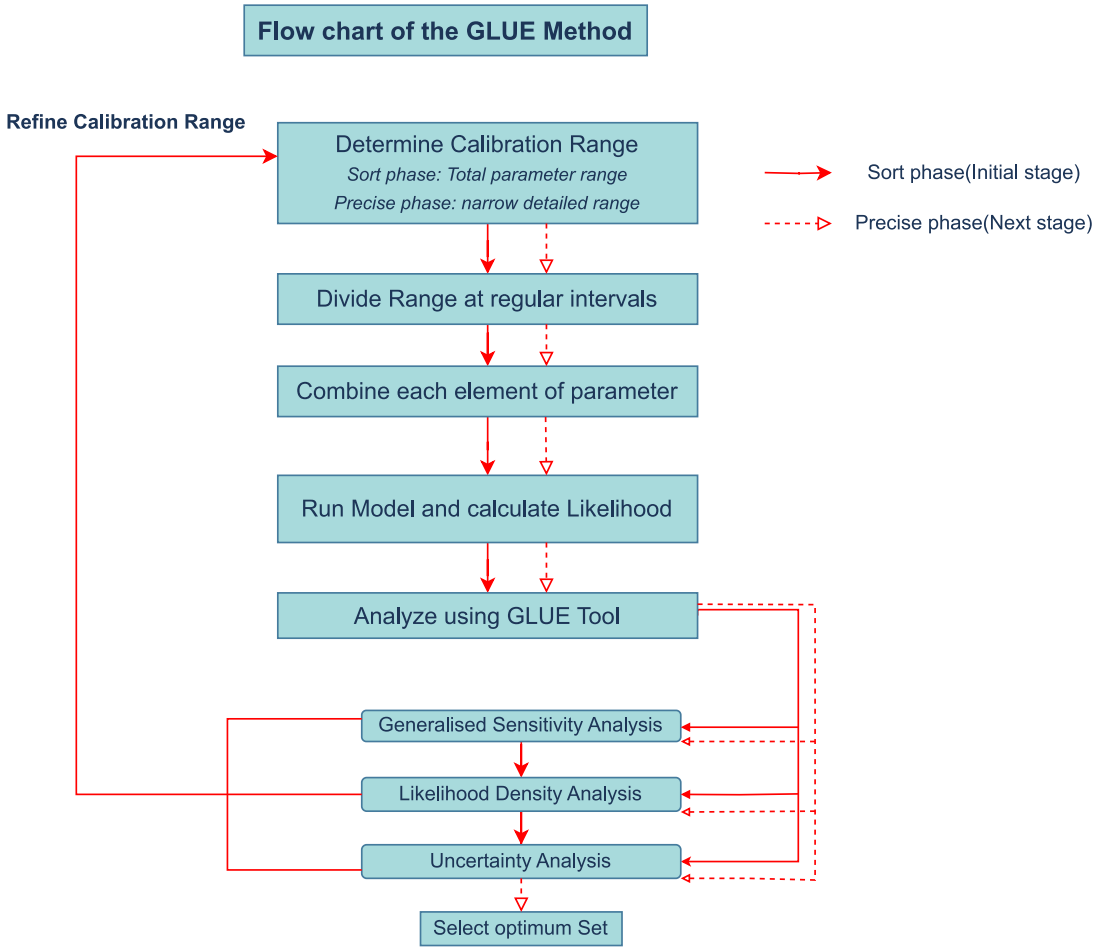

Figure 4.1: Flow chart of GLUE process. After Bae et al. (2022)

Within GLUE, Monte Carlo sampling is employed to explore the parameter space. Each sampled parameter set is tested against observational data, and those meeting predefined performance criteria are retained as behavioural. The distribution of these behavioural sets then provides probabilistic insights into prediction uncertainty. In coastal engineering, this framework has been shown to effectively capture model uncertainty, supporting both sensitivity analysis and robust uncertainty quantification (Bae et al., 2022; Simmons, 2018).

A critical step in this process is defining an evaluation metric to distinguish between behavioural and non-behavioural runs. The Brier Skill Score (**BSS**), originally proposed by Rijn et al. (2003), is widely used in coastal applications as a quantitative measure of predictive skill. It evaluates the accuracy of simulated cross-shore changes by comparing predicted and observed post-storm water depths, relative to pre-storm measurements as shown in Equation (4.1).

$$\mathrm{BSS} = \frac{\sum\left(\left|z_m - z_p\right|\right)^2}{\sum\left(\left|z_m - z_r\right|\right)^2} \tag{4.1}$$

Here, z_m is the observed post-storm depth, z_p is the simulated post-storm depth, and z_r is the pre-storm reference depth. Model performance according to **BSS** is summarized in Table 4.1, following the classification of Rijn et al. (2003).

Table 4.1: Model performance based on BSS

BSS range	Model Performance
0.8 ≤ BSS < 1.0	Excellent
0.6 ≤ BSS < 0.8	Good
0.3 ≤ BSS < 0.6	Fair/Reasonable
0 ≤ BSS < 0.3	Poor
BSS < 0	Bad

Bae et al. (2022) applied this approach in their study, noting that the large number of simulations inherent to GLUE necessitated a quantitative standard for identifying significant outcomes. To address this, they defined behavioural runs as those for which the mean BSS across baseline profiles exceeded 0.3 as shown in Equation (4.2).

$$\begin{aligned} &\text{behavioural run if } \frac{\sum_{i=1}^{n} BSS_i}{N} \geq 0.3 \\ &\text{non-behavioural run if } \frac{\sum_{i=1}^{n} BSS_i}{N} < 0.3 \end{aligned} \tag{4.2}$$

After behavioural runs were identified, a weighted likelihood was assigned to each parameter combination to resolve equifinality. In this context, likelihood quantified the

probability that a parameter set would yield an optimal simulation of the observed event. All non-behavioural runs were assigned a likelihood of zero, while behavioural runs were weighted proportionally to their BSS values as shown in Equation (4.3).

$$\text{Likelihood}_{\text{BSS}} = \frac{BSS_i}{\sum_{i=1}^{n} BSS_i} \tag{4.3}$$

Here, n is the number of behavioural parameter combinations, and BSS_i is the BSS value of the i-th behavioural run. This weighting provided a transparent basis for parameter evaluation and posterior uncertainty analysis within the GLUE framework.

Figure 4.2 shows methodology adopted in this study regarding how LHS and GLUE were applied for inital set of simulations. First, selected parameters were equally divided into 50 equal intervals and then 50 random set of simulations were made using LHS technique. The script used for generating LHS based runs is shown in Appendix A. Overview of 50 set of runs obtained from LHS technique is shown in Table C.1.

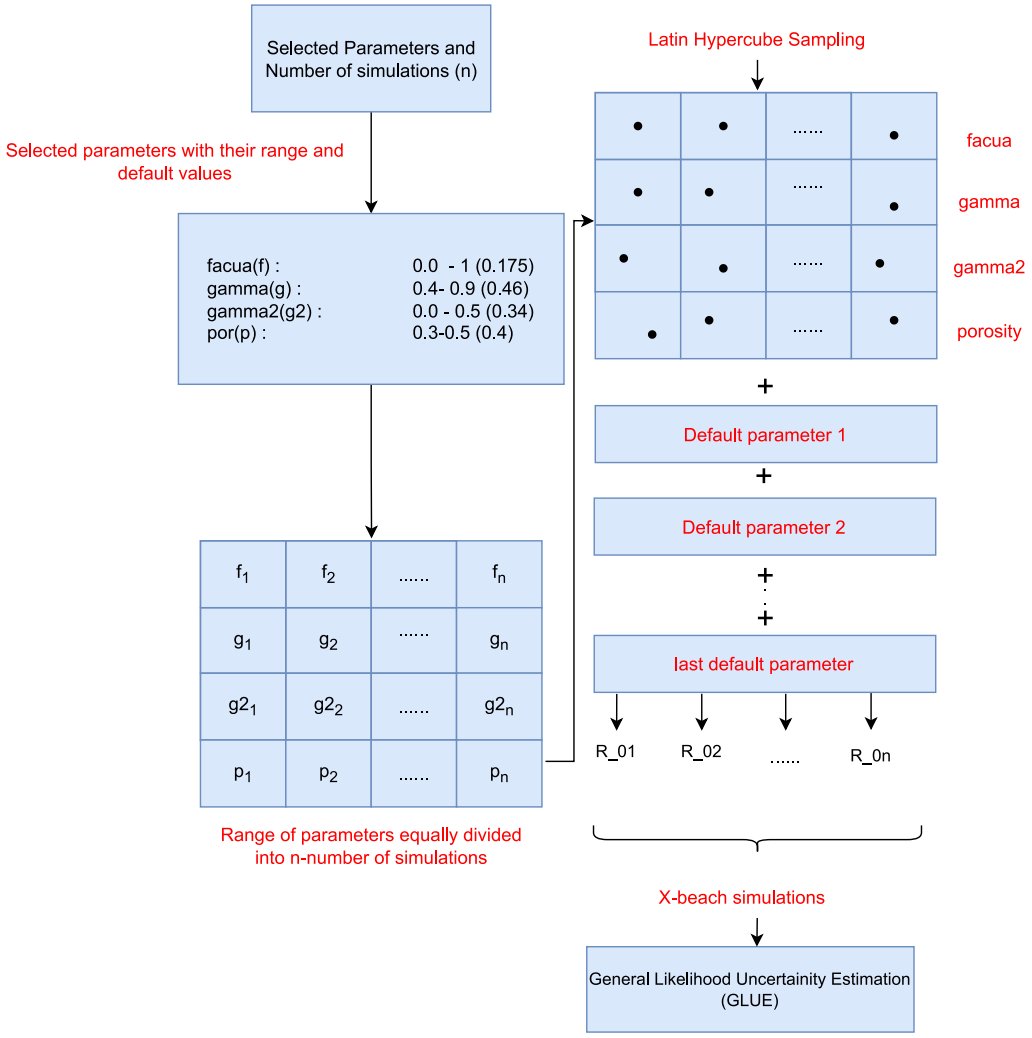

Figure 4.2: Methodology adopted for the initial set of simulations

4.2 Parameter Sensitivity Analysis based on Statistics

As a first step toward parameter sensitivity evaluation, a statistical approach was applied using LHS. The plan was to generate an ensemble of 50 simulations in order to capture the variability of XBeach input parameters within realistic ranges and explore their influence on model performance.

For each completed run, model skill was quantified using three performance metrics: BSS, the root mean square error (**RMSE**) and erosion volume differences. Pairwise parameter–metric dependencies were examined using Pearson correlation coefficients (r). Although the true parameter–response relationships were expected to be nonlinear, linear regression was applied as a diagnostic tool to approximate local trends and to provide an interpretable measure of direction and strength of association. Scatter plots with regression lines, r-values, and p-values were produced to visualize these tendencies. In addition, a correlation matrix was computed to summarize dependencies across the entire parameter–metric space.

4.3 Generalized Sensitivity Analysis (GSA)

Building on the likelihood weighting, **GSA** is performed to assess the relative influence of input parameters. The approach follows Hornberger and Spear (1981), as extended within the GLUE framework by Beven & Binley (1992). Sensitivity is evaluated by comparing the likelihood-weighted Cumulative Distribution Function (**CDF**) of each parameter with its prior uniform distribution. The Kolmogorov–Smirnov D-statistic (**K-SD**) is used to quantify the maximum difference between the two distributions. A K-SD close to 0 indicates low sensitivity, whereas values approaching 1 reflect strong sensitivity (Thorndahl et al., 2008).

In addition, Probability Density Functions (**PDFs**) of the cumulative likelihoods are examined to identify parameter ranges associated with higher model performance. This procedure enables a more objective determination of influential parameters, reducing uncertainty by highlighting regions of the parameter space that consistently produce significant predictions.

4.4 XBeach Model Setup

The XBeach workflow has basically three sequential stages. First is pre-processing, where the model domain is defined, grids are built, inputs and boundary conditions are prepared, and parameters are configured. Second is processing, in which the simulations are executed. Third is post-processing, where results are analyzed and visualized to interpret model behavior. Figure 4.3 outlines the key tasks and information flow within each stage.

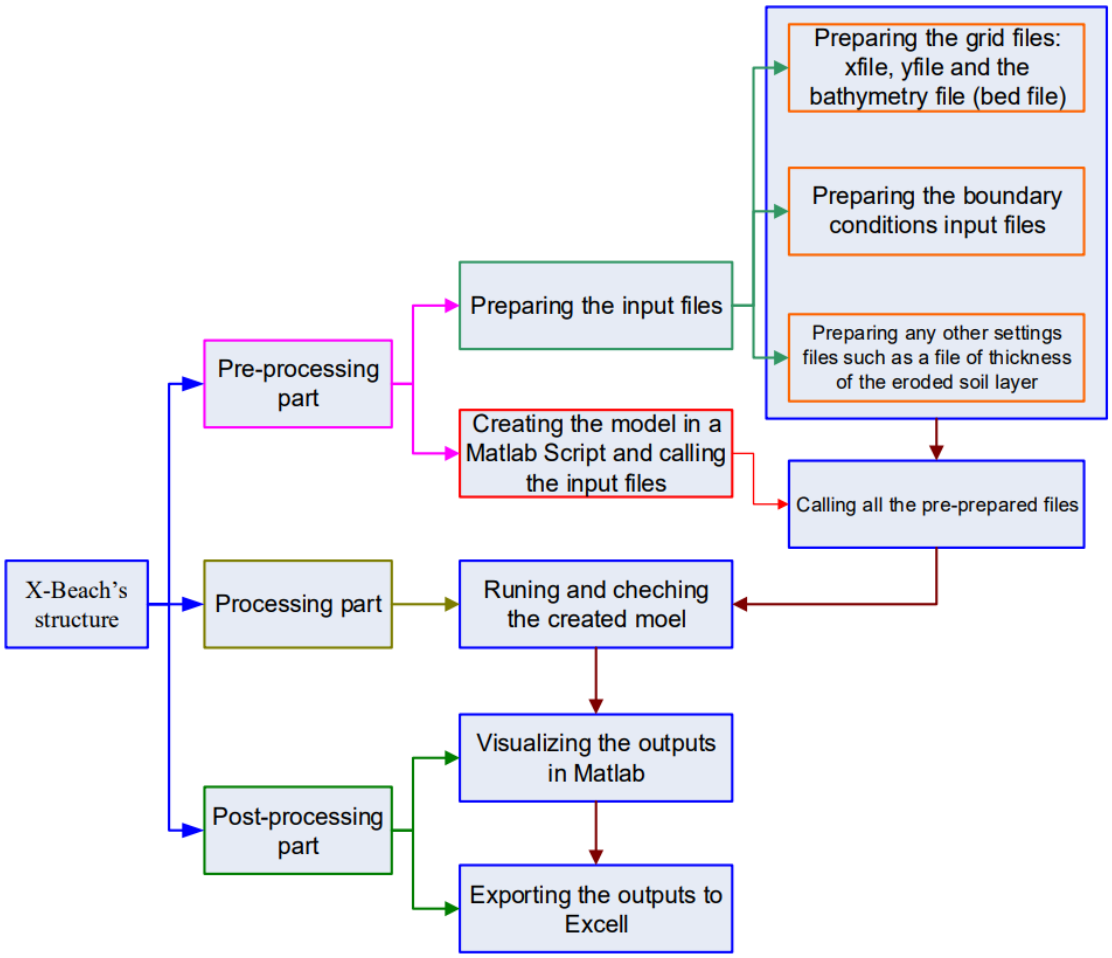

Figure 4.3: Stages of Modeling in XBeach. After Abdelaal & Oumeraci (2016)

4.5 Pre-Processing Phase

4.5.1 Topo Bathymetry

Bathymetry describes the topographic shape of waterbody floors. During an extreme event, the dune body is only partially submerged, and erosion also occurs in the non-submerged area, for example through slope failure. For this reason, XBeach often refers to topo-bathymetry rather than bathymetry, since the terrain area above the water surface is also included in the modeling.

Within the ResCAD project, the geodetic coordinate system **ETRS89** / **UTM** Zone 33N (**EPSG**: 25833) is consistently used. Elevation data are provided in sea-level-related heights according to the Deutsches Haupthöhennetz 2016 (**DHHN2016**) in the unit m üNHN. The topo-bathymetry of the study area is discussed in the following sections.

4.5.2 Grid Construction

The fundamental concept of computational grids in XBeach models is illustrated in Figure 4.4. XBeach generally operates with curvilinear grids, while a rectangular grid is treated

as a special case. A computational grid has four boundaries with equal cell numbers on opposite sides, though the cell size may vary. XBeach also supports the use of Delft3D grids.

In Figure 4.4, the offshore boundary is shown in blue, where wave boundary conditions are imposed. The landward boundary is marked in red, and the lateral boundaries are shown in orange. The grid origin $(x_{\text{ori}}, y_{\text{ori}})$ is defined at the outer corner of the offshore boundary (left-hand corner when viewed from land) and corresponds to node X_{11}. Grid indices are denoted by m in the alongshore and n in the cross-shore direction. The angle α specifies the rotation of the computational grid relative to the world-coordinate axis and is essential for correctly georeferencing input and output data such as hydrodynamics, bathymetry, and simulation results.

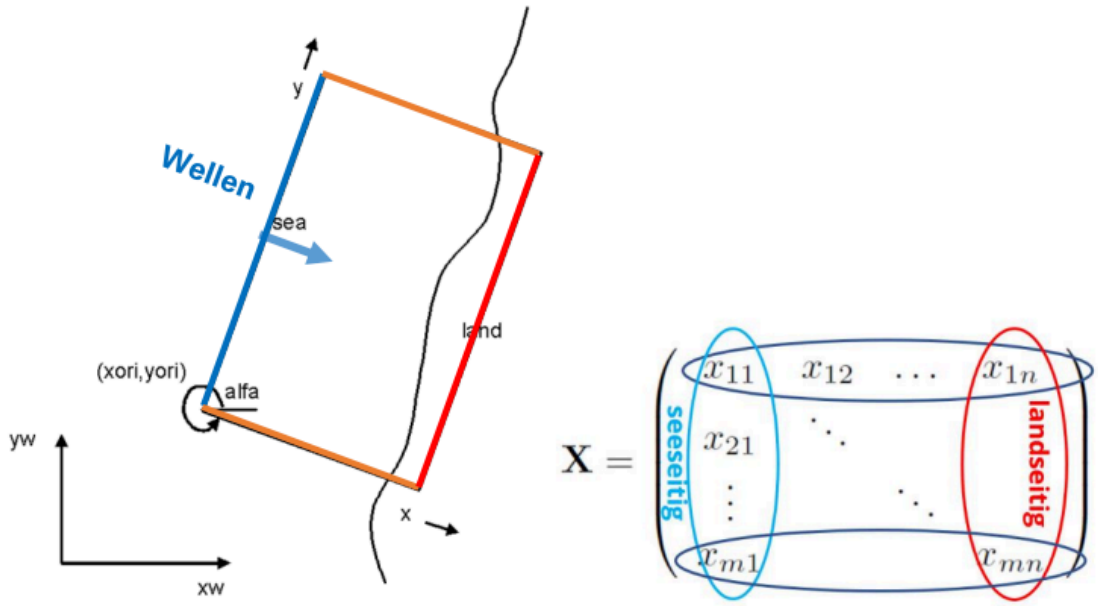

Figure 4.4: Basic concept of computational grids in XBeach, adapted from ResCAD A

The computational grid was constructed in a rectangular configuration, aligned to the coastline following the XBeach convention where the x-axis represents the cross-shore direction (pointing landward) and the y-axis denotes the alongshore direction.

First, the central profile was defined using landward and offshore points extracted from measured post-storm survey data. From these coordinates, the shoreline orientation angle (α) was calculated with respect to the eastward world-coordinate axis. The landward boundary point was shifted 50 m inland to ensure that the model domain fully encompassed the coastal dune area.

Based on this orientation, a local coordinate system was established by translating the shoreline point to the model origin $(x_{\text{ori}}, y_{\text{ori}})$ and rotating all bathymetric data such that the

computational axes were perpendicular and parallel to the coast. This allowed a consistent definition of a rectangular grid in local space that was then mapped to world coordinates through the origin and angle α.

A computational domain spanning 520 m cross-shore and 1400 m alongshore was fixed first (Figure 4.12). The initial grid resolution was set to $\Delta x = 10$ m in the cross-shore and $\Delta y = 10$ m in the alongshore direction, resulting in $nx = 52$ and $ny = 140$ cells, respectively. To better capture nearshore processes and dune morphology, the grid size was subsequently varied in both directions. In the cross-shore direction, the coarse grid was refined using the MATLAB function `xb_grid_xgrid()`, where the cell size was dynamically adjusted based on the Courant–Friedrichs–Lewy(**CFL**) condition, the representative peak wave period and a prescribed minimum grid size. This refinement produced cell sizes as small as 2 m near the shoreline, while allowing coarser spacing offshore. In the alongshore direction, the function `xb_grid_ygrid()` was applied to introduce a grading function, yielding finer resolution in the central region of interest and smoother coarsening toward the lateral boundaries.

The retrofitting step, in which bathymetric elevations were re-interpolated to the refined grid, significantly improved the quality of the computational mesh. The resulting size-varying grid preserved numerical stability while providing the spatial resolution required to represent key coastal features such as the dune foot and nearshore sandbars, thereby enhancing the model's ability to capture wave transformation and dune erosion processes. A cross section across the middle of the grid is shown in Figure 4.5 with original grid points and matlab fitted grid points. The optimised computational grid is shown in Figure 4.7

The measured bathymetry for the selected region with size varying cells is shown in Figure 4.8. This visualizes the very gentle nearshore slope off Ahrenshoop: even 400 m from the shoreline, depths reach only about 4–5 m. Pronounced sandbars are also evident and can be expected to enhance wave dissipation.

Figure 4.9 represents the next step in constructing the bathymetry, applying seaward deepening and smoothening. Beyond the offshore limit of the measured profile, the bed was linearly deepened towards the open boundary using a constant geometric slope of 0.05. This is necessary to achieve the water depth required for the XBeach simulation so that imposed waves do not break immediately at the seaward boundary if they are too high or too long.

The minimum water depth required for imposing wave and boundary conditions can be determined from the two panels in Figure 4.6. The selected minimum depth of 12.5 m is therefore within a safe range for the wave height and remains acceptable for the peak period. The adjusted model spans only 700 m in the cross-shore direction. Because water

levels during the storm surge are 1.0–1.5 m higher and values decrease landward, the chosen minimum depth is on the safe side.

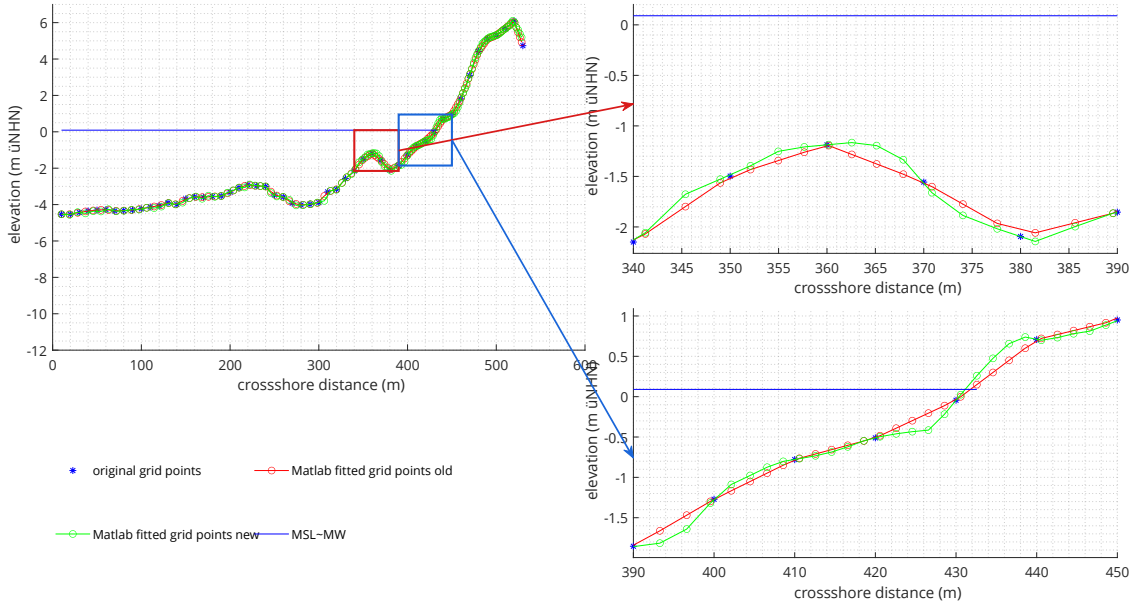

Figure 4.5: Observation of grid fitting with Matlab

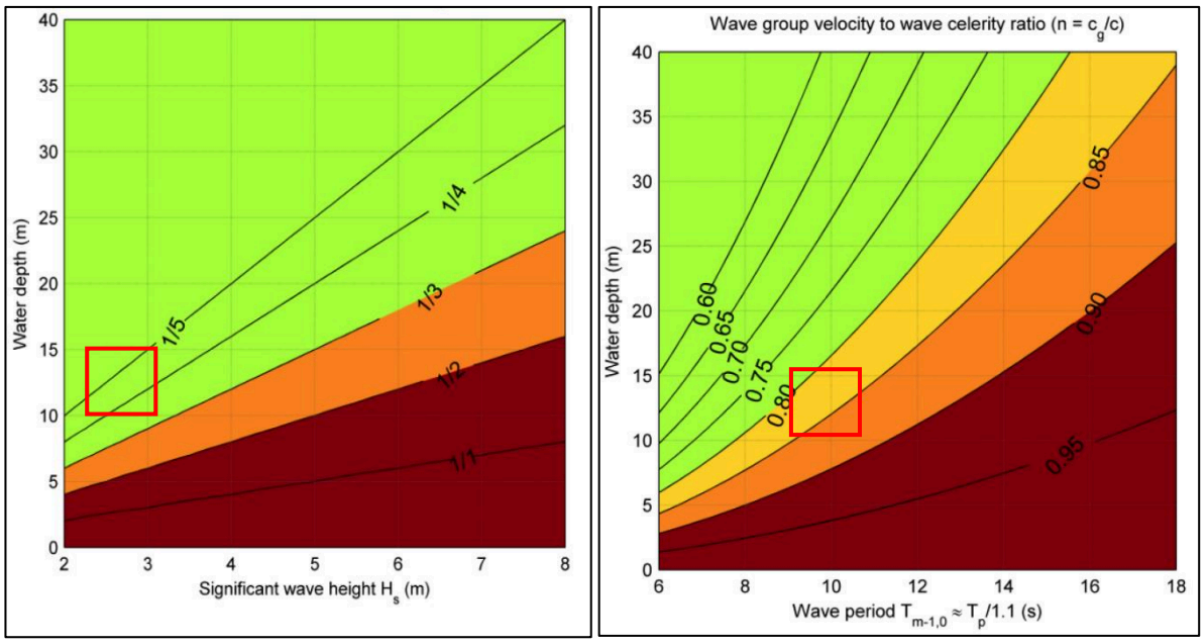

Figure 4.6: Hydrodynamic criteria for minimum water depth. Left: Significant wave height ~ 2.5 m, right: Peak period ~ 10 s. After ResCAD project

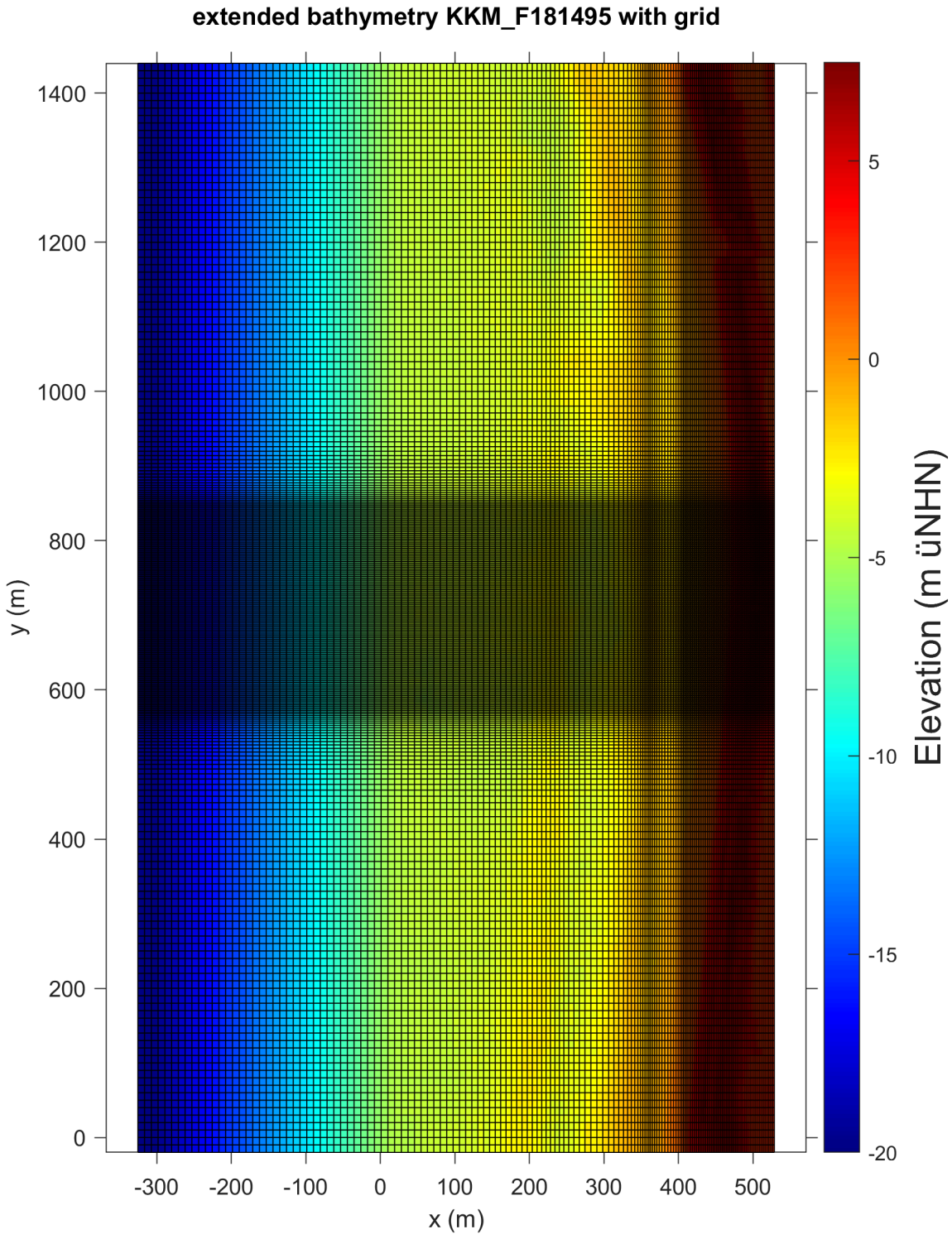

Figure 4.7: Extended and optimized computational grid

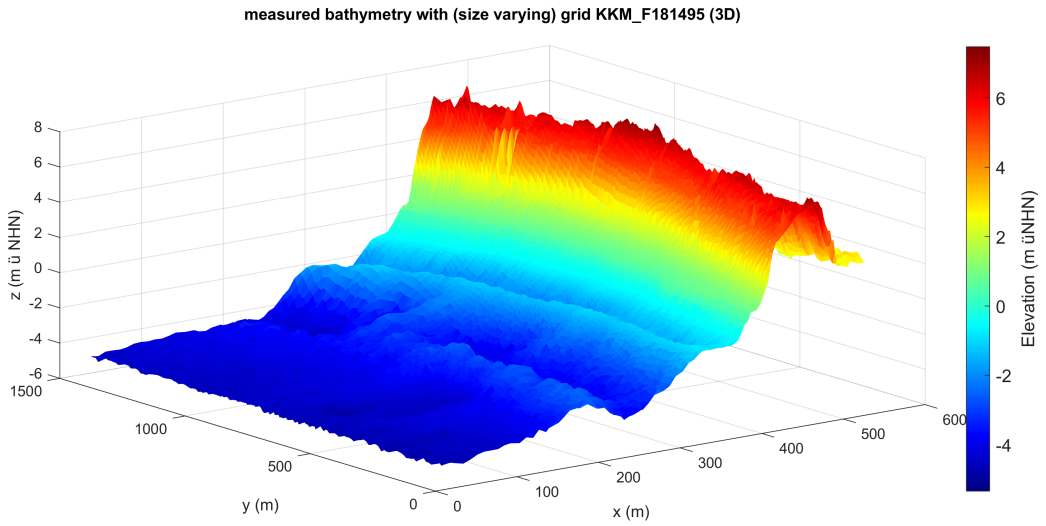

Figure 4.8: Constructed bathymetry (size varying) from existing measurement data in 3D

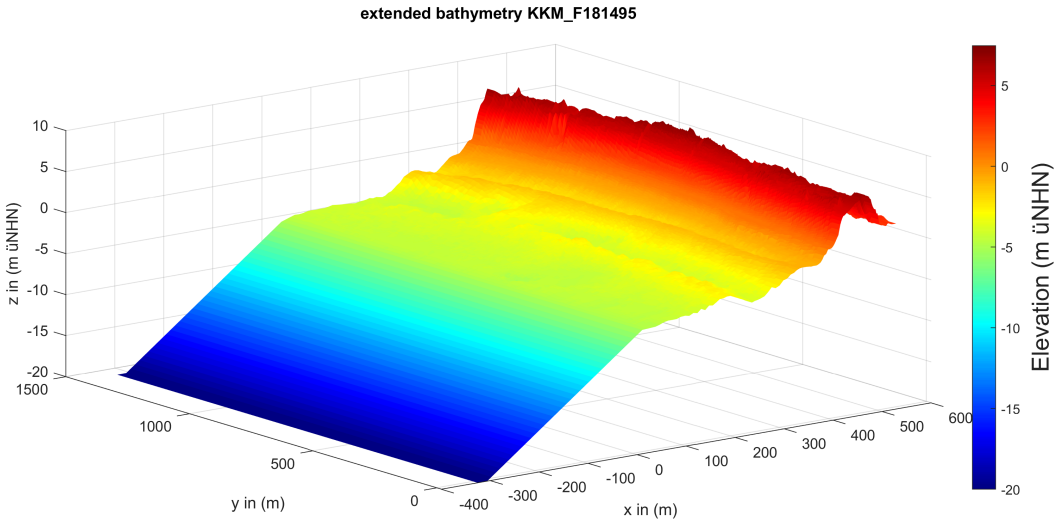

Figure 4.9: Modified and expanded bathymetry in 3D

4.6 Hydrodynamic Input

After setting up the computational grid, the hydrodynamic forcing was prescribed through wave and water level boundary conditions. In this study, the hydrodynamic conditions were set through `waves.txt` and `tide.txt` files. The `waves.txt` file contains the following information:

`< Hm0 > < Tp > < mainang > < gammajsp > < s > < duration > < dtbc >`

where the meaning of each is given in Table 4.2.

Figure 4.10 shows the variation of H_{sig}, T_p, surge and wave angle over time. The hydrodynamic inputs depict a single storm-like event with growth, peak, and decay. After an initial calm period, conditions intensify from 20 h onward: significant wave height rises steadily

to a maximum just before 70 h, while peak period lengthens, indicating a maturing sea state.

Table 4.2: Information contained in a wave.txt file

`Hm0`	significant wave height [m]
`Tp`	peak period [s]
`mainang`	mean wave attack angle [°]
`gammajsp`	peak enhancement factor [-]
`s`	directional spreading coefficient [-]
`duration`	duration of spectrum interval [s]
`dtbc`	temporal resolution of the wave time series [s]

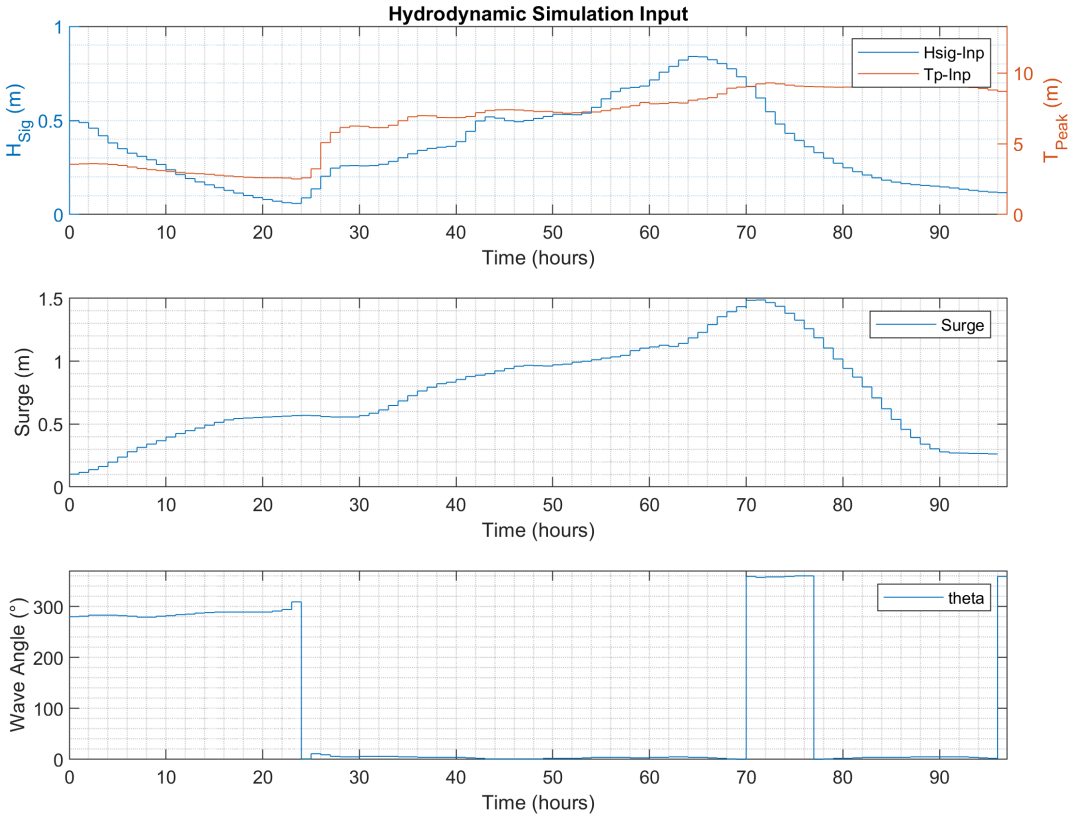

Figure 4.10: Hydrodynamic input used in the simulation

Concurrently, surge increases to roughly 1.4 – 1.5 m and then recedes. Under the nautical convention (clockwise from true north), the incident wave angle is almost constant at an angle of approximately 300°. For the time period between 24 h and 70 h, it is approximately 0°. There is quick change of angle to around 350 degrees for the time period 70-77 h and then it is 0° again. This information is also properly shown in Figure 4.11.

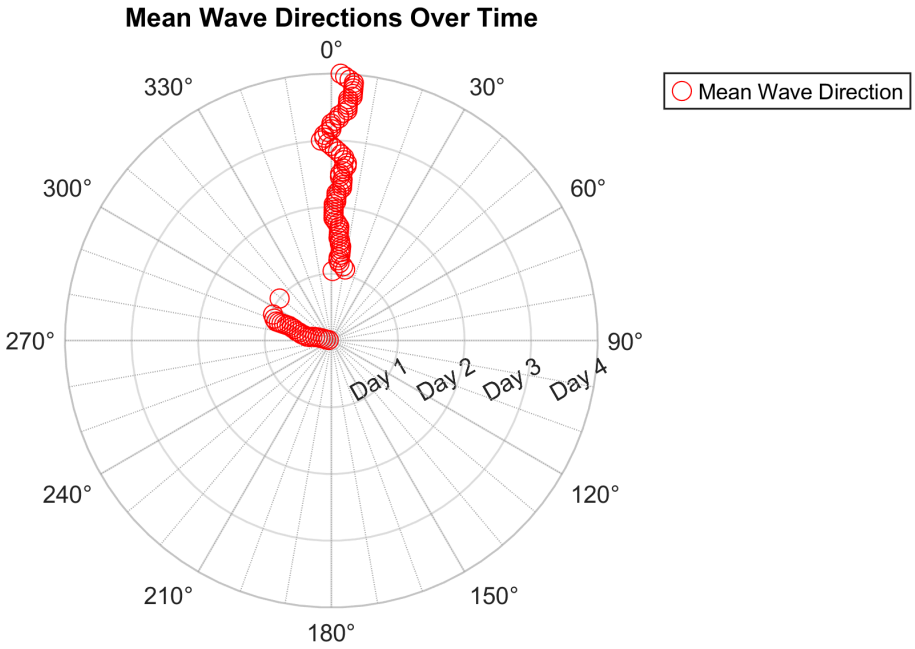

Figure 4.11: Mean wave directions over time

4.7 Specification of the Boundary Conditions

4.7.1 Specification of Offshore Wave Boundary Conditions

Usually, the offshore boundary is an artificial boundary, which has no physical meaning. On the offshore boundary, wave and flow conditions are imposed. In the computational domain, waves and currents will be generated which should pass through the offshore boundary to the deep sea with minimal reflection.

In XBeach, spectral wave boundaries can be provided as:

1. parametric JONSWAP spectra, either a single spectrum (`wbctype = jons`) or a time-series table (`wbctype = jons_table`)
2. nested SWAN spectra from two-dimensional frequency–direction files (`wbctype = swan`)
3. user-supplied spectra of arbitrary shape (`wbctype = vardens`).

In this study, time-varying parametric spectra were prescribed using `wbctype = jons_table`, whereby each record provided the JONSWAP parameters for the boundary at the corresponding time step.

With `wavemodel = surfbeat` selected, the lateral wave boundaries were prescribed as `lateralwave = neumann`, i.e., the longshore gradient was set to zero. As Neumann conditions in surfbeat can introduce shadow-zone artefacts mainly in wave-groupiness (rather than in significant height), a narrow buffer adjacent to the lateral edges was excluded from analysis. The alternative `lateralwave = wavecrest` was not adopted to avoid potential over-refraction and inflated longshore currents.

4.7.2 Specification of Flow Boundary Conditions

Flow boundary conditions are specified on all sides of the domain. In this study, the flow boundary conditions at both the offshore (front) and onshore (back) sides of the XBeach domain were set to `abs2d` (i.e., absorbing–generating, weakly reflective). This choice, which is also the model's default, permits obliquely incident and reflected waves, making it suitable for fully two-dimensional simulations, while providing stable absorption of outgoing long waves to minimize spurious reflections. Using `abs2d` on both boundaries ensures consistent wave handling across the domain and avoids the limitations of 1-D or wall (no-flux) conditions, which are less appropriate for our coastal application. For the left and right boundary, the default `left = neumann` is used. Along the lateral boundaries (left and right; perpendicular to the coastline), Neumann (no-gradient) conditions, i.e. `left = neumann` and `right = neumann` were applied, which enforce locally zero normal gradients in water level and velocity and are recommended in XBeach.

Figure 4.12 shows the flow boundary conditions in all the four boundaries. The green line at the middle represent the transect along which cross section study is conducted.

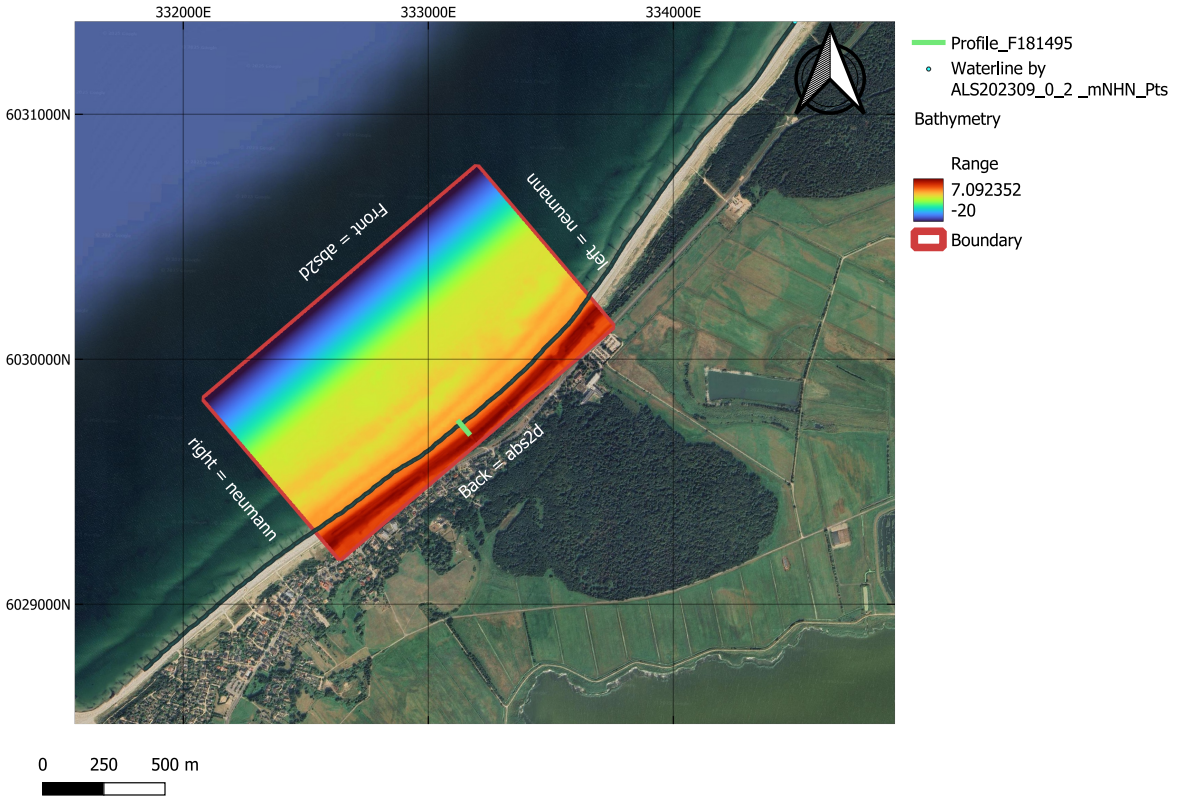

Figure 4.12: Study area with bathymetry and boundary conditions

After the construction of final grid, the bathymetry and grid information are exported as `bed.dep`, `x.grd` and `y.grd` respectively. Then using the function `xb_generate_settings()`

from Open Earth Tools (**OET**), `params.txt` file was created which now contains grid and bathymetry info, wave input, flow input, morphological input, etc. in the form of keyword/value pairs. It also generated new values of nx and ny, which now are irregularly spaced. In summary, the list of files that need to be present in a folder before running XBeach is presented in Table 4.3. The parameters `tintm` and `tintg` shown in Table 4.3 are the interval of time-averaged spatial output and interval for instantaneous spatial output respectively. A typical example of `params.txt` file is shown in Appendix D.

Table 4.3: Files needed for XBeach model setup

File	**Function**	**Additional Information**
XBeach.exe	XBeach executable	Use of XBeach 1.24.6057 Halloween version
Params.txt	File defining all model parameters	
Depth file	Model Bathymetry	Use of `bed.dep` file
Grid file	Model grid	Use of `x.grd` & `y.grd` file
Wave input files	wave conditions	use of `waves.txt`
Water level input	To apply varying tide and surge conditons	use of `tide.txt`

Table 4.4: Modeling - Input Data

Parameter		**Used values**
Grid information	nx	164
	ny	286
	dx	d x_{min} = 2 m ,d x_{max} = 10 m
	dy	d y_{min} = 2 m ,d y_{max} = 10 m
	offshore waterdepth	−20
	offshore slope	0.05
wave	thetamin/thetamax	220 ° / 20 °
	wavemodel / wbctype	surfbeat / jonstable
Sediment	D50 / D90	0.26 mm / 0.45 mm
	morfac	10
Other	cyclic(boundaries)	1
	tintg / tintm	600 s / 3600 s
	CFL	0.7

5 Results and Discussion

First of all **LHS** was used to generate a number of random samples where *facua, gamma* and *gamma2* were varied in the ranges provided by the XBeach manual. For porosity, it was varied between 0.35 and 0.45 with the default value of 0.4. Table 5.1 and Table 5.2 show the set of ranges of the selected parameters offered by XBeach along with the obtained results after simulations.

Table 5.1: Selected Parameters for LHS-based Simulation

Parameter	Default-value	Range offered by XBeach
facua	0.175	0.0 - 1.0
gamma	0.46	0.4 - 0.9
gamma2	0.34	0.0 - 0.5
wetslp	0.15	0.1 - 1.0

Table 5.2: Selected LHS-based Parameter Combinations used in XBeach Simulations

Run	facua	por	gamma	gamma2	BSS	RMSE	cumVdt (m^3/m)	Erosion (m^3/m)	Accretion (m^3/m)
001	0.175	0.4	0.46	0.34	0.755	0.196	−0.926	6.802	6.081
002	0.188	0.362	0.606	0.112	−0.233	0.44	−4.716	5.546	0.405
003	0.002	0.421	0.417	0.07	0.575	0.258	2.475	12.224	16.411
004	0.073	0.36	0.837	0.163	0.038	0.389	−2.414	12.851	10.005
005	0.109	0.361	0.427	0.435	0.443	0.296	0.012	5.357	6.061
006	0.285	0.303	0.772	0.299	0.237	0.346	1.27	3.376	5.27
007	0.132	0.36	0.432	0.336	0.611	0.247	−3.998	9.821	5.649
008	0.197	0.379	0.452	0.162	0.619	0.244	−0.441	6.114	5.941
009	0.226	0.333	0.586	0.358	0.53	0.272	7.048	2.566	11.23
010	0.233	0.351	0.836	0.417	0.608	0.248	5.744	2.836	10.202
011	0.126	0.434	0.695	0.201	−0.032	0.403	−6.161	15.754	9.184
012	0.255	0.442	0.871	0.303	0.354	0.319	8.165	1.135	11.11
013	0.062	0.417	0.659	0.465	−0.093	0.414	−2.776	14.001	10.771
014	0.156	0.428	0.488	0.097	0.198	0.355	−4.997	8.731	3.63
015	0.02	0.42	0.783	0.494	−1.441	0.619	−2.964	23.208	21.308
016	0.05	0.369	0.736	0.427	−0.325	0.456	−2.393	15.471	12.663

Table C.1 shows the complete set of 50 runs, including one run with the default values of the selected parameters.The highlighted first row of Table 5.1 shows the set of default parameter combinations. For each run, BSS, RMSE, cumulative change in volume (cumVdt), erosion and accretion were extracted using **NetCDF** files and a **MATLAB** script. Grid related information and hydrodynamic input are shown in Table 4.4 and described in Section 4.6

respectively. The run 015 with a parameter combination of *facua* = 0.02, *por* = 0.42, *gamma* = 0.783 and *gamma2* = 0.494 (Table 5.2) produced a clear storm-dominated response. The small value of *facua* represents strong storm conditions, leading to pronounced dune erosion with an erosional volume of 23.21 m³/m, while the displaced sediment was deposited offshore (Figure 5.1). The cross sectional profile shown is in the middle of the grid domain (i.e., for all values of m and $n = 144$). This configuration yielded a comparatively higher BSS score (0.61), indicating improved agreement with the measured profile, although at the cost of substantially increased dune erosion.

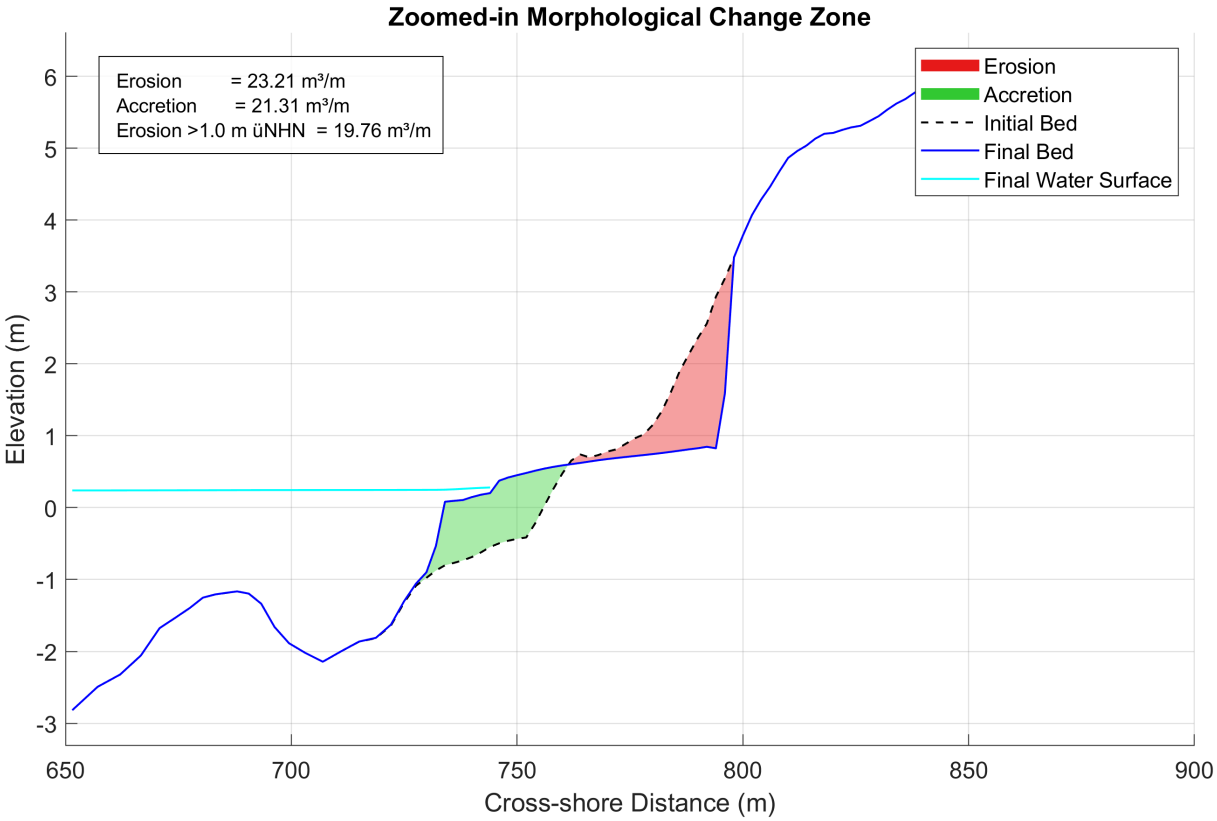

Figure 5.1: Cross-sectional profile for facua = 0.02, gamma= 0.783, gamma2 = 0.494 and por = 0.42 (n = 144)

At the end of the simulation for run 015, the cumulative erosion and sedimentation pattern across the model grid is presented in Figure 5.2. The plot confirms that the dune toe in the nearshore zone experienced severe erosion, while the adjacent offshore area acted as a depositional sink, accumulating the displaced material. For run 006, the two-dimensional erosion–sedimentation distribution (Figure 5.4) revealed a similar trend as observed in the cross-shore profile (Figure 5.3), with limited dune erosion and enhanced lower-foreshore accretion.

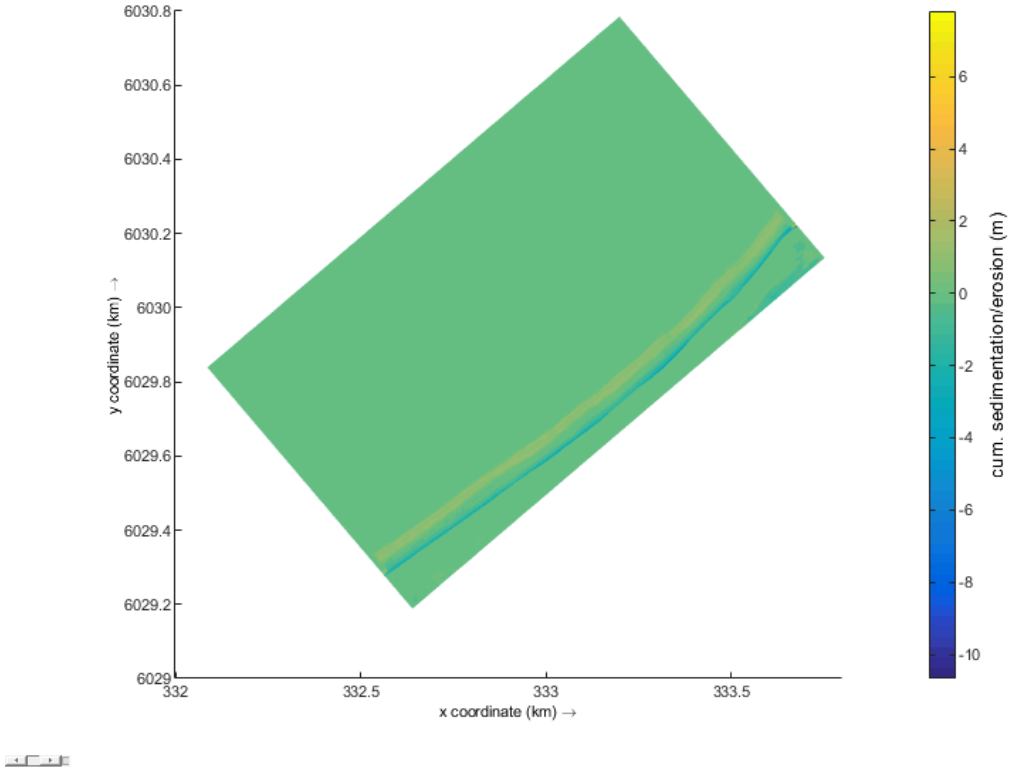

Figure 5.2: Cumulative erosion / sedimentation at the end of simulation for facua = 0.02, gamma= 0.783, gamma2 = 0.494 and por= 0.42

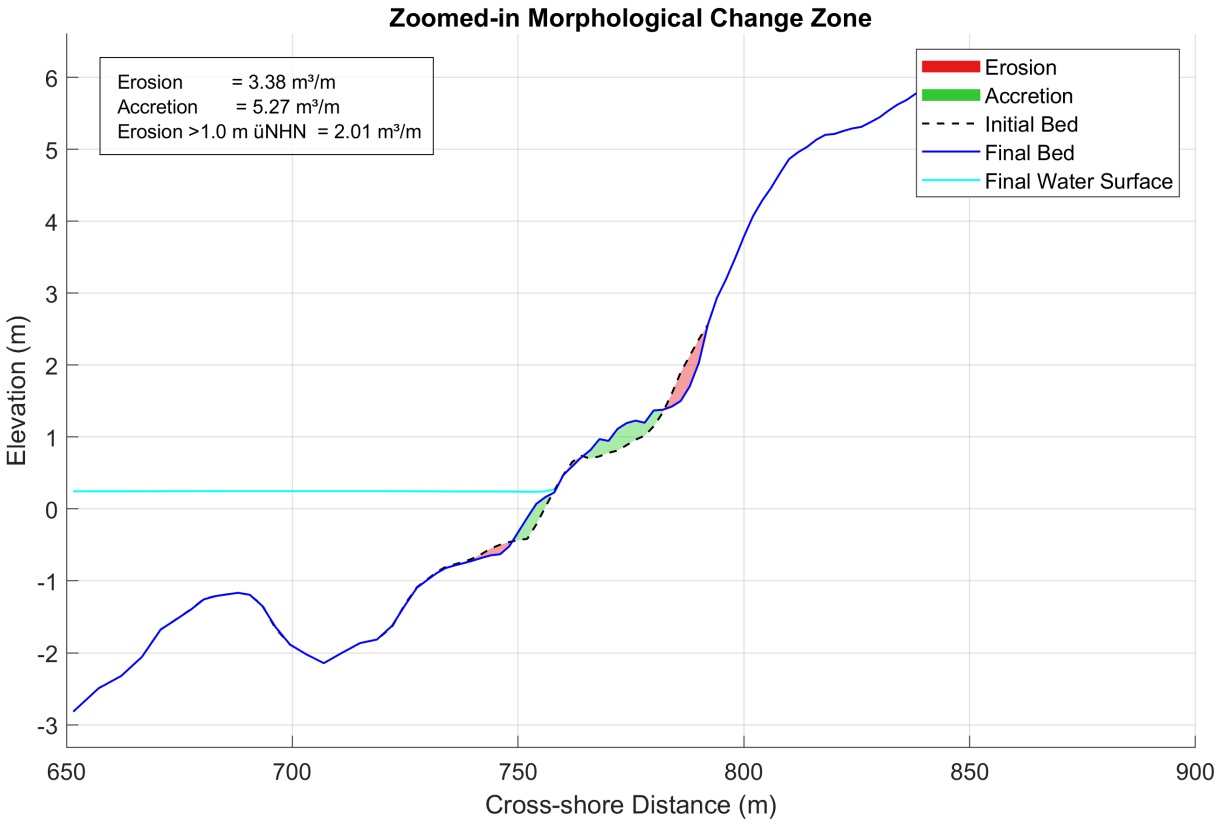

Figure 5.3: Cross-sectional profile for facua = 0.2854, gamma = 0.7716, gamma2 = 0.2985 and por = 0.3025

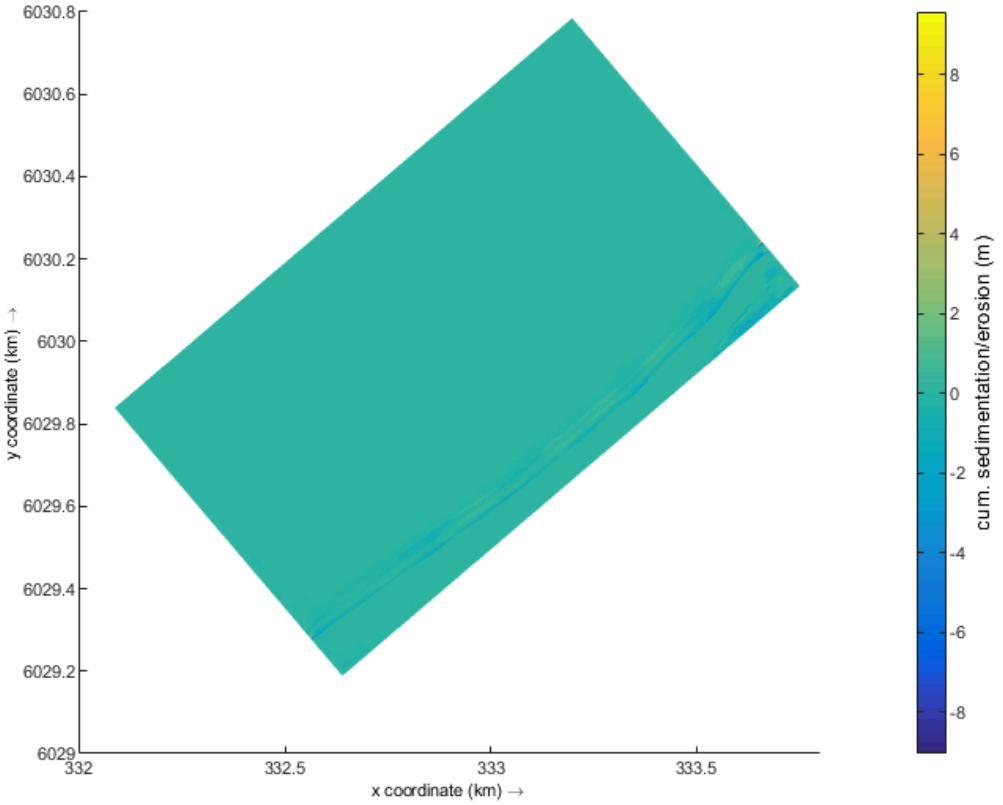

Figure 5.4: Cumulative erosion / sedimentation at the end of simulation for facua = 0.2854, por = 0.3025, gamma = 0.7716 and gamma2 = 0.2985

The run 006 with a parameter combination of *facua* = 0.2854, *por* = 0.3025, *gamma* = 0.7716 and *gamma2* = 0.2985 (Table 5.2) reflected more onshore-directed transport conditions. The higher value of facua enhanced accretion in the lower foreshore (5.27 m³/m) while limiting dune erosion to only 3.38 m³/m (Figure 5.3). However, this configuration resulted in a lower BSS score (0.23), indicating a weaker agreement with the measured profile despite reduced erosion volumes.

5.1 Parameter Sensitivity Analysis based on Statistics

Despite the regression and correlation analysis, no robust conclusions could be drawn from the obtained set of runs based on LHS. The number of completed runs was too low to identify statistically reliable parameter–metric relationships, with most p-values exceeding the conventional 0.05 significance level. For example, while *facua* showed moderate correlations with BSS ($r \approx 0.47$) and RMSE ($r \approx -0.45$) as shown in Figure 5.5 and Figure 5.6, these were only marginally significant ($p \approx 0.06$–0.08). Each subplot shows scatter points, least-squares regression line, and Pearson correlation coefficient (r) with associated p-value.

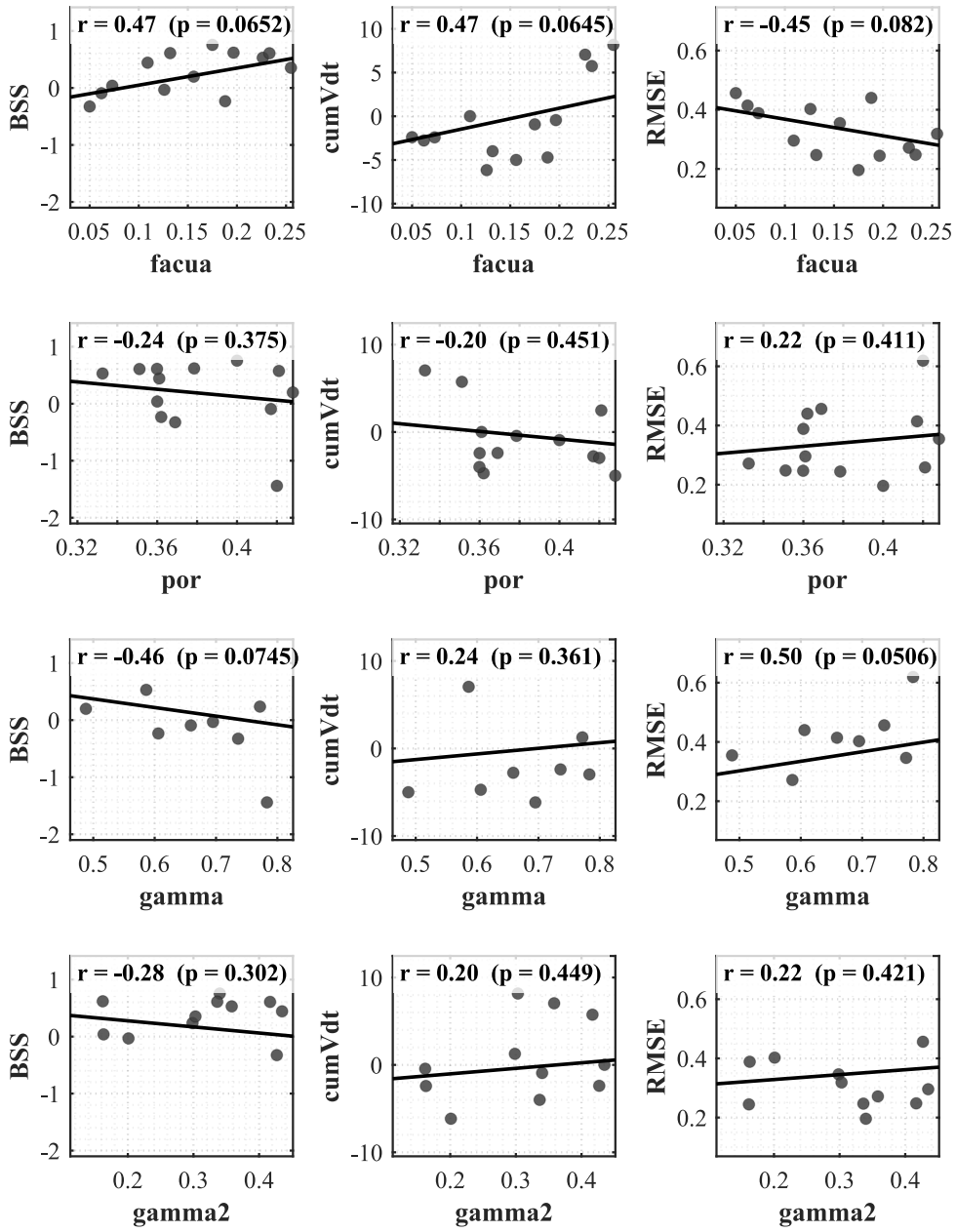

Figure 5.5: Linear regressions between XBeach input parameters and model performance metrics

Similarly, *gamma* exhibited trends opposite to *facua*, but again with p-values near the threshold. Porosity (*por*) and *gamma2* displayed weak, non-significant associations with all metrics. Taken together, the results indicate that the dataset is insufficient for drawing meaningful inferences on parameter sensitivity or for guiding calibration strategies.

The primary limitation stems from the computational burden of XBeach simulations with the netCDF implementation. Each run required more than 18 hours of computation time, and in several cases simulations crashed before completion. This made it infeasible to generate a sufficiently large ensemble of runs for reliable statistical evaluation. As a consequence, the analysis had to be terminated at this stage and a shift toward the

more traditional OAT method was necessary. While the preliminary trends hint at possible parameter influences, the low sample size and instability of the simulation setup prevent these results from being considered conclusive.

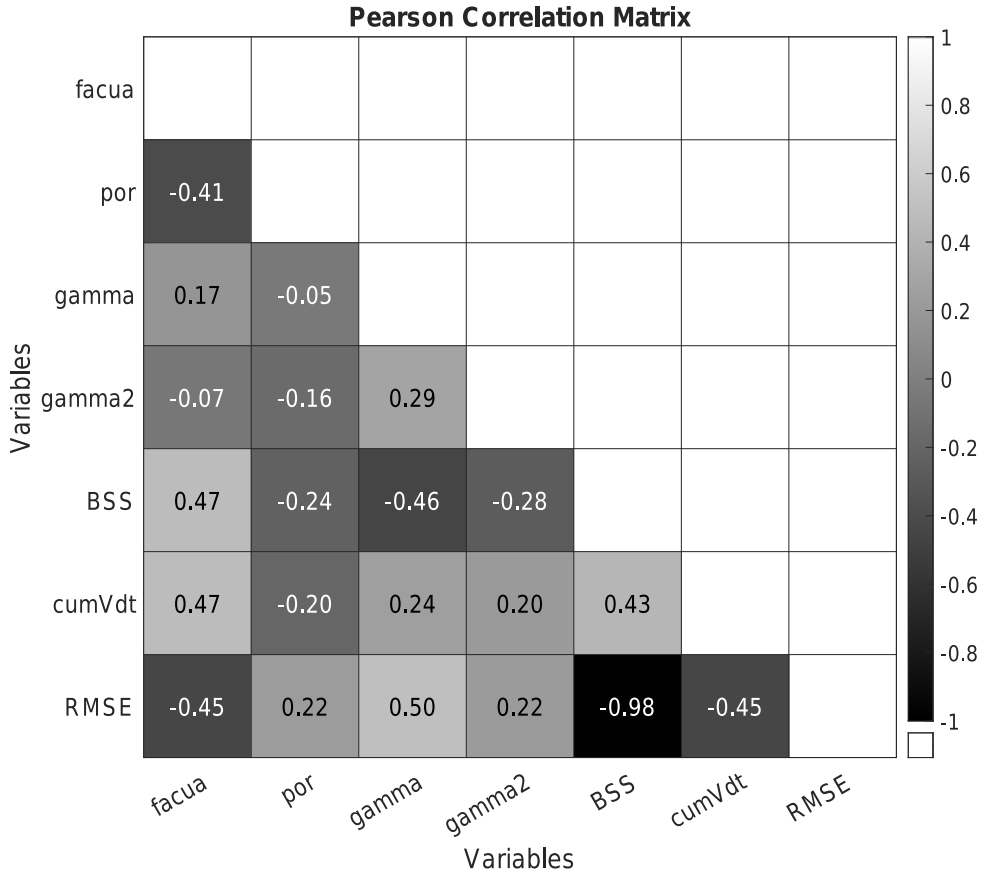

Figure 5.6: Pearson correlation matrix between XBeach input parameters and model performance metrics

The parameter porosity (*por*) was excluded from further analysis within the GLUE framework due to its negligible influence on model performance. Correlation analysis revealed weak and statistically non-significant relationships with all three evaluation metrics ($|r| < 0.24$, $p > 0.35$). These results indicate that porosity does not meaningfully affect model skill, error reduction or erosion volume estimates within the tested range. So, it was fixed at a default value (0.4) to simplify calibration and focus computational resources on more sensitive parameters such as *facua, theta* and *dtheta*.

5.2 Application of GLUE Methodology for Sensitivity Analysis

Table 4.1 presents the model performance as evaluated following the approach of Rijn et al. (2003). However, in this study, based on only 16 simulation runs, the obtained BSS values were comparatively low, with several runs even producing negative values (as seen in Table 5.2). To apply the GLUE methodology, only behavioural runs with positive BSS were considered and likelihood weights were assigned based on the BSS values. Subsequently,

the K-SD value was calculated as described in Section 4.1. The calculation of likelihood BSS and cumulative likelihood BSS is shown in Table 5.3.

Table 5.3: Selected LHS-based Parameter Combinations for Sensitivity Analysis (BSS > 0)

Run	facua	gamma	gamma2	BSS	Likelihood BSS	Cumulative Likelihood BSS
001	0.175	0.46	0.34	0.755	0.152	0.152
008	0.1965	0.4515	0.1618	0.619	0.125	0.277
007	0.132	0.4318	0.3362	0.611	0.123	0.4
010	0.2331	0.8362	0.4167	0.608	0.122	0.522
003	0.002	0.417	0.07	0.575	0.116	0.638
009	0.2263	0.5863	0.3583	0.53	0.107	0.744
005	0.109	0.427	0.435	0.443	0.089	0.834
012	0.255	0.871	0.303	0.354	0.071	0.905
006	0.2854	0.7716	0.2985	0.237	0.048	0.952
014	0.156	0.488	0.097	0.198	0.04	0.992
004	0.073	0.837	0.163	0.038	0.008	1

GLUE-based Parameter Sensitivity

Based on the results of the selected behavioural runs, K-SD values indicated differing levels of parameter sensitivity. As observed in the Figure 5.7, the parameter *gamma* showed the highest sensitivity (K-SD = 0.389), followed by *facua* (K-SD = 0.195) and *gamma2* (K-SD = 0.175). A higher K-SD value reflects a greater sensitivity, suggesting that gamma exerts the strongest influence on model performance in this limited ensemble. This aligns with findings from recent GLUE applications, which consistently identified *facua* and *gamma* as the most sensitive parameters in XBeach, while gamma2 tended to exhibit weaker but non-negligible effects (Bae et al., 2022; Gai et al., 2025).

However, the relatively low K-SD values across all three parameters, particularly when compared to values reported in larger ensemble GLUE studies, imply that the sensitivity patterns in this study are constrained by the small number of runs. In other coastal GLUE studies, *facua* has typically emerged as the dominant parameter controlling erosion response, with *gamma* exerting secondary but significant effects on wave breaking and energy dissipation (Bae et al., 2022; Simmons, 2018).

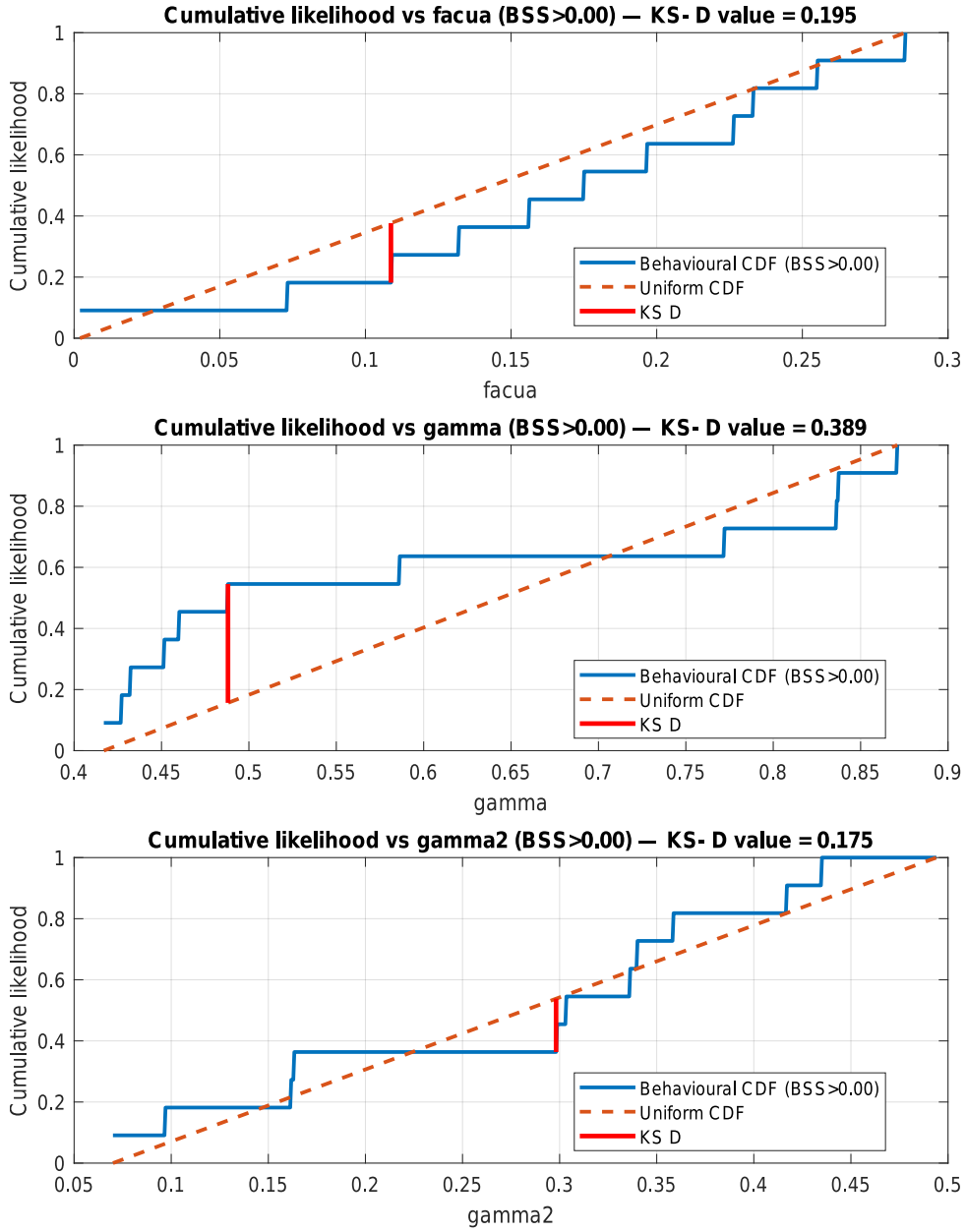

Figure 5.7: K-SD statistic based on GLUE methodology

5.3 Application of OAT Method

Following the application of the LHS-based GLUE method, key parameters such as *facua*, *gamma* and *gamma2* were varied individually while keeping the others constant. Same hydrodynamic input conditions were used as described in Section 4.6. But grid related information were changed to reduce the simulation time (Table 5.4). The morphological acceleration factor was also increased to 15 (`morfac = 15`). With changed grid related information and new value of *morfac*, the simulation time was reduced to average of 3.5 hrs from average of 18 hours. An overview of the simulation runs is provided in Table E.1 which shows BSS, erosion and accretion information.

Table 5.4: Modeling - Input Data for OAT method

Parameter		Used values
Grid information	nx	129
	ny	144
	dx	d x_{min} = 2 m ,d x_{max} = 20 m
	dy	d y_{min} = 2 m ,d y_{max} = 20 m
	offshore waterdepth	−20
	offshore slope	0.05
wave	thetamin/thetamax	220 ° / 20 °
	wavemodel / wbctype	surfbeat / jonstable
Sediment	D50 / D90	0.26 mm / 0.45 mm
	morfac	15
Other	cyclic(boundaries)	1
	tintg / tintm	600 s / 3600 s
	CFL	0.7

5.3.1 Variation of facua

The parameter *facua* was systematically varied around its default value of 0.175 while keeping other parameters constant to investigate its sensitivity to dune erosion processes. Two perturbation groups were introduced: (i) incremental increases of approximately +3 % to +7 %, resulting in values between 0.1802 and 0.1872, and (ii) reductions of −1 % to −10 %, yielding values between 0.1732 and 0.1575. These values of *facua* are summarized in Table E.1 together with other output metrics.

In Figure 5.8, the sensitivity of the model outputs to variations in the parameter *facua* is presented. In the upper panel, a decreasing trend of the BSS score with increasing *facua* is shown, with the highest statistical skill (BSS ≈ 0.61) obtained at the lowest tested values around 0.16–0.17. In the middle panel, the relationship between *facua* and the cumulative volume change (cumVdt) is displayed, where lower *facua* values resulted in more negative volumes, indicating stronger net erosion, whereas higher values reduced the erosional magnitude. In the bottom panel, the effect on dune erosion above 1 m üNHN is illustrated, showing a consistent decrease with increasing *facua*. This demonstrates that smaller values of *facua* intensified dune scarping, while larger values suppressed erosion. The intensified erosion near the dune toe for the lower value of *facua* (0.1575) can be compared with the cross sectional profile for another run with higher value of *facua* (0.1872) and the clear differences were noticed.

The erosion and sedimentation is taking place at certain places only, i.e. near surf zone and swash zone at a distance of ≈ 740-800m from offshore as shown in Figure 5.9 and

Figure 5.12. Figure 5.12 shows the final net sedimentation or erosion observed for the lowest value of *facua* adopted at time step 402 where $H_{\max}$ is reached with value of 1.66 m. The direction of sediment transportation can be confirmed by the observation of GLM velocities as observed in Figure 5.13. The arrows also indicate the magnitude of velocites. As observed in the figure, the observed magnitude of GLM velocities also match the area where there is erosion and sedimentation. The arrows are mixed with each other near the centre of the grid, because model grid is size varying and there is finer grid resolution at the centre of the grid.

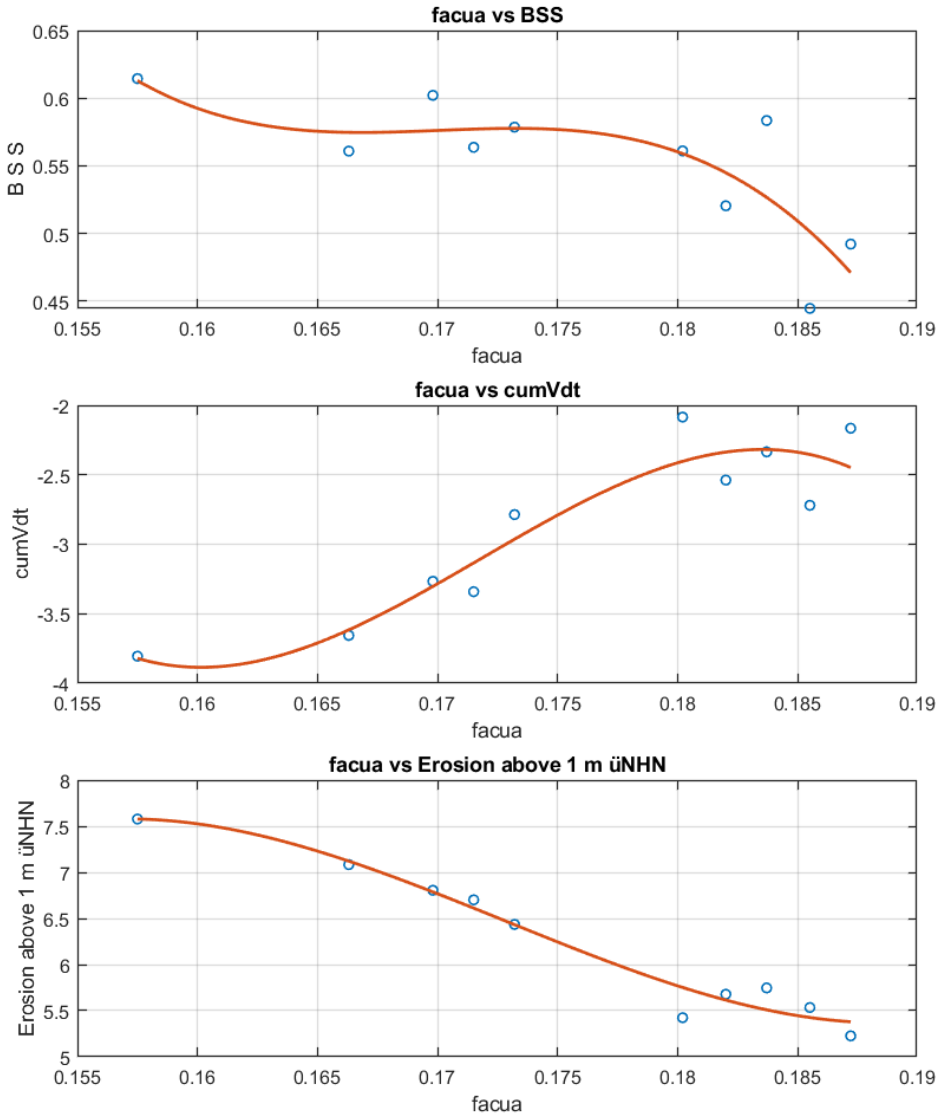

Figure 5.8: Relationship between facua and other output metrics

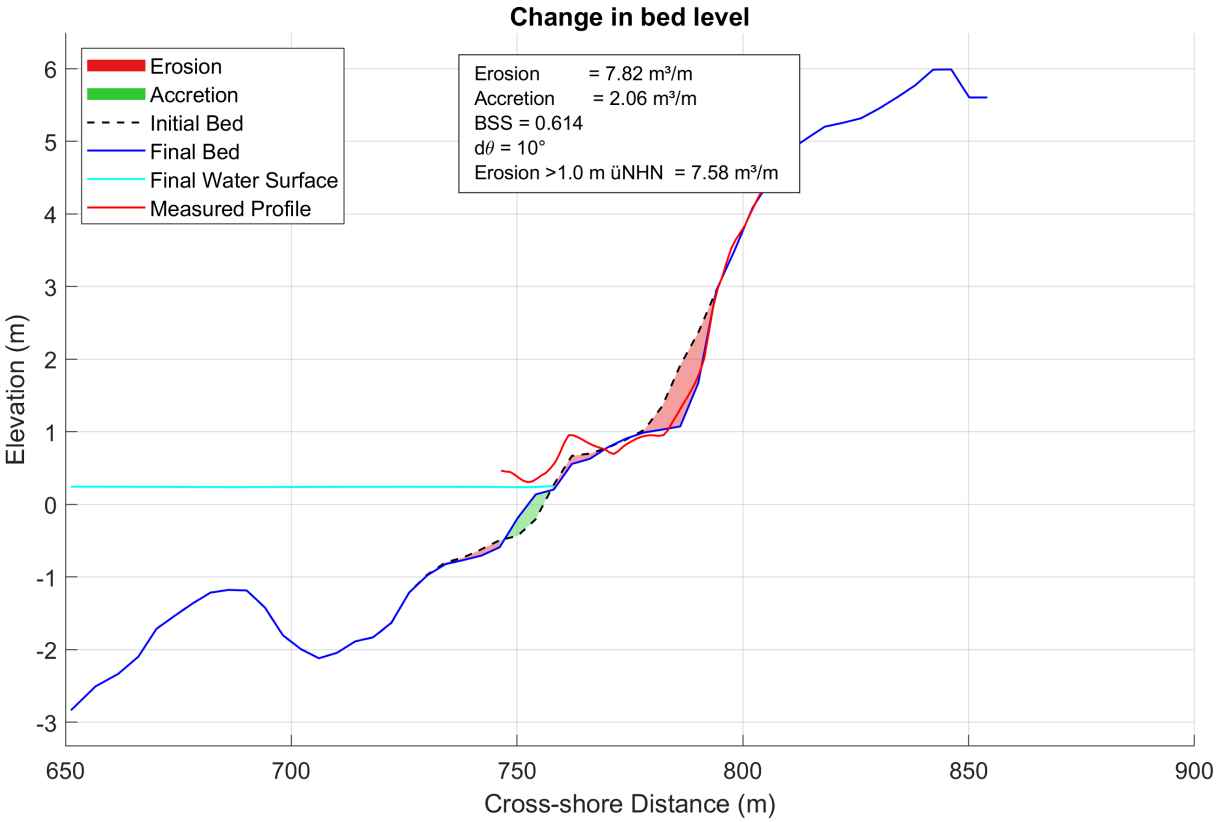

Figure 5.9: Observation of change in bed level for facua value of 0.1575

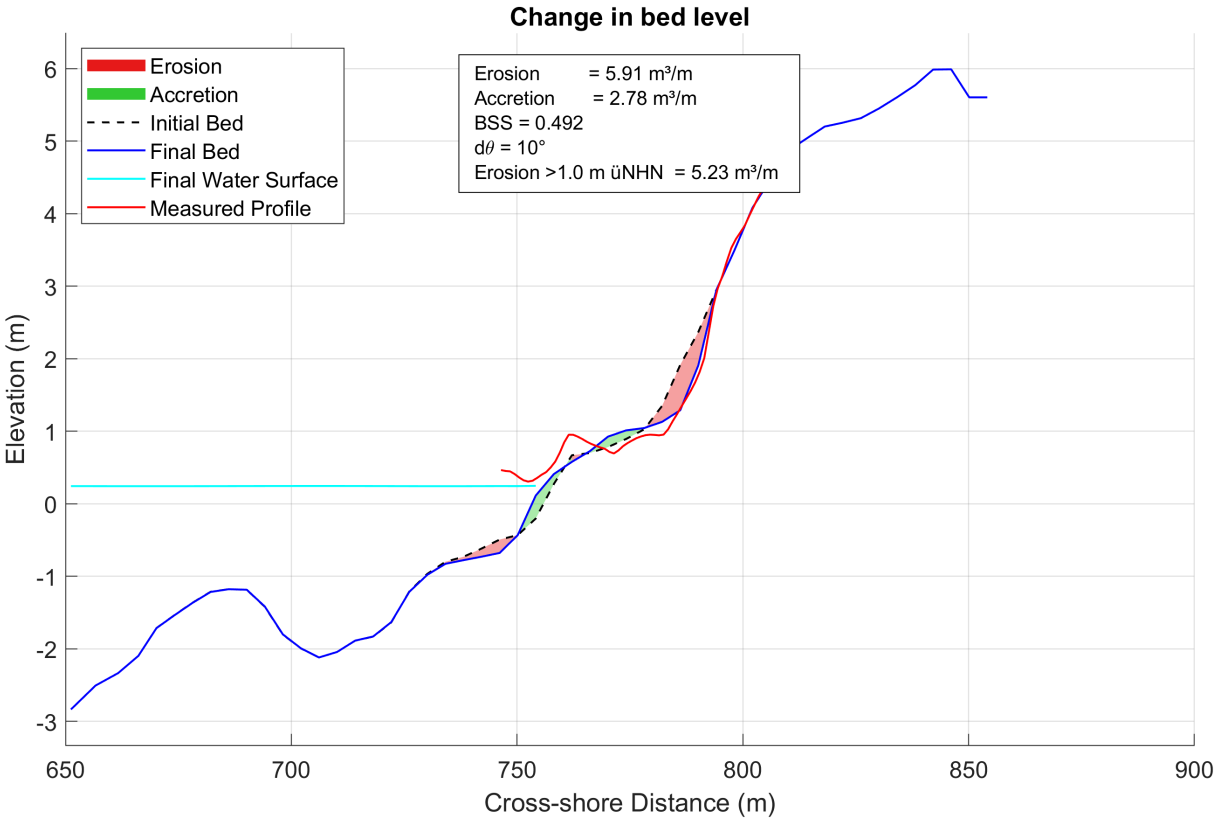

Figure 5.10: Observation of change in bed level for facua value of 0.1872

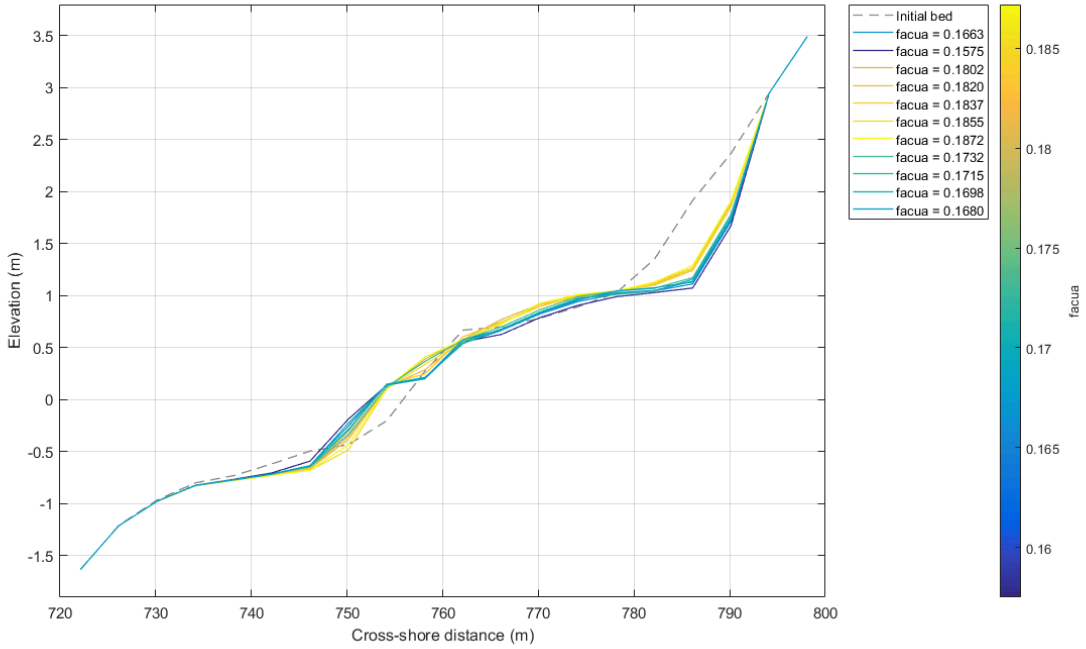

Figure 5.11: Bed level change for each value of facua

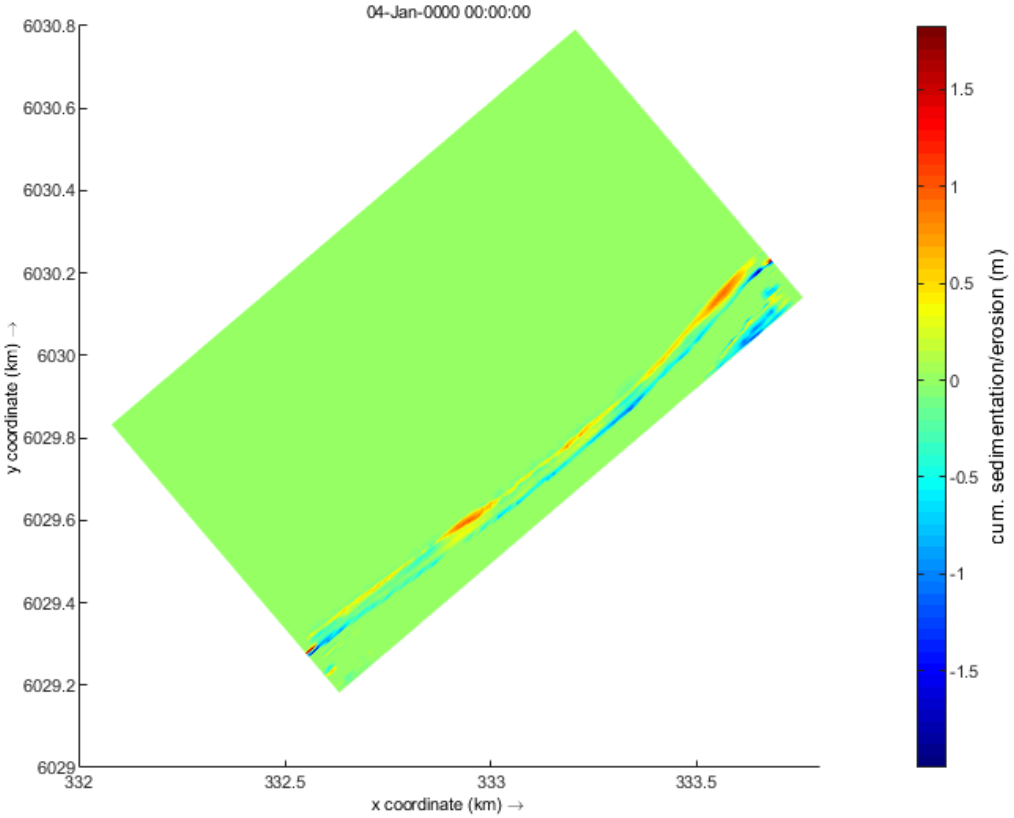

Figure 5.12: Change in bed level in 2D for facua value of 0.1575

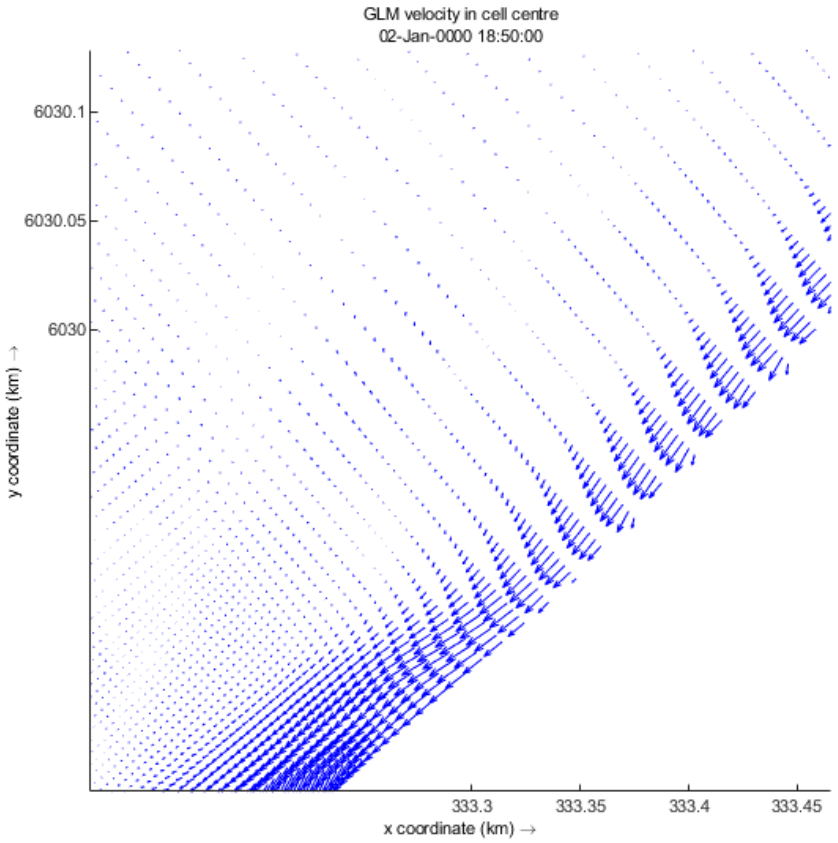

Figure 5.13: GLM velocity at cell center at time step 402 for facua value of 0.1575

5.3.2 Variation of gamma

The breaking parameter *gamma* was varied around its default value of 0.46 to capture potential shifts in wave breaking intensity. Two perturbation ranges were tested: reductions of −1 % to −4 % (*gamma* = 0.455–0.442) and increases of +1 % to +5 % (*gamma* = 0.465–0.483).

The performance metrics in Figure 5.14 showed that model skill and erosion response are moderately sensitive to *gamma*. The first plot shows that the BSS improves with increasing *gamma* up to about 0.47, after which it declines slightly, suggesting an optimal range for reproducing the measured profiles. The second plot reveals that cumulative erosion volumes above 1 m NHN (cumVdt) follow a similar pattern, with lowest erosion at intermediate *gamma* values and enhanced erosion for both smaller and larger values. The third plot, representing erosion above 1 m üNHN shows that higher (*gamma* > 0.48) values lead to increased dune loss.

These trends can be explained by the role of *gamma* in the wave-breaking formulation, where the maximum wave height is defined as:

$$H_{\max} = \gamma h + \delta H_{\mathrm{rms}} \tag{5.1}$$

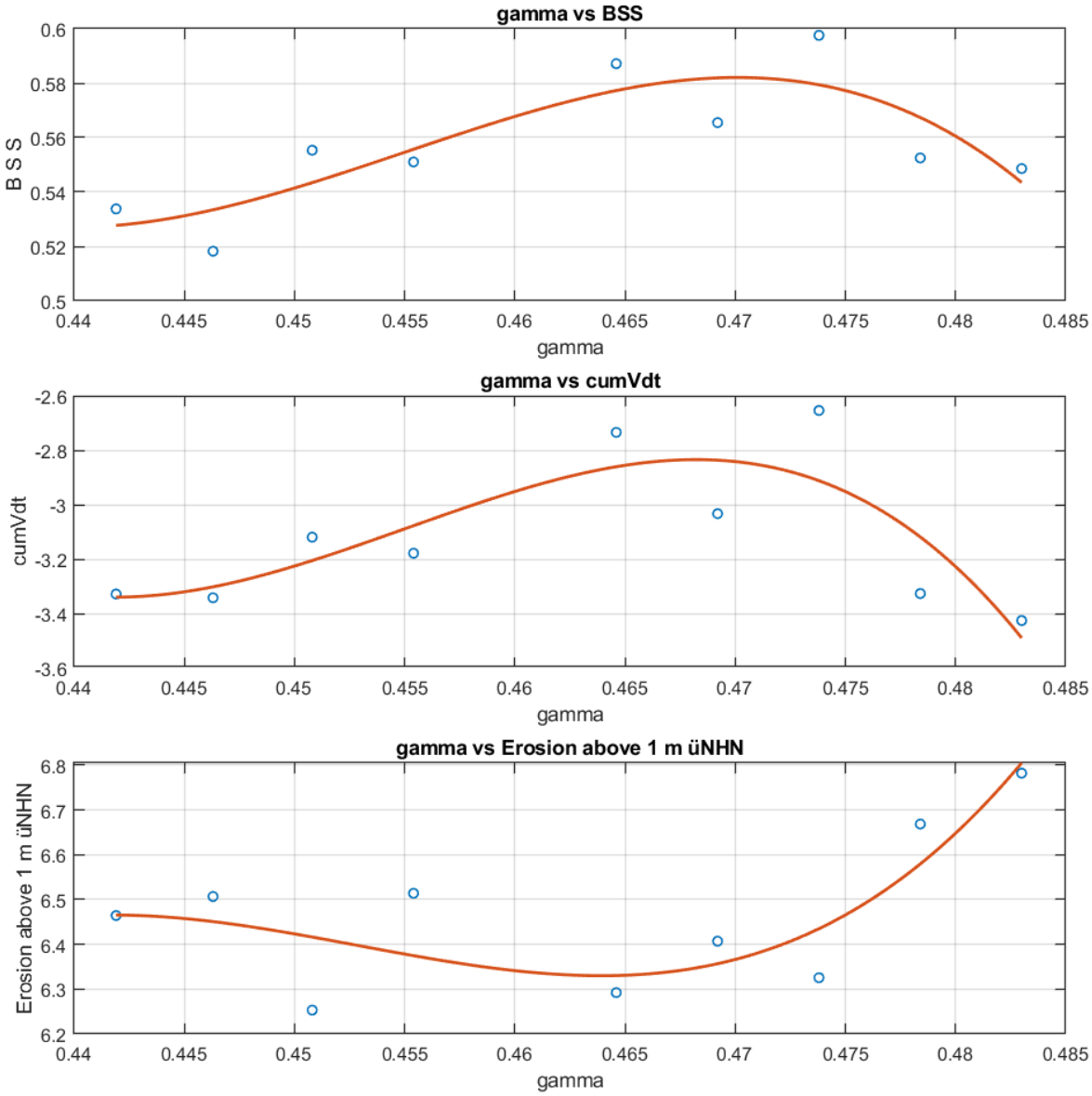

Figure 5.14: Relationship between BSS and variation of input Parameters

This threshold controls the fraction of breaking waves Q_b and thus the rate of energy dissipation. Smaller gamma reduces $H_{\max}$, increasing the fraction of breaking waves and intensifying turbulence and sediment mobilization at the dune toe. Larger γ raises $H_{\max}$, delaying breaking and allowing higher waves to propagate landward, which enhances scarping and crest lowering once breaking occurs. The reduced erosion at intermediate values reflects a balance where dissipation occurs seaward of the dune, limiting wave run-up and protecting the crest.

The cross-shore profiles (Figure 5.16) confirm that the morphological sensitivity to *gamma* is limited, with only subtle differences around ≈ 750–760 m and no significant change at the dune toe. This shows that while *gamma* exerts a measurable influence on dune

erosion and statistical skill, its effect remains secondary compared to transport-related parameters such as *facua*.

The above discussion can be further supported by examining the GLM velocity fields for different values of m. Figure 5.15 illustrates the direction of GLM velocity at $m = 1, 40, 65,$ and 105, corresponding to distinct cross-sections along the longshore direction. The brown and blue arrows represent GLM velocities for *gamma* = 0.483 and *gamma* = 0.4419, respectively, at time step $nt = 408$.

It can be observed that sediment transport is evident near the onshore region, particularly around the dune toe. Additionally, the GLM velocity vectors are generally aligned in the same direction at both offshore and onshore boundaries. However, for the higher *gamma* value, wave breaking occurs later compared to the lower *gamma* value. This is reflected in Figure 5.15, where the wave-induced velocity vectors at *gamma* = 0.483 continue to point in the original propagation direction as they move toward the coast, indicating delayed breaking.

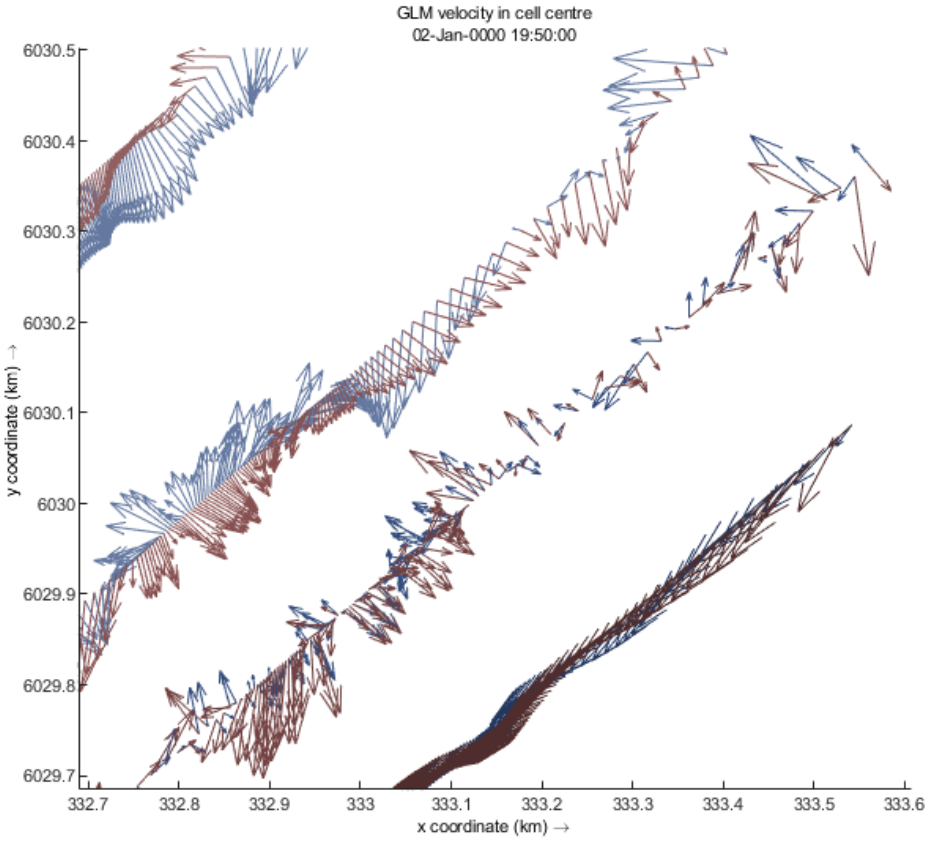

Figure 5.15: Observation of GLM velocity direction at nt = 408 and alond different alongshore grid for two values of gamma

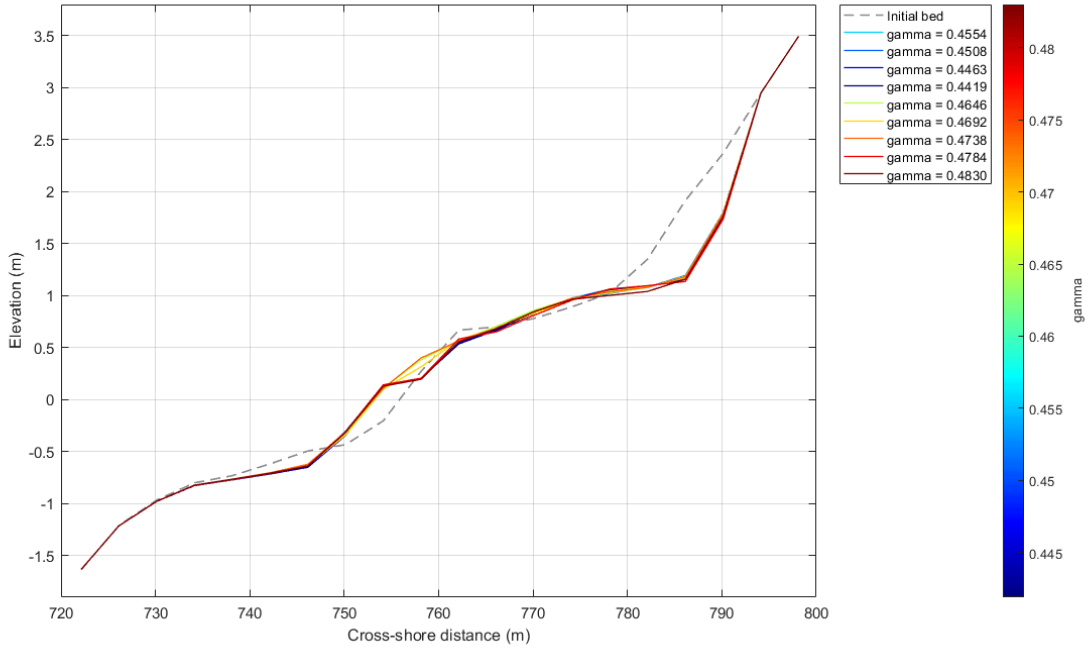

Figure 5.16: Cross sectional profile for according to different values of gamma

5.3.3 Variation of gamma2

The roller parameter *gamma2*, whose default value is 0.34, was explored across a wider sensitivity range compared to the other parameters. Because it was explored between 0.3366 to 0.3944, with some gaps in the middle, it was difficult to fit a cubic fit for this set of runs. So, it was not plotted. But the obtained values of BSS and erosion volumes are presented in Table E.1. Looking at this values, it hints that, a gamma2 value of 0.4 gives a good approximation to the actual profile.

5.3.4 Change of morfac Value to 20

The version of XBeach used in this study has a default *gamma* value of 0.46. Section 5.3.2 hinted that higher values of *gamma* improved model performance. Also, Roelvink et al. (2009) used default *gamma* value of 0.55 in their study. The *gamma2* values in the range 0.38 - 0.4 also produced better results as compared to the values lower than the default values as discussed in Section 5.3.3 (also shown in Table E.1). In addition to this, lower values of *facua* hinted for good model performance from the results shown in Section 5.3.1. On this basis, it was decided to accelerate the simulation with *morfac* value of 20 by varying *facua* in the range of 0.14 - 0.16 at an interval of 0.02 for *gamma2* values of 0.38, 0.39 and 0.40. Same hydrodynamic conditions and same grid information as shown in Table 5.4 were used except the value of morfac, which was set to 20. The overview of runs along with obtained results are presented in Table F.1.

The relationship between facua and BSS was evaluated separately for three fixed values of *gamma2* (0.38, 0.39, and 0.40) as shown in Figure 5.17. A cubic regression was fitted to each dataset to highlight potential nonlinear responses. For *gamma2* = 0.38, a weakly increasing trend of BSS with higher *facua* values was observed. The fit suggests that the statistical skill improves slightly as *facua* approaches 0.16, with an R^2 value of 0.40 indicating moderate explanatory power.For *gamma2* = 0.39, the relationship became flatter, with only minor improvements in BSS at higher *facua* values. The cubic regression explained less variance ($R^2 = 0.24$), reflecting a weaker influence of *facua* under this *gamma2* setting. For *gamma2* = 0.40, the relationship was more irregular, with no consistent monotonic trend. The cubic fit showed the lowest explanatory strength ($R^2 = 0.21$), suggesting that under this parameterization, BSS is largely insensitive to changes in *facua*. Overall, the analysis indicates that the sensitivity of BSS to variations in *facua* decreases as *gamma2* increases. At lower gamma_2 values, changes in *facua* exert a more noticeable, albeit still moderate, control on model performance, whereas at higher *gamma2* the effect becomes marginal.

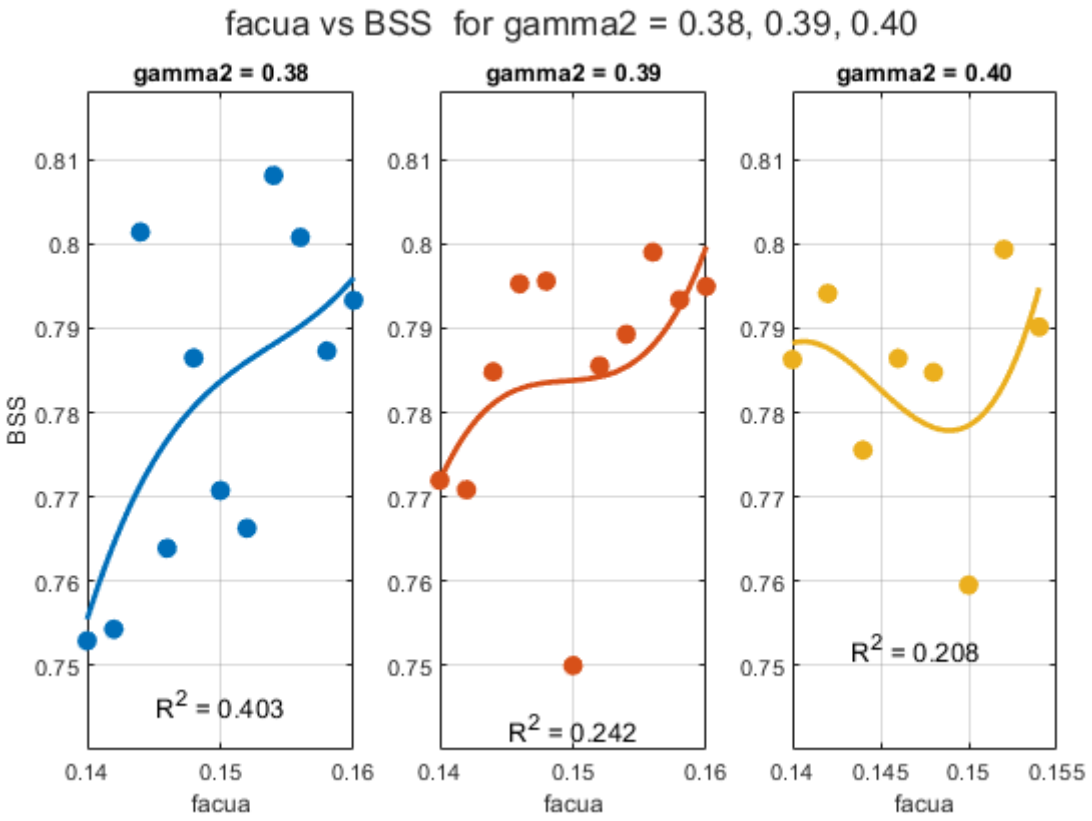

Figure 5.17: Observation of facua vs BSS for morfac value of 20 at higher value of gamma (0.6)

The relationship between *facua* and the cumulative volume change (cumVdt) was also evaluated for three different values of *gamma2* (0.38, 0.39, and 0.40). The scatter points and cubic fits are shown in Figure 5.18. For *gamma2* = 0.38, only a weak relationship was observed ($R^2 = 0.069$), indicating that variations in *facua* did not strongly explain the

variability in cumVdt. The trend suggests a slightly increasing cumVdt with larger *facua*, but the scatter indicates considerable variability.For *gamma2* = 0.39, a clearer non-linear relationship emerged ($R^2 = 0.349$). The fitted curve suggests that cumVdt decreases with *facua* up to about 0.150, followed by an increase at higher values. This indicates a potential threshold response of sediment volume change around intermediate *facua* values.For *gamma2* = 0.40, the strongest relationship was obtained ($R^2 = 0.753$), with a well-defined cubic trend. In this case, cumVdt initially decreases as *facua* increases, reaching a minimum near 0.150, and then rises again. This suggests that under higher *gamma2* conditions, the sensitivity of sediment volume change to *facua* becomes more pronounced, with the possibility of regime shifts between erosional and depositional dominance.Overall, these results indicate that the interaction between *facua* and *gamma2* strongly affects morphological response. At lower *gamma2*, the influence of *facua* on cumVdt is weak and scattered, whereas at higher *gamma2* values the response becomes systematic and more predictable.

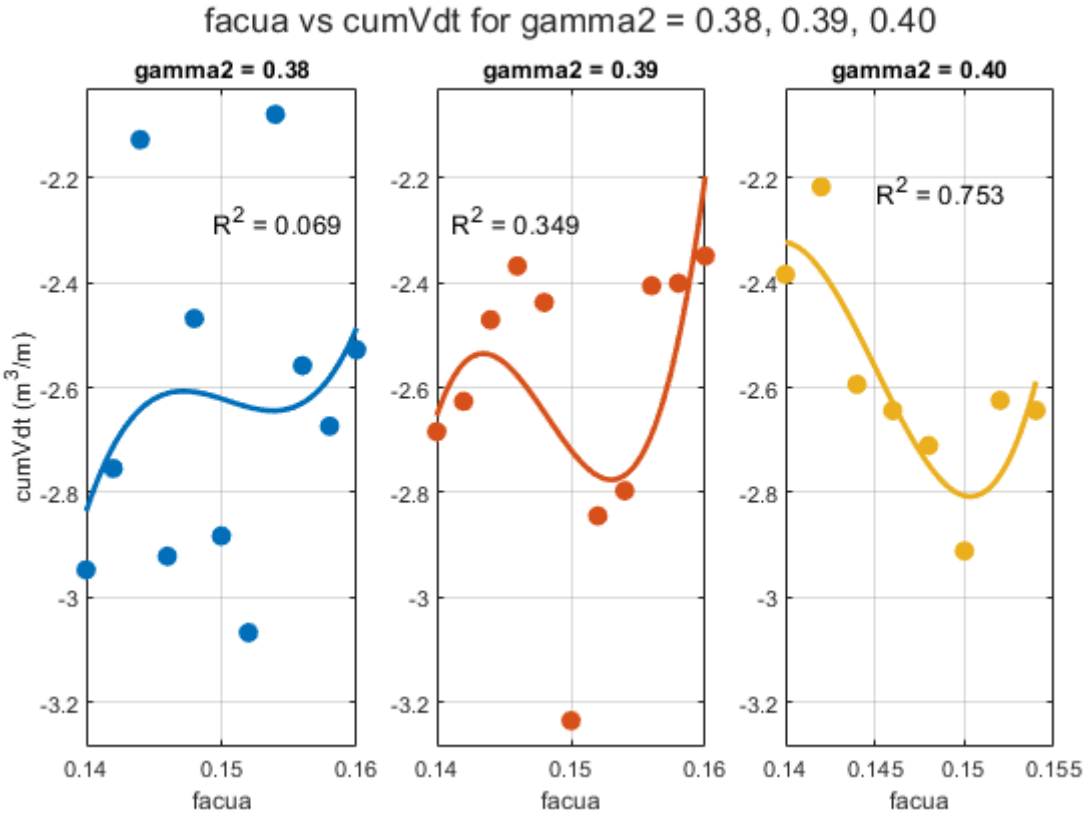

Figure 5.18: Observation of facua vs CumVdt for morfac value of 20 at higher value of gamma (0.6)

One cross sectional profile which obtained the highest value of BSS is shown in Figure 5.19. The simulated profile was found to reproduce the observed post-storm morphology with good agreement, as indicated by a high BSS value (0.8081) and a low RMSE (0.1676). The alignment of simulated and observed end-profiles suggests that the main patterns of

dune erosion were well captured. Localized erosion signals around the dune toe (750–800 m) correspond to areas of steep profile change, while the velocity components indicate enhanced flow in the same region, supporting the link between hydrodynamic forcing and sediment loss. Overall, the simulation demonstrated reliable skill in representing dune erosion processes, though localized erosion appeared more pronounced in the model than in the measurements.

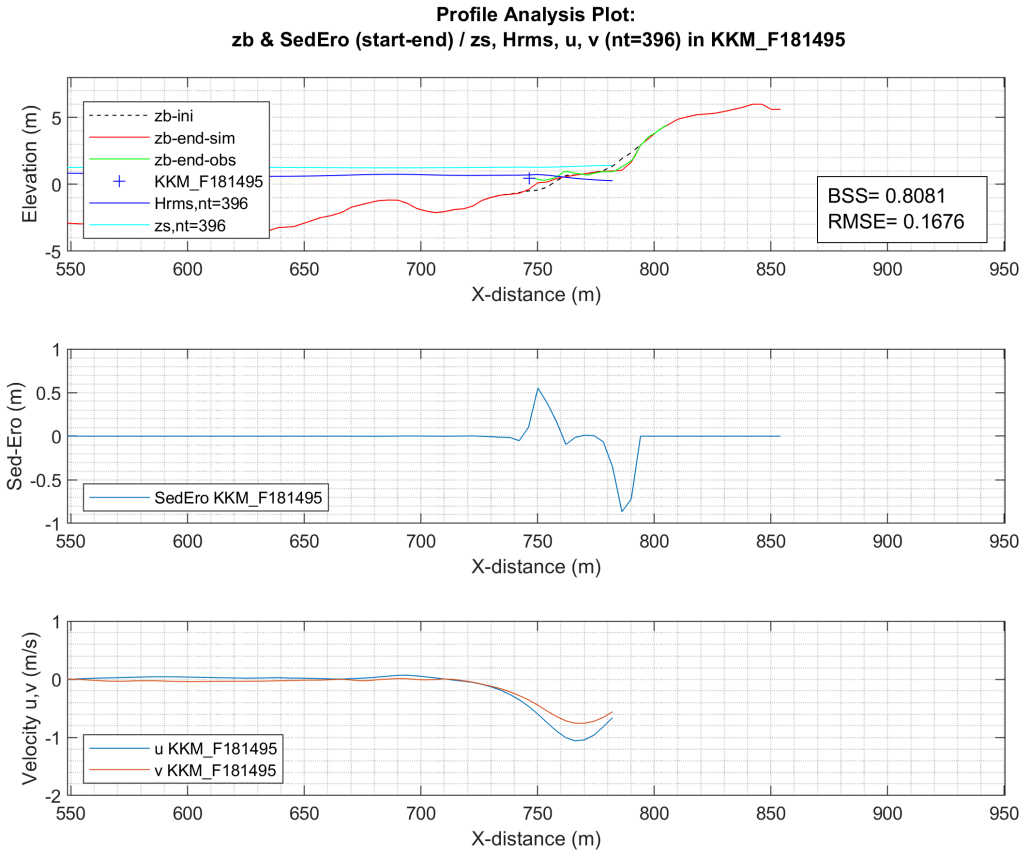

Figure 5.19: Profile Analysis Plot for morfac value of 20

5.3.5 Change in Dimension of Model Grid

The model grid was reduced in the longshore direction symmetrically keeping the cross shore length same. This resulted in $nx = 165$ and $ny = 81$ with size varying grid (Figure 5.20). This was also done to reduce the simulation time. But this time, *gamma* was varied by keeping other parameters constant because the higher values of *gamma*, as compared to default value (0.46) hinted for better model performance as presented in Section 5.3.2. Same hydrodynamic conditions and same grid information as shown in Table 5.4 were used and the morphological acceleration factor *morfac* was set to 15. The BSS values were significantly improved as shown in Figure 5.21.

Among the tested values, the run with *gamma* = 0.5 produced the highest model skill, with a BSS of 0.8562 and the lowest RMSE of 0.1526 (Figure 5.22). The simulated final bed profile closely matched the observed post-storm profile, particularly around the dune toe, where erosion and accretion patterns were captured with high fidelity.

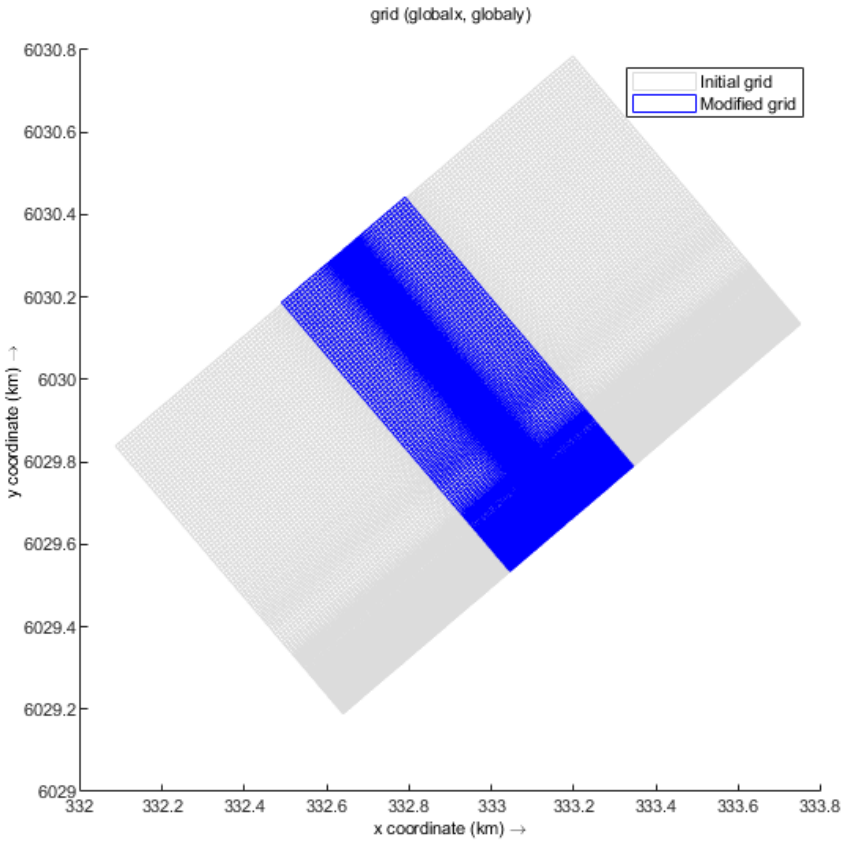

Figure 5.20: Change in longshore length of the model grid

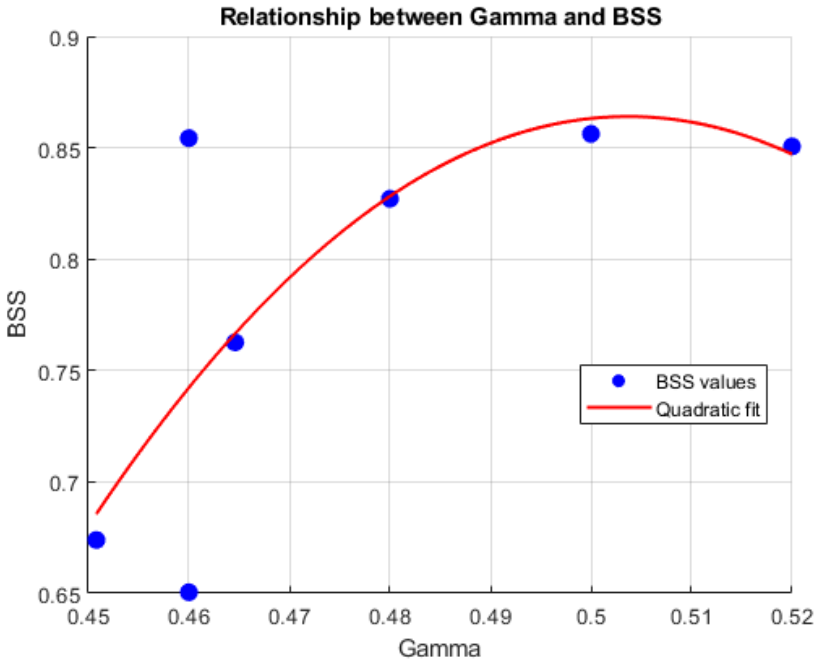

Figure 5.21: Relationship between gamma and BSS for reduced grid size

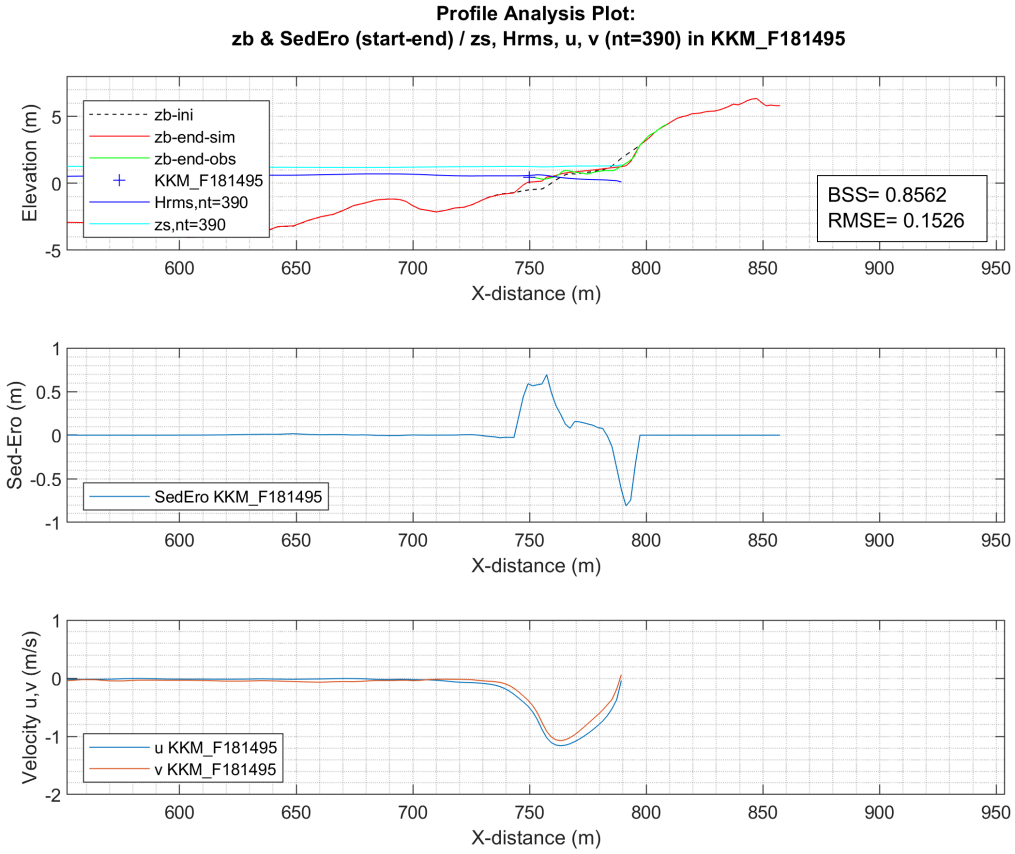

Figure 5.22: Profile analysis plot when longshore length was reduced

5.3.6 Variation of dtheta

While the parameters *facua*, *gamma* and *gamma2* directly control the representation of wave energy dissipation and hydrodynamic forcing in XBeach, they do not address the angular spreading of wave energy. Therefore, the parameter *dtheta*, which defines the directional resolution of the incoming wave spectrum, was also varied. A finer directional resolution allows for a more accurate representation of obliquely incident waves and longshore gradients in wave forcing, which can strongly affect sediment transport pathways and dune erosion patterns. In contrast, a coarser resolution reduces computational demand but may oversimplify directional energy distribution. Thus, testing the sensitivity of *dtheta* was necessary to assess the trade-off between model efficiency and the accuracy of morphodynamic responses.

In the used version of XBeach model in this study, the default value of the parameter *dtheta* is 10°, with an allowable range from 0.1° to 180°. For this part of the simulation study, *dtheta* was systematically varied at intervals of 2°, starting from 20° down to a finer resolution of 2°. In total, 10 simulations were performed. They hydrodynamic conditions were kept similiar as in the previous runs and the same bathymetry was used. The grid related information for these set of information was used as presented in Table 4.4. The obtained results are also presented in

Interpreting *dtheta* as the directional bin width, the results show a steady increase in **BSS** from 2° to 9°, a minor dip near 10°, and a clear rise to a maximum around 16° (**BSS** ≈ 0.80), followed by sharp deterioration at 20° (Figure 5.23). The concurrent volume response begins strongly positive at 2°, attains a distinct positive maximum near 12°, then returns to approximately neutral at 16° and becomes increasingly negative beyond 16°–18°, indicating net sediment deficit by 20°. Taken together, *dtheta* ≈ 14°–16° provides the most credible compromise, i.e. high BSS with a near-balanced sectional volume budget.

As the directional resolution parameter *dtheta* increased, erosion volumes greater than 1 m üNHN were observed to grow progressively. At the same time, accretion, which was substantial at small to intermediate dtheta and peaked around 10–12°, declined sharply beyond 14° and approached minimal values by 20° (Figure 5.24). This pattern can be attributed to a reduced retention of directional spreading and wave refraction at larger dtheta values. In XBeach, dtheta defines the directional bin width of the incoming wave spectrum. Smaller dtheta values provide finer angular resolution, allowing wave energy to be distributed across multiple propagation angles and improving the representation of oblique wave components, directional spreading and refraction. These processes promote a more balanced redistribution of sediment through both cross-shore and alongshore transport pathways. Conversely, larger dtheta values discretize the spectrum into fewer,

broader bins, which diminishes the capacity of the model to retain directional variability. As a result, the wave forcing becomes overly concentrated in fewer directions, amplifying cross-shore erosive processes while limiting compensating deposition. This reduction in angular detail explains the progressive net sediment deficit observed at large dtheta values, consistent with the cumulative volume change trends shown in Figure 5.23. In contrast, moderate dtheta values (approximately 14–16°) produced realistic dune erosion magnitudes while still allowing for appreciable local accretion, reinforcing this range as the most credible setting for the studied event and site.

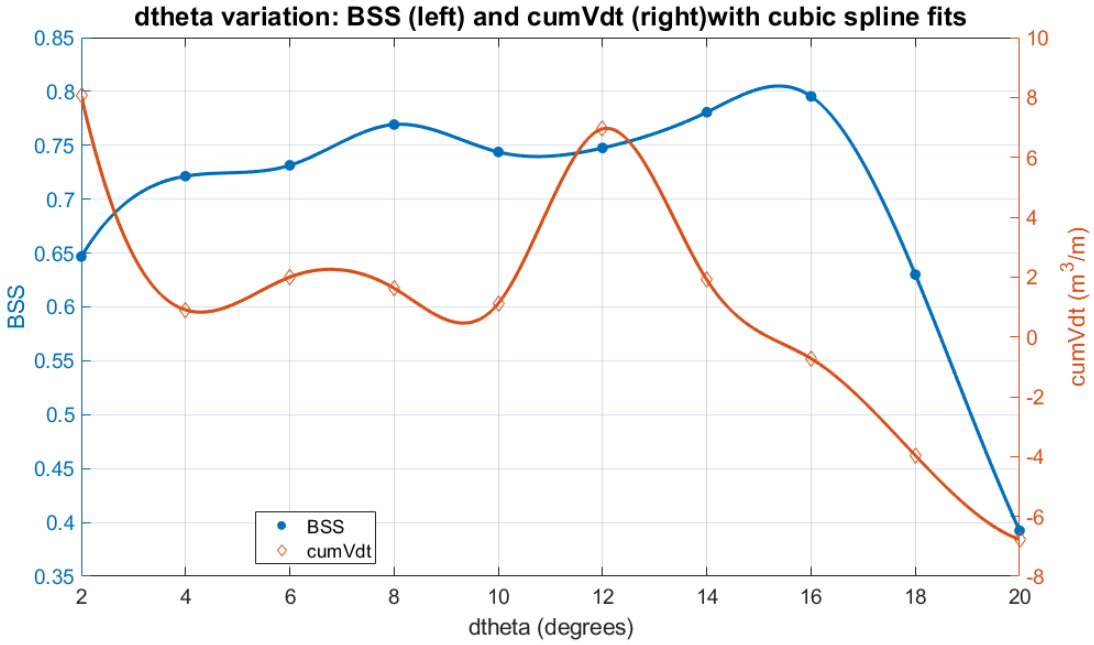

Figure 5.23: Observation of BSS and cumulative erosion volume with variation of dtheta

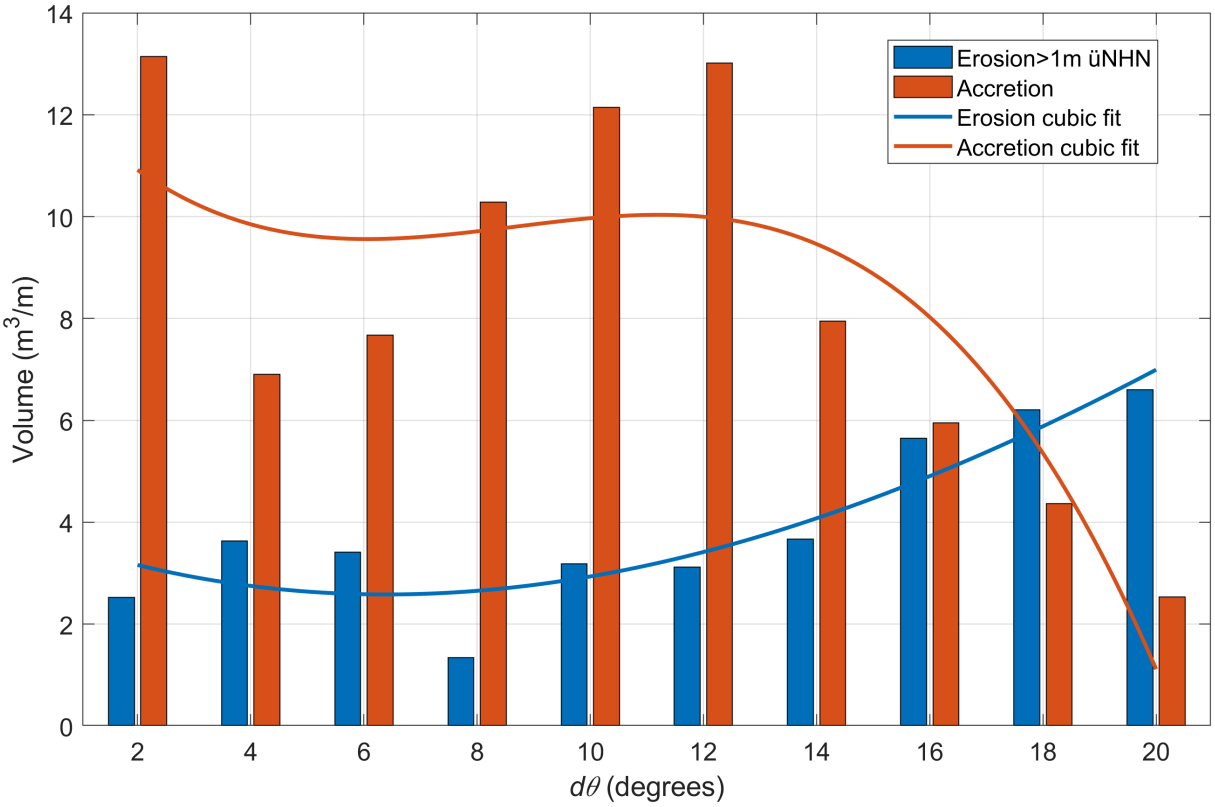

Figure 5.24: Variation of erosion and accretion with dtheta

Figure 5.25 compares modeled post-storm cross-shore profiles for a directional resolution *dtheta* from $20°$ to $2°$, against the initial bed (dashed) and the measured profile (black). In the region ≈ 760 – 780 m, the solutions are tightly clustered, indicating weak sensitivity of the wave–bed response to *dtheta* there. Sensitivity increases from $\approx 785\mathrm{m}$ toward the dune toe/upper beach ($\approx 790–800\mathrm{m}$), where the envelope of colored curves widens. Coarser directional discretization (e.g., *dtheta* = 20°) tends to predict stronger scouring at the toe and lower elevations, i.e., a more erosive response while finer resolution (e.g., *dtheta* = 2 °) yields a steeper recovery landward. The profile for *dtheta* = 14 ° aligns closely with the measured slope transition over most of the zoomed reach. It is also clearly shown in Figure 5.26, Figure 5.27, Figure 5.28 and Figure 5.29. Overall, the results suggest that *dtheta* chiefly controls the morphology around the dune toe by modulating directional wave energy distribution and the longshore component of transport; a moderate resolution ($6°–14°$) offers a good balance between skill and computational cost for this case.

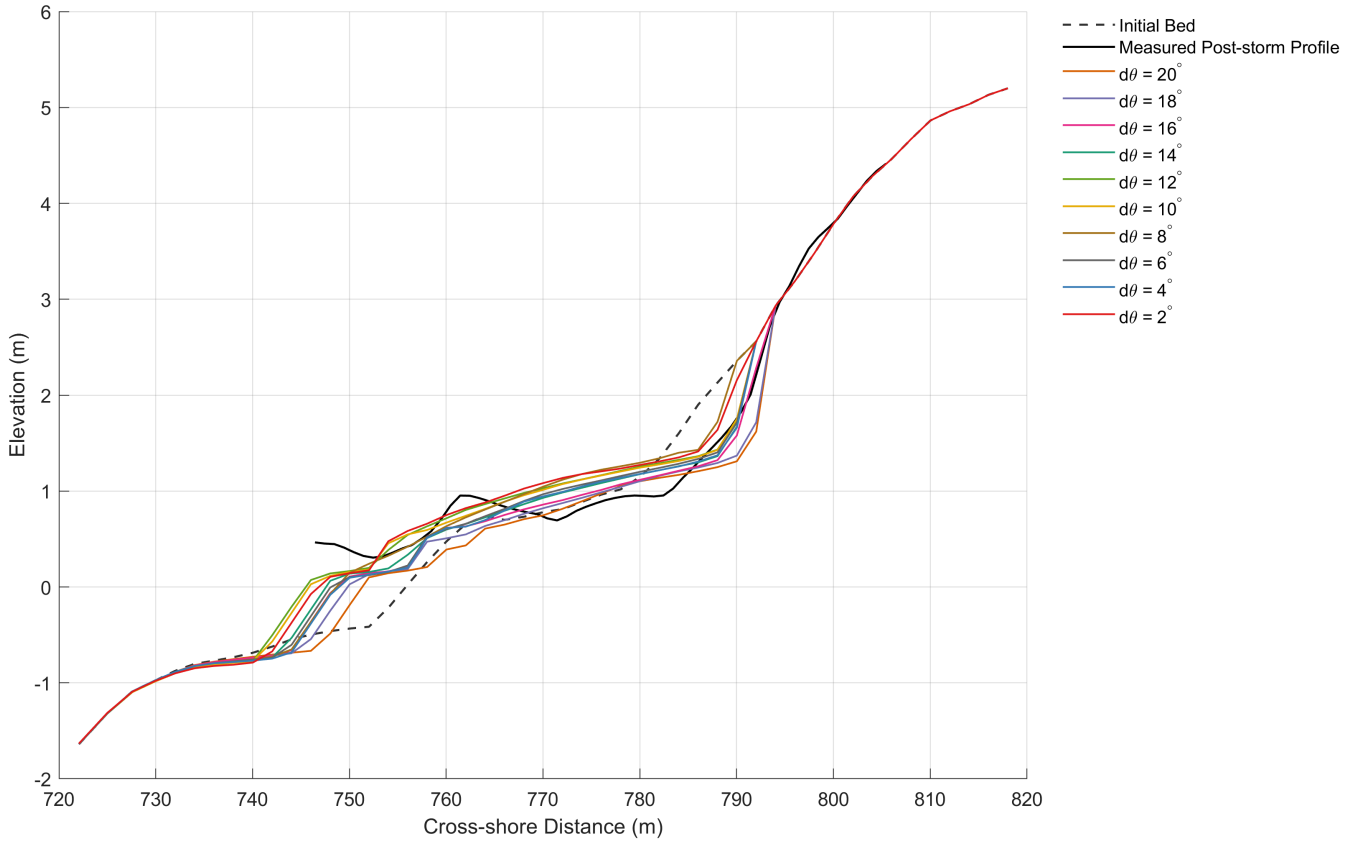

Figure 5.25: Simulated bed levels for each value of dtheta

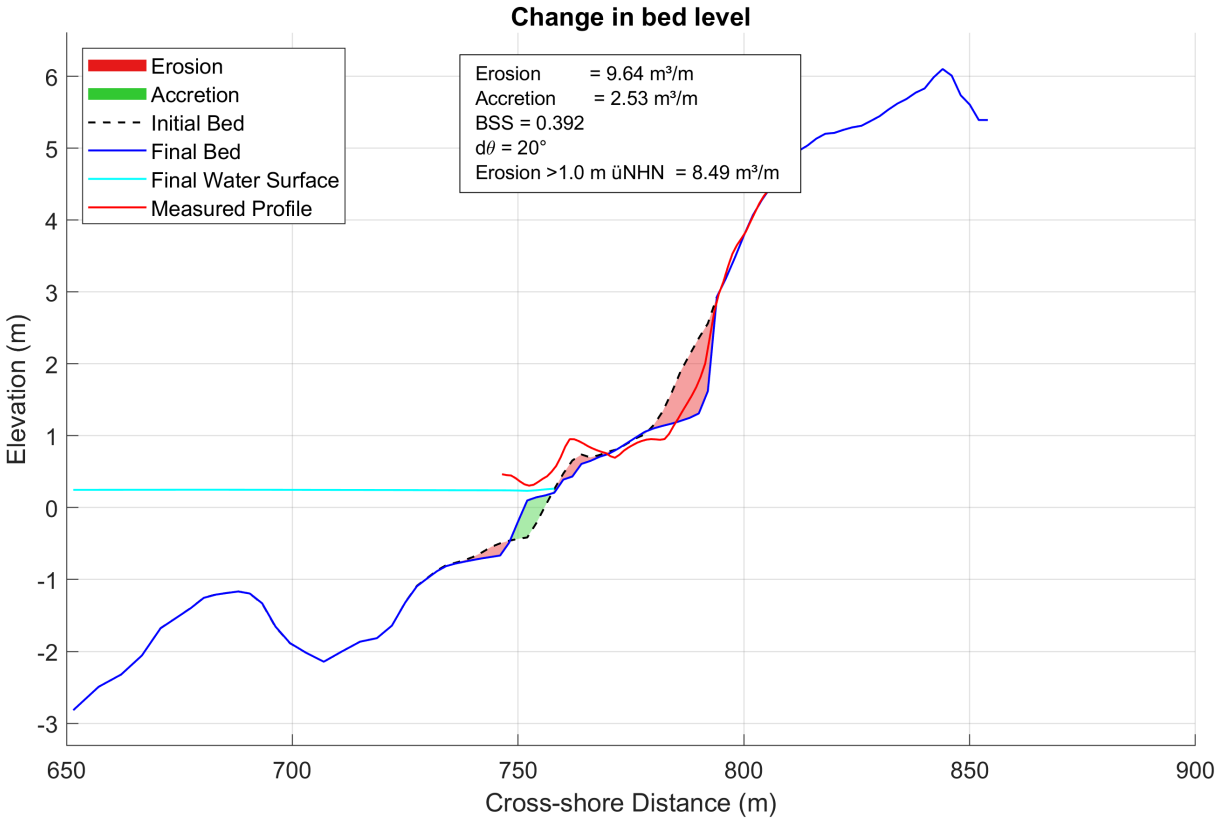

Figure 5.26: Observation in change in bed level (dtheta = 20 °)

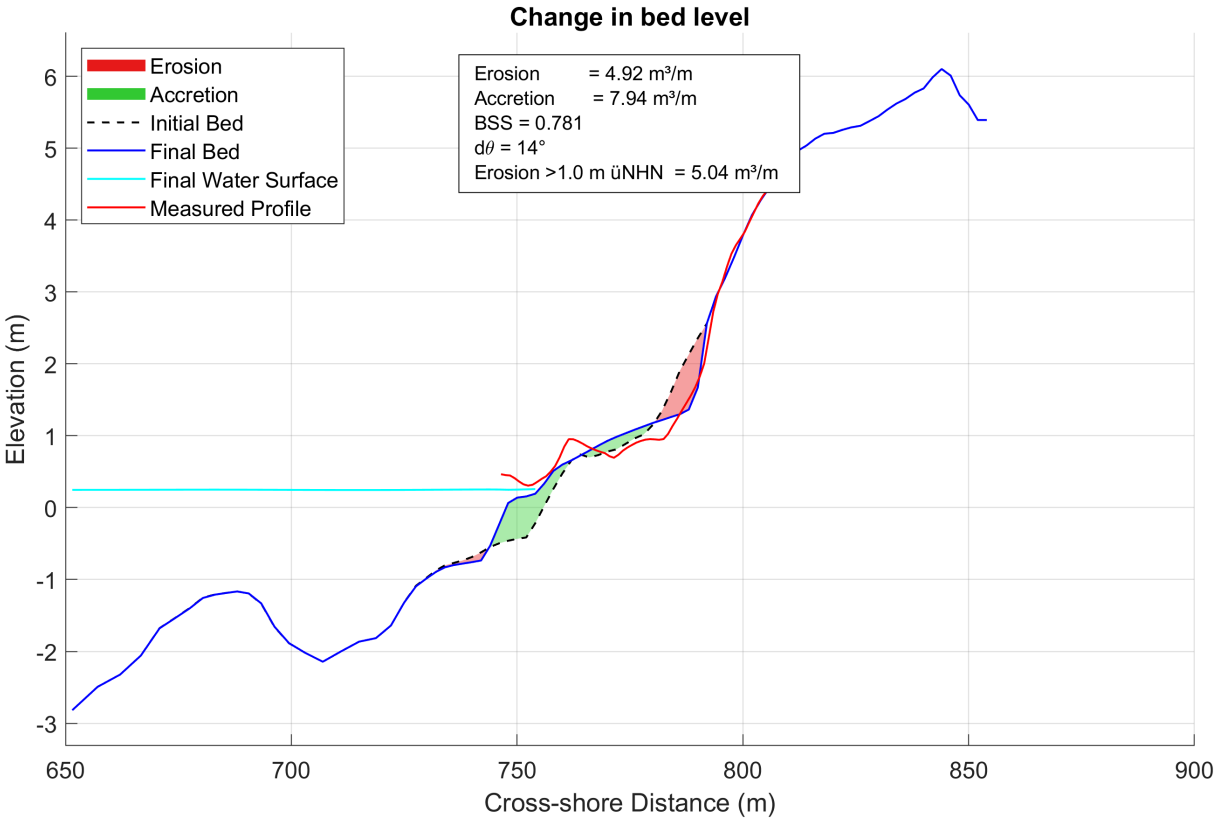

Figure 5.27: Observation in change in bed level (dtheta = 14 °)

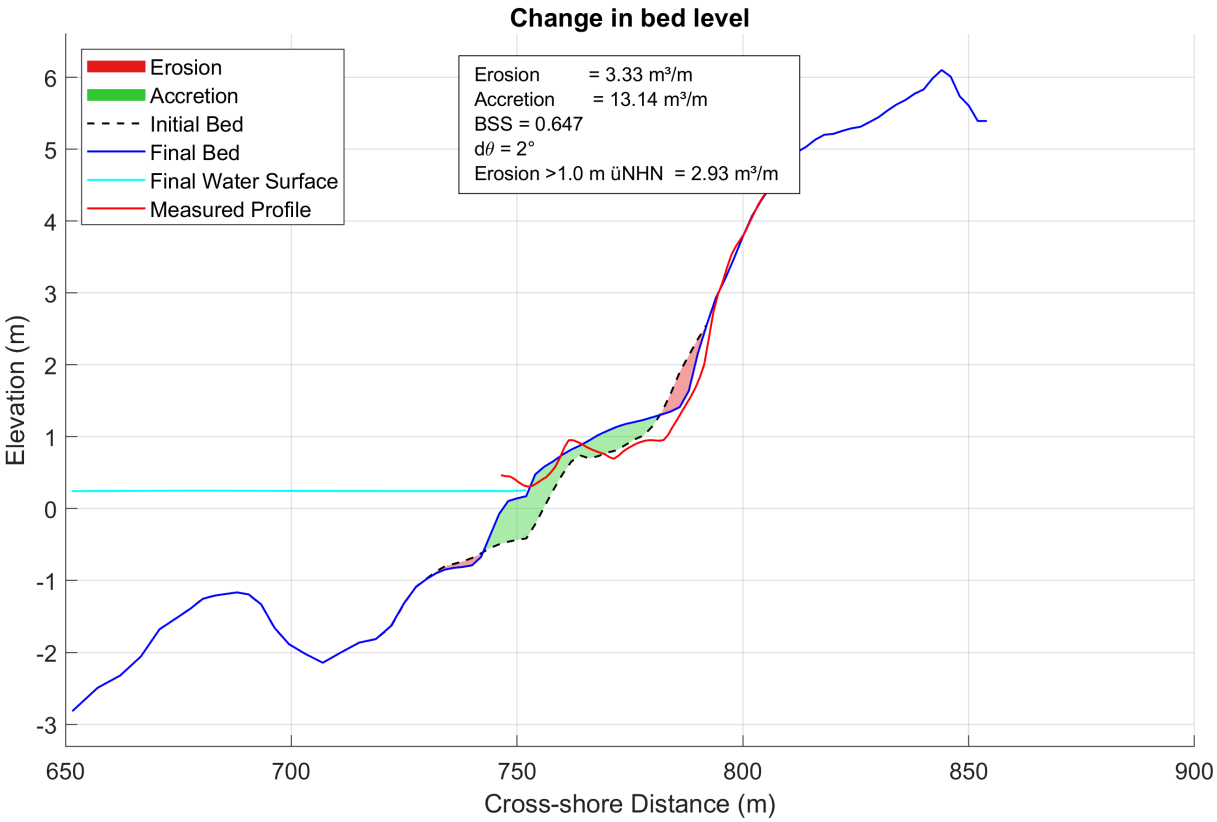

Figure 5.28: Observation in change in bed level (dtheta = 2 °)

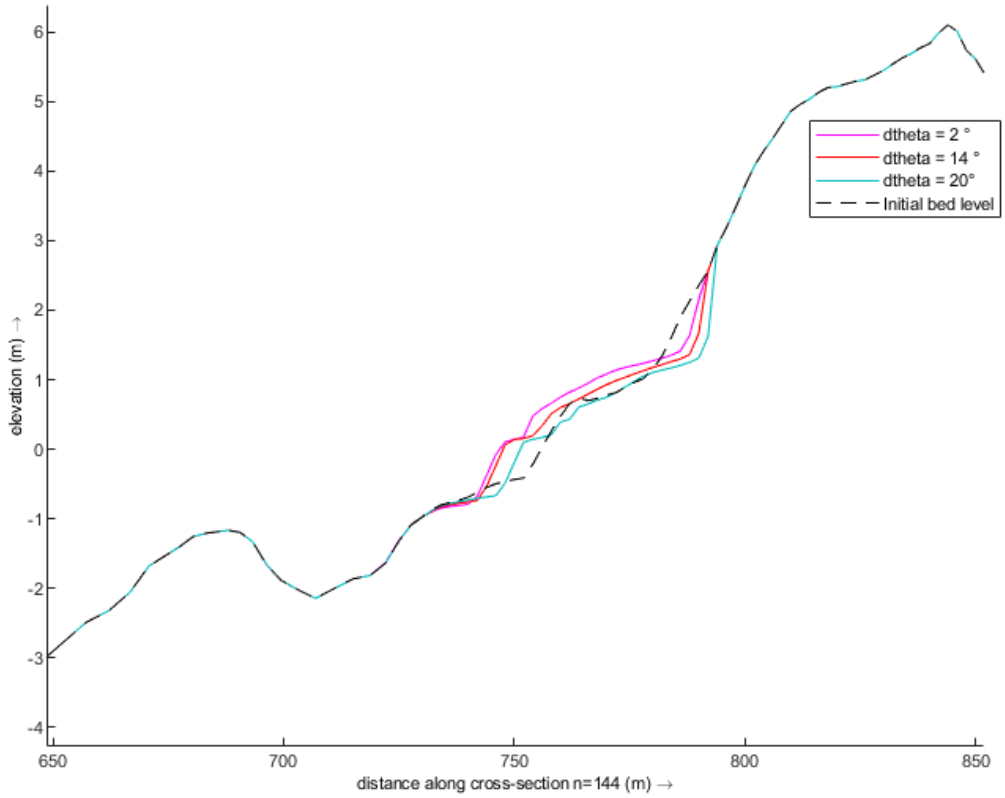

Figure 5.29: Observation in change in bed level for dtheta value of 2°,14° and 20°

Figure 5.30 illustrates the variation of cross-shore (u) and longshore (v) velocities at observation point 1 as a function of the wave directional spreading parameter *dtheta*. At early times (3 h), u is positive (onshore-directed, ≈ 0.3–0.5 m/s) and v is weakly positive (≈0.2 m/s), indicating onshore inflow with a developing alongshore current. At later times (60–72 h), both components reverse: u becomes strongly offshore-directed (up to –0.7 m/s) and v negative (down to –0.6 m/s), showing the establishment of seaward transport and a reversal in longshore flow. The effect of *dtheta* is evident, with larger spreading angles (≈ 20°) yielding smoother, weaker responses, while smaller values (≈ 2°) enhance flow magnitudes and variability. Overall, the results highlight the sensitivity of nearshore circulation to wave spreading, with narrower spreading intensifying both cross-shore export and longshore current variability, thereby influencing sediment transport near the dune toe.

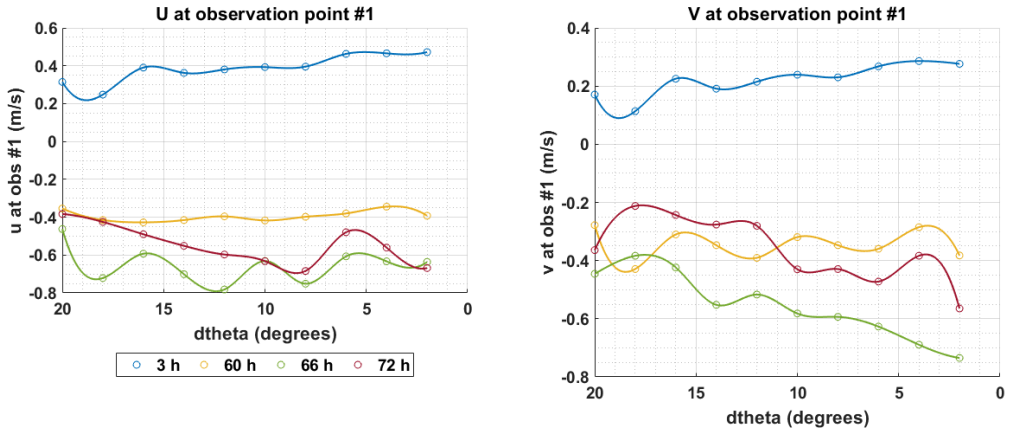

Figure 5.30: Observation of flow velocities at observation point 1 for different values of dtheta

5.3.7 Variation of Angle of Wave Incidence

To isolate the wave-incidence angle, i.e. the angle between the shore-normal and the direction of wave incidence, runs were repeated with only *theta* varied between simulations. The definition of *theta* used in these simulations is further explained in Figure 5.31. An arbitrary *theta* is shown, where angles to the right of the shore-normal are treated as positive and those to the left as negative when observed from the land side. The angle of wave incidence relative to the shore-normal was calculated from the values provided in the wave.txt file, where the angles are given relative to true North. The angles were varied at 10° intervals from the shore-normal.

For all these cases, standard profiles were selected, and the adopted bathymetry is shown in Figure 5.32. The boundary forcing was limited to a 20 h window based on tide and wave data. The hydrodynamic forcing applied in the simulations consists of a 20-hour window of wave and surge conditions (Figure 5.33). The upper panel shows the variation of significant wave height (H_{sig}) and peak wave period (T_{peak}), while the lower panel illustrates the storm surge development. These conditions were imposed uniformly across all simulations for the variation of θ. All other parameters were used as default but following the result observed in above section regarding the optimum value of dtheta, the value of dtheta was used as 14. Also, for relatively faster simulation, the morfac value was set to 15. The `params.txt` file generated x-directional cells as $nx = 176$ and y-directional cells as $ny = 276$, the cells being size varying.

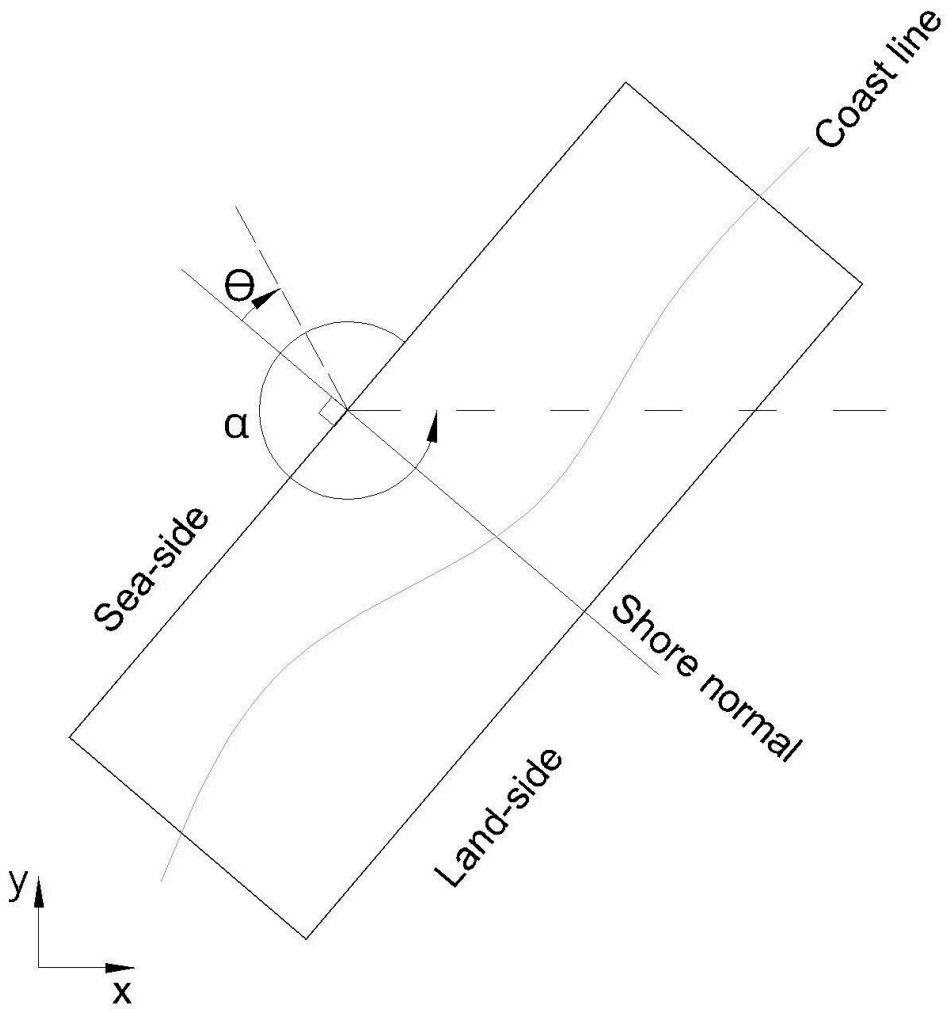

Figure 5.31: Illustration of angle of wave incidence - theta

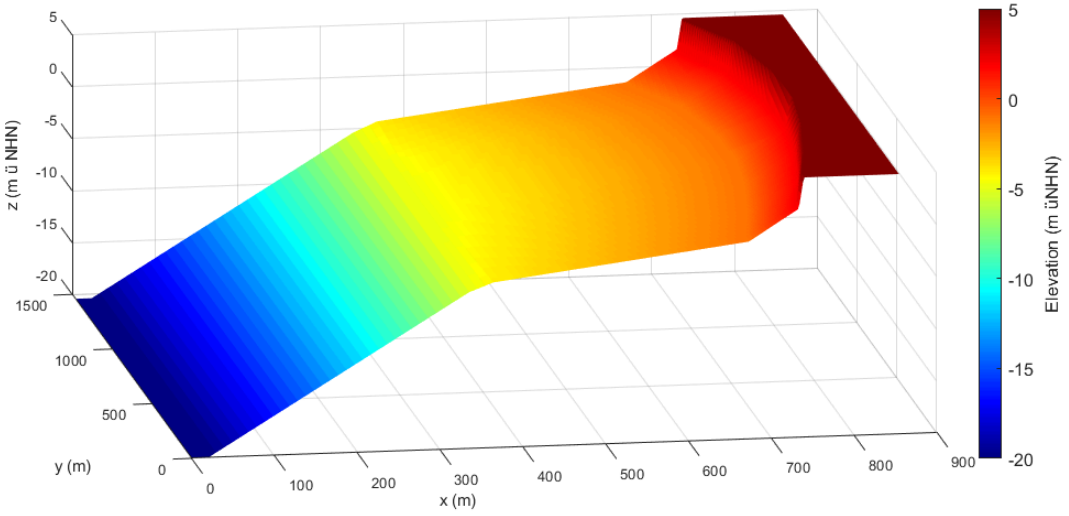

Figure 5.32: Bathymetry used for the variation of theta

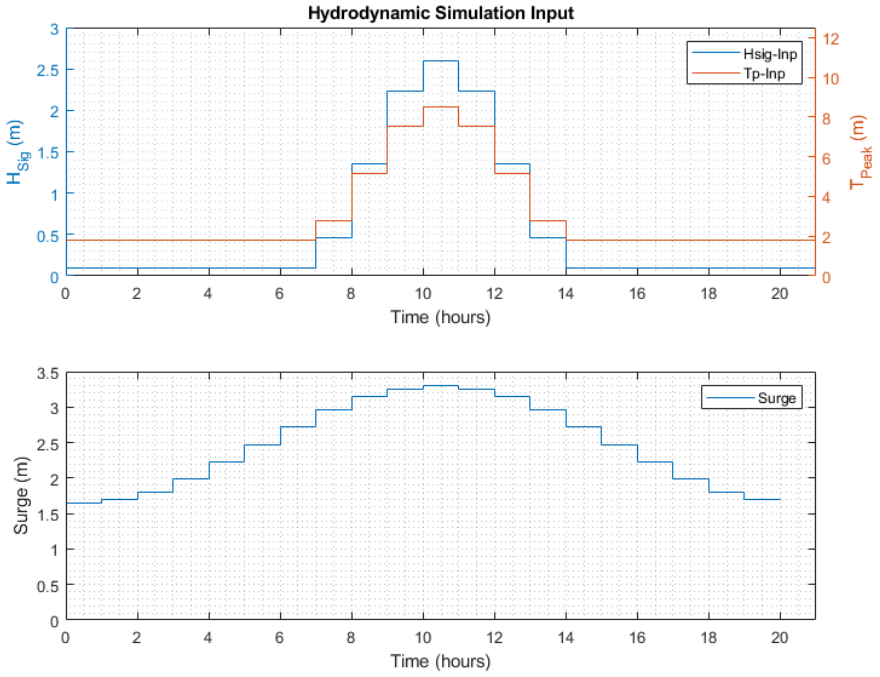

Figure 5.33: Hydrodynamic input used for the variation of theta

Volume Analysis

Figure 5.34 illustrates the balance between erosive losses and depositional gains as a function of wave angle. At shore-normal incidence, both erosion and accretion are relatively small, reflecting localized scarping and limited offshore transport. However, With increasing θ, erosion volumes grow steadily, paralleled by rising accretion volumes that signal significant nearshore redistribution of dune-derived sediments. Importantly, the accretion increase is not sufficient to offset erosive losses at the dune face, implying a net vulnerability of the coastal profile under oblique storm.

Figure 5.35 reveals a strong dependency of dune response on the incident wave angle θ. Erosion volumes are lowest at shore-normal incidence ($\theta = 0°$) and increase substantially till 40°. Conversely, accretion volumes also grow with obliquity, indicating a compensating sediment redistribution. Notably, erosion above 1 m üNHN follows the same cubic trend as total erosion, highlighting that dune-face scarping is most intense under oblique forcing. This pattern aligns with findings by De Winter & Ruessink (2017) who showed that even moderate deviations from shore-normal incidence ($\theta \geq 10–15°$) can enhance dune erosion volumes to the same order as moderate sea level rise. The asymmetry between left and right incidence further underlines the importance of alongshore sediment transport, driven by wave obliquity, as a governing factor in dune response.

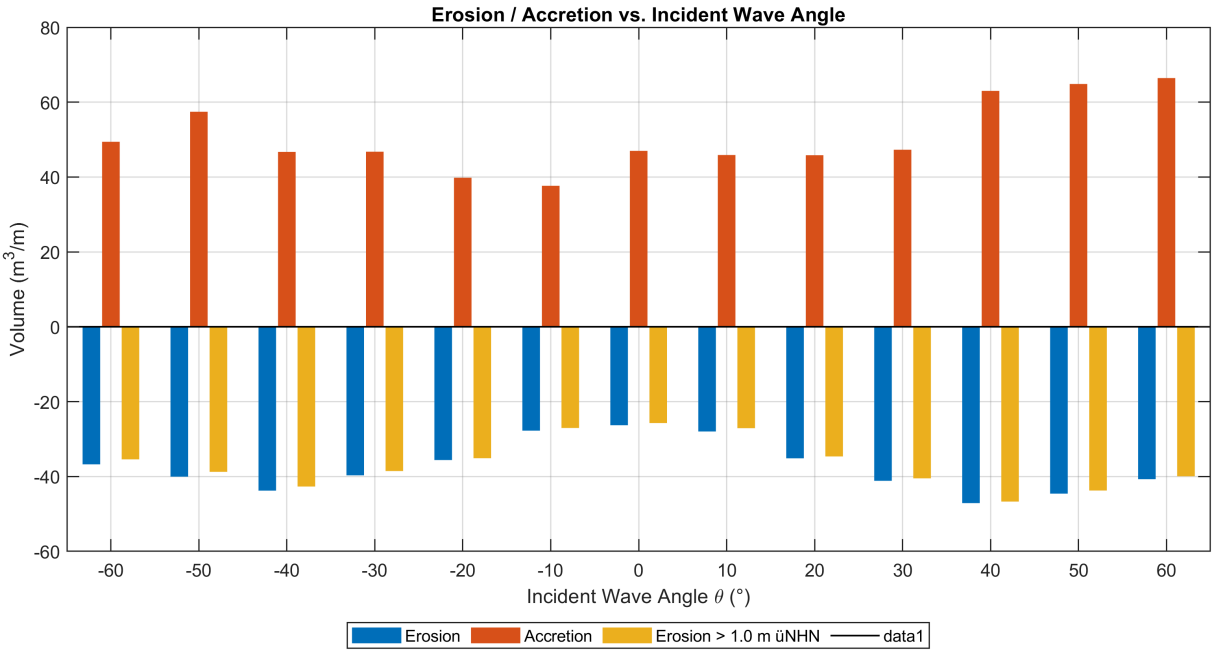

Figure 5.34: Magnitude of erosion and accretion volumes in accordance with angle of wave incidence (θ)

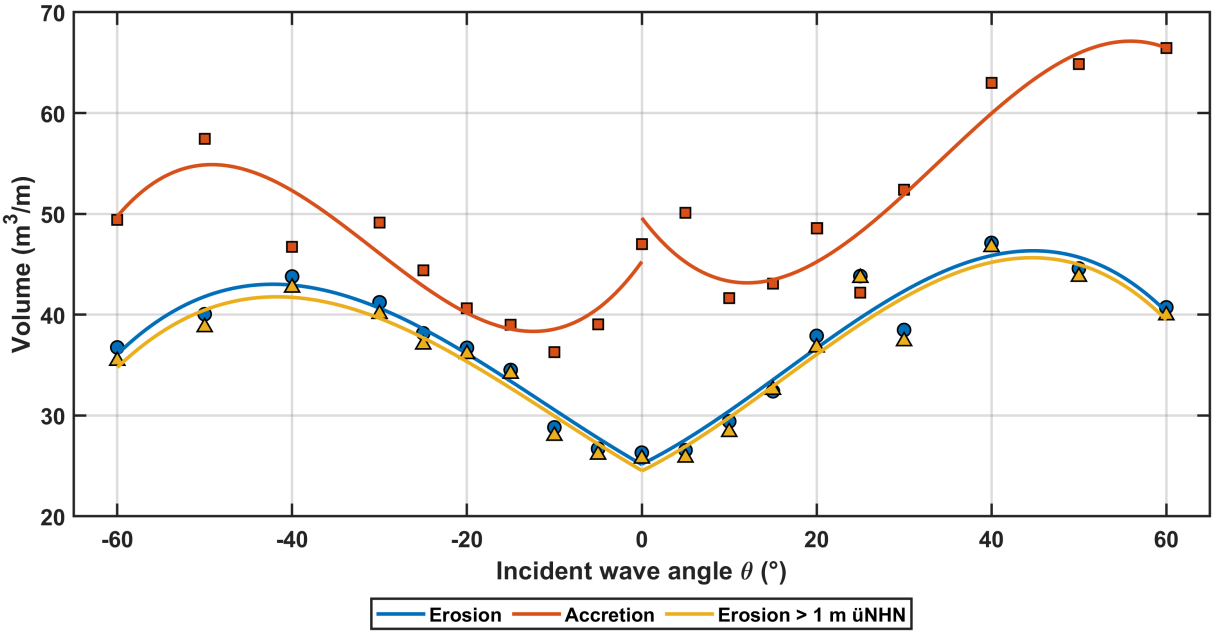

Figure 5.35: Erosion and accretion volumes left and right of shore normal

As shown in Figure 5.36, the comparatively low erosion and accretion volumes at shore-normal incidence (θ = 0°) indicate that perpendicular wave attack leads to localized dune scarping but limited sediment redistribution. In contrast, oblique waves introduce a strong longshore current component that enhances sediment mobilization, resulting in higher volumetric erosion and greater nearshore or alongshore deposition. The results therefore suggest that while normal wave incidence produces sharp dune scarps, oblique incidence governs the magnitude of sediment exchange between the dune and nearshore system. This is also verified by Figure 5.37 and Figure 5.38. In those figures, when waves attack the

model domain at a positive angle of 40° relative to the shore-normal, they transport the eroded material in the direction of attack. Conversely, when waves approach at 40° to the left of the shore-normal, more sedimentation occurs in that direction.

To further illustrate this behaviour, the GLM velocity field at time step $nt = 64$ is shown in Figure 5.39. The velocity arrows were extracted at specific cross-shore and longshore grid positions ($m = 60, 120$; $n = 60, 116, 172, 229$), thereby capturing four cross-shore sections and two longshore sections. The green and orange vectors correspond to θ = 40°, while the pink and red vectors represent θ = –40°. The mirrored pattern of these velocity fields confirms that wave obliquity generates distinct longshore currents with opposite orientations, consistent with the observed sediment redistribution. Cross-shore velocities dominate near the dune toe, whereas longshore components become more pronounced seaward, reflecting the combined effect of refraction and oblique wave forcing. This supports the interpretation that directional wave attack fundamentally alters sediment pathways, with the GLM velocities providing spatially explicit evidence of the mechanisms driving erosion–accretion asymmetry.

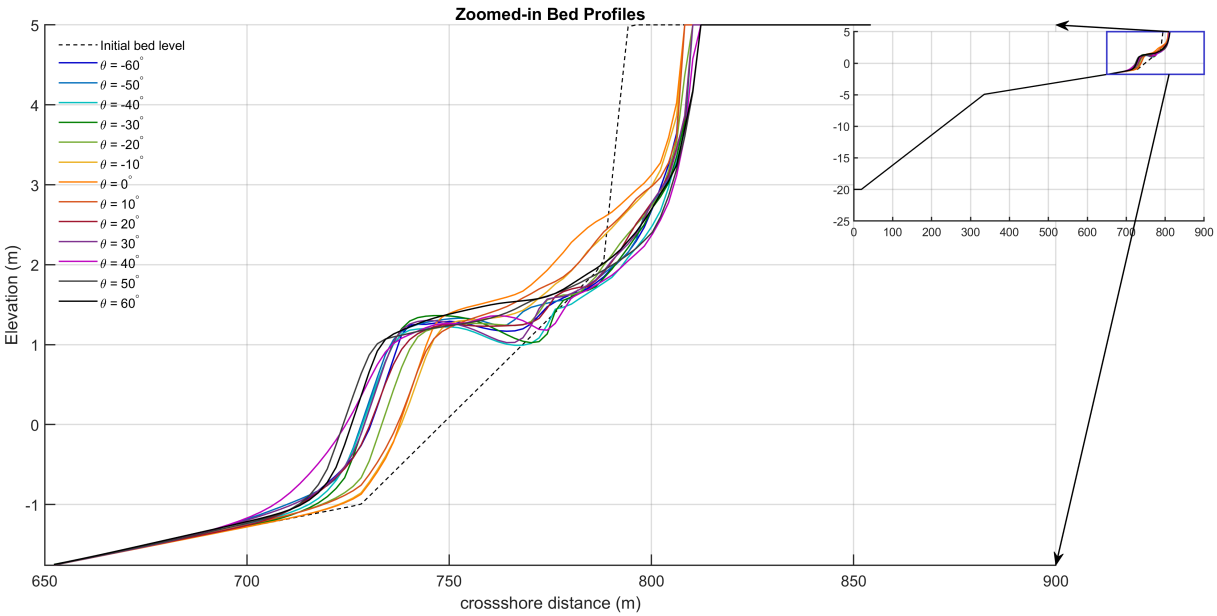

Figure 5.36: Change in bed level with respect to change in θ

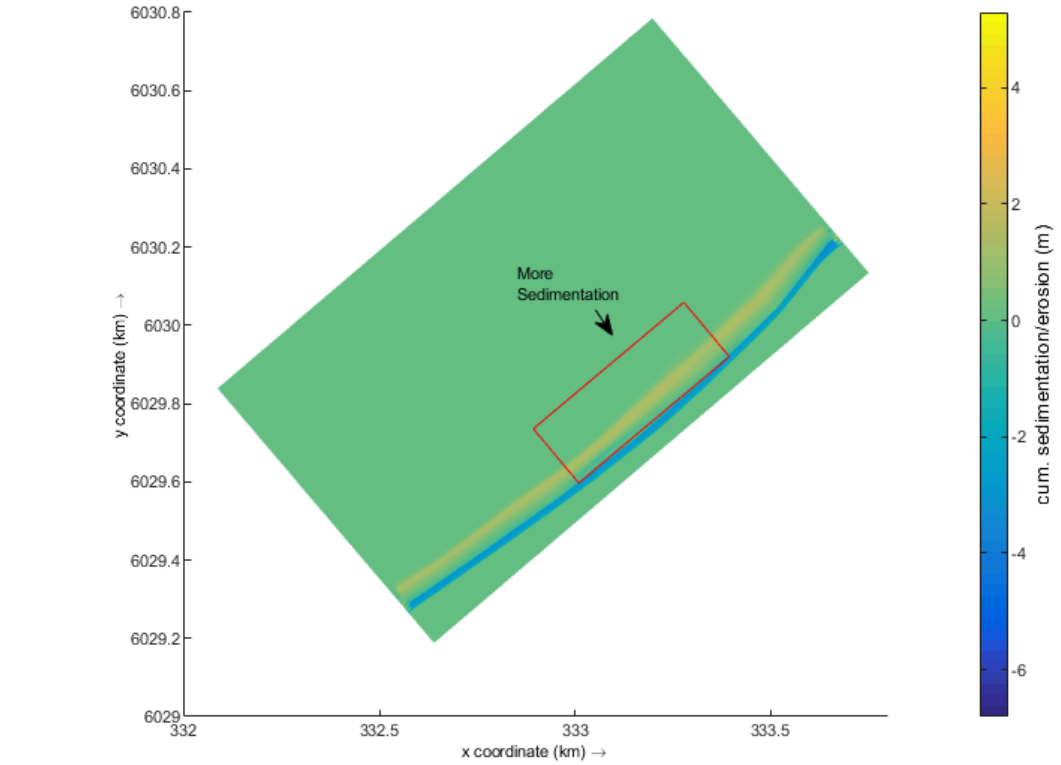

Figure 5.37: Observation of cumulative sedimentation/erosion for theta = −40°

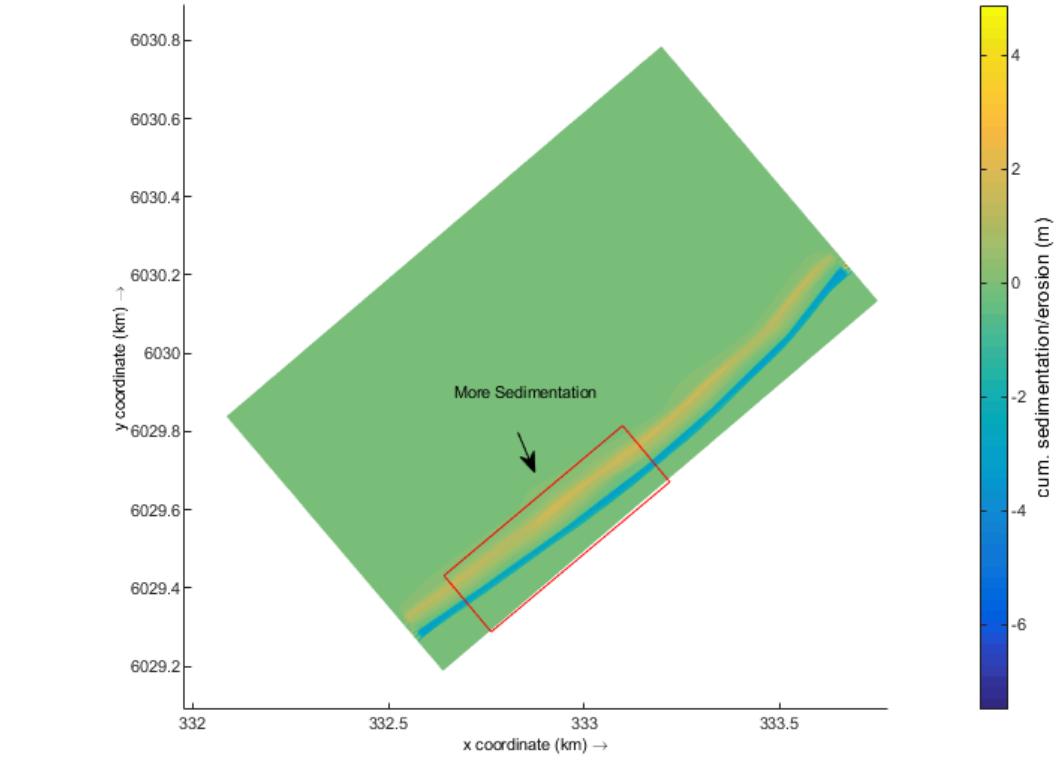

Figure 5.38: Observation of cumulative sedimentation/erosion for theta = 40°

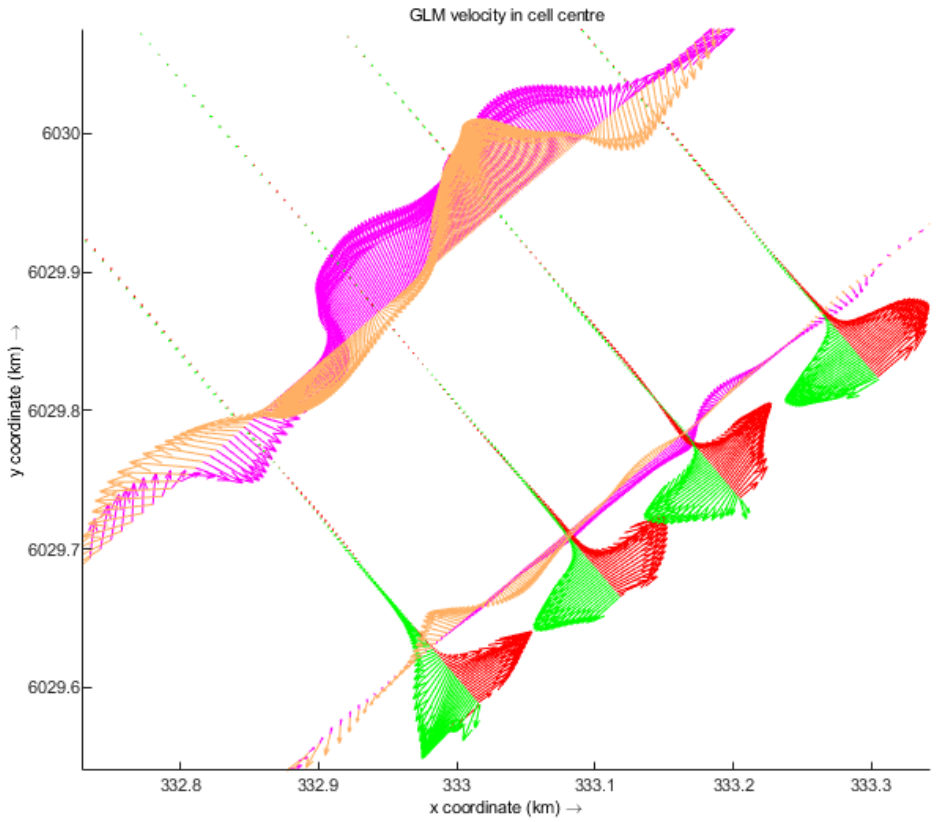

Figure 5.39: GLM velocities at cell centre showing direction of sediment transport for theta value of −40° and 40°

6 Conclusion and Outlook

6.1 Sensitivity based on Statistics

The statistical sensitivity analysis based on LHS provided initial insights into parameter influences but was constrained by the limited number of completed runs. Among the tested parameters, *facua* showed the most consistent, though still marginal, correlation with model performance, with lower values generally associated with higher BSS and lower RMSE. In contrast, *gamma* exhibited opposite but similarly weak trends, while *porosity* and *gamma2* displayed negligible influence within the tested ranges, leading to the exclusion of *por* from subsequent analyses. Overall, the results demonstrated that despite some indication of sensitivity to *facua*, the small ensemble size, high computational cost and instability of certain simulations prevented statistically robust conclusions. Consequently, the statistical approach was deemed insufficient for reliable calibration guidance, necessitating a shift toward a OAT sensitivity analysis to capture clearer parameter effects.

6.2 GLUE-based Parameter Sensitivity

Based on the application of the **GLUE** methodology, *gamma* was identified as the most sensitive parameter (K-SD = 0.389), followed by *facua* (K-SD = 0.195) and *gamma2* (K-SD = 0.175) This outcome is not consistent with existing literature, where *facua* has generally been reported as the most important and influential parameter in coastal dune erosion modeling. The divergence observed in this study may be attributed to the limited number of simulations made, which likely constrained the robustness of the sensitivity assessment.

6.3 Application of OAT Method

Variation of facua

The sensitivity analysis of *facua* showed that decreasing its value improved statistical skill (highest BSS ≈ 0.61) but intensified dune erosion. Lower facua values produced larger negative cumVdt values, indicating stronger net erosion, particularly near the dune toe. Erosion above 1 m üNHN consistently declined with increasing facua, confirming its suppressive effect on dune scarping. Spatial patterns revealed concentrated erosion and deposition within the surf and swash zones (≈ 740–800 m from offshore). GLM velocity fields corroborated the erosion–sedimentation zones, with velocity magnitudes aligning with areas of strongest morphological change.

6.3.1 Variation of gamma and gamma2

The sensitivity analysis of *gamma* demonstrated that model skill improved as values increased slightly above the default (0.46), with optimal performance around 0.47, after which BSS declined. Cumulative erosion volumes followed a similar pattern, with intermediate gamma values yielding the least erosion, while both lower and higher values intensified scarping. This reflects the dual role of gamma in the wave-breaking threshold: smaller values trigger earlier breaking and turbulence, whereas larger values delay breaking, allowing stronger wave attack at the dune toe. Cross-shore profiles confirmed only subtle morphological differences, but GLM velocity fields showed delayed breaking for higher *gamma*, consistent with greater landward transport potential. Overall, *gamma* was found to exert a moderate but secondary influence compared to *facua*, mainly affecting the timing and location of wave energy dissipation.

In contrast, variation of the roller parameter *gamma2* showed weaker and less systematic effects. The tested range (0.3366–0.3944) did not allow for a reliable cubic fit, yet tabulated results indicated that higher values, particularly near 0.40, provided the best agreement with measured profiles. This suggests that *gamma2* contributes to shaping the roller energy and momentum transfer, but its role is less dominant than facua or gamma.

6.3.2 Change of morfac Value to 20

By increasing the morphological acceleration factor (*morfac*) to 20, it was possible to explore parameter sensitivity more efficiently while maintaining consistent hydrodynamic conditions. The relationship between facua and BSS was found to weaken with increasing gamma2, showing the strongest response at gamma2 = 0.38 and becoming negligible at gamma2 = 0.40. In contrast, the influence of facua on cumulative volume change (cumVdt) became more structured at higher gamma2 values, with the most systematic trend observed at gamma2 = 0.40. These results indicate that the interaction between facua and gamma2 strongly shapes erosion–accretion dynamics, particularly under higher gamma2 conditions. A representative profile with the highest BSS (0.8081) and low RMSE (0.1676) confirmed that the main dune erosion patterns were well reproduced, with localized erosion concentrated near the dune toe. Overall, the accelerated simulations with morfac = 20 effectively captured key dune erosion processes while highlighting the coupled sensitivity of facua and gamma2.

6.3.3 Change in Dimension of Model Grid

By reducing the model grid in the longshore direction while maintaining the cross-shore length, computational efficiency was improved without compromising spatial resolution in the surf and dune zones. Under these conditions, sensitivity tests of the breaking parameter *gamma* revealed marked improvements in model skill compared to the default setup. The best performance was obtained for *gamma* = 0.5, which achieved the highest BSS (0.8562) and lowest RMSE (0.1526). The corresponding profile showed close agreement with the measured post-storm morphology, particularly around the dune toe where erosion and deposition patterns were accurately reproduced. These results demonstrate that grid optimization in combination with refined parameterization can significantly enhance model efficiency and predictive skill.

6.3.4 Variation of dtheta

The sensitivity analysis of the wave directional resolution parameter *dtheta* revealed that model performance was strongly influenced by the degree of angular spreading. Finer resolutions (2°–10°) generally improved statistical skill (BSS) and supported balanced sediment redistribution, while coarser resolutions (>16°) led to progressively larger net erosion volumes and reduced accretion. This pattern was attributed to the reduced ability of the model at larger dtheta to capture directional spreading and wave refraction, causing cross-shore erosion to dominate without compensating deposition. Cross-shore profiles confirmed that moderate dtheta values (≈14°) provided the best match to measured post-storm morphology, particularly around the dune toe, while velocity diagnostics further demonstrated that narrow directional bins enhanced nearshore circulation intensity. Taken together, the results indicate that a moderate directional resolution (≈14°–16°) represents the most credible compromise, achieving both high model skill and realistic morphodynamic responses at manageable computational cost.

6.3.5 Variation of theta

The sensitivity analysis of the wave incidence angle theta showed that shore-normal waves (*theta* = 0°) produced localized dune scarping with limited sediment redistribution, while increasing obliquity enhanced both erosion and accretion volumes. Erosion intensified progressively up to ± 40°, with compensating deposition occurring in the nearshore and alongshore directions, though not sufficient to offset dune-face losses. Cross-shore profiles confirmed that oblique incidence governs the magnitude of sediment exchange between dune and nearshore systems, in contrast to the more confined response at normal incidence. The GLM velocity fields further illustrated that *theta* = ± 40° generated mirrored longshore currents, driving asymmetric sediment transport depending on wave

approach direction. Overall, these results highlight that oblique wave incidence fundamentally alters dune response by strengthening longshore currents and enhancing volumetric erosion.

6.4 Limitations

While this study provides valuable insights into the sensitivity of XBeach parameters in reproducing dune erosion processes, several limitations must be acknowledged. These constraints stem mainly from computational restrictions, methodological simplifications, and data availability, all of which influence the scope and generality of the findings. The following key limitations were identified:

1. **Limited ensemble size:**
   The number of simulations performed was relatively small due to the high computational demand of the netCDF-MPI XBeach implementation. This restricted the robustness of statistical analyses (e.g., regression, GLUE) and likely contributed to atypical sensitivity outcomes, such as gamma being identified as the most sensitive parameter instead of facua.
2. **Single transect studied:**
   Only one transect was analyzed in this study, meaning that sensitivity results are restricted to a single cross-shore profile. Since bathymetry varies spatially, model responses to parameters can differ across locations even under identical hydrodynamic forcing. This spatial limitation reduces the ability to generalize the findings to broader coastal settings.

6.5 Conclusion

The aim of this thesis was to assess the sensitivity of key XBeach simulation parameters in reproducing dune erosion processes at the Baltic Sea site of Ahrenshoop, with the goal of improving model calibration and coastal management strategies.

The achievements of the objectives outlined in Section 1.4 are summarised below:

1. *Identify and analyze key simulation parameters that govern morphodynamic responses under extreme hydraulic events (e.g., storm surges and wave attack).*
   The study demonstrated that, besides the widely recognised influence of *facua* and *gamma*, parameters such as *dtheta* (directional resolution) and *theta* (angle of wave incidence relative to the shore-normal) also play an essential role in controlling dune erosion patterns and morphodynamic responses under extreme hydraulic conditions.
2. *Evaluate the sensitivity of dune erosion and erosion volumes to variations in wave conditions, boundary conditions, and model inputs.*
   Sensitivity tests across multiple parameter ranges revealed clear trends in BSS, erosion

volumes and profile changes. The analyses confirmed that model performance is strongly dependent on both hydrodynamic input parameters (*facua*, *gamma*) and directional parameters (*dtheta*, *theta*), each shaping different aspects of dune erosion processes.

3. *Quantify the effect of individual parameters on modelled outcomes and explore the possibility of aggregating them into global parameters to simplify model calibration.*
   Parameter effects were quantified using LHS-based statistics, GLUE and OAT experiments. *Facua* controlled the erosive response–skill trade-off (lower *facua* produced higher BSS but larger erosion), *gamma* modulated breaking location and run-up, *gamma2* provided secondary adjustments to roller energy and *dtheta* governed directional spreading and alongshore transport representation. While a single "global" parameter could not replace these distinct controls, the combined action of (*facua*, *gamma*) for wave dissipation and (*dtheta*, *theta*) for directionality offers a practical grouping for calibration and scenario testing.
4. *Formulate recommendations for parameter ranges that support the design and improvement of dune erosion management strategies in comparable coastal settings.*
   Based on the ensemble examined, credible settings for the studied event and site include: slightly elevated *gamma* (0.47–0.50), moderate *gamma2* (0.38–0.40) and *dtheta* in the range 6°–14° (with 14°–16° giving the best profile agreement at acceptable cost). *Facua* should be selected with explicit acknowledgment of the trade-off: lower values improve statistical skill but increase dune scarping and net erosion; mid-range values reduce erosion while retaining acceptable skill. Oblique *theta* markedly increases erosion and alongshore redistribution and should be considered in design scenarios and early-warning assessments.

Taken together, the thesis clarifies which XBeach parameters most strongly influence dune erosion at Ahrenshoop, demonstrates how directional resolution and wave obliquity shape sediment pathways, and provides calibrated parameter guidance that balances statistical skill with physically realistic erosion magnitudes. These results can inform targeted calibration, scenario evaluation and the design of adaptive coastal protection strategies for similar Baltic settings.

6.6 Outlook

Based on the findings and limitations identified in this study, the following recommendations are proposed to improve dune-erosion modelling on the Baltic coast:

1. **Starting with synthetic transects prior to natural profiles:**
   Initial sensitivity analyses on synthetic cross-shore transects with prescribed dune

crest, toe and seaward slope are recommended. This setup facilitates isolation of parameter effects (e.g., *facua*, *gamma*, *gamma2*, *dtheta*) with shorter and more stable runs; calibrated insights may then be transferred to natural profiles. The reliance on a natural profile in this study (except the *theta* series) contributed to longer runtimes and occasional instabilities.

2. **Operational settings for routine sensitivity analyses:**
   The use of *morfac* = 15 - 20 in combination with a directional resolution *dtheta* in the range 10°–14° is recommended, as this balance yielded strong skill with credible erosion magnitudes in this work. Brief convergence checks (e.g., *morfac* = 10/15/20 and *dtheta* = 8/12/16°) on a subset of cases are advisable to confirm consistency of key diagnostics (BSS, RMSE, dune-toe retreat, cumVdt).

3. **GLUE ensemble design and ensemble size::**
   Construction of the GLUE ensemble on synthetic profiles with a reduced forcing window centered on peak surge/wave energy (≈ 8–12 h) is expected to increase numerical stability and the number of simulations completed within a given time, enabling ≥ 100–200 behavioral runs with space-filling sampling (e.g., LHS/Sobol). A multi-criteria likelihood (BSS, RMSE, dune-toe/crest displacement, volumetric bias) with reported K–SD uncertainty is recommended. After narrowing priors for facua, gamma, gamma2, and dtheta, the calibrated ranges can be transferred to natural profiles across multiple transects for site-wide validation.

References

Aakjær, P., & Buch, E. (2022,). *The 1872 super-storm surge in the Baltic–the Danish perspective, Die Küste, 92, 125–139*.

Abdelaal, S., & Oumeraci, H. (2016,). *Modelling Strategies with XBeach (XBeach Manual)* (p.). https://doi.org/10.13140/RG.2.1.4199.0644

Andersen, T. L., & Frigaard, P. (2011). *Lecture notes for the course in water wave mechanics*.

Andrews, D., & McIntyre, M. (1978). An exact theory of nonlinear waves on a Lagrangian-mean flow. *Journal of Fluid Mechanics*, *89*(4), 609–646.

Arkel, M. van. (2016). *Towards an efficient sensitivity analysis of wave forcing in coastal erosion studies*.

Bae, H., Do, K., Kim, I., & Chang, S. (2022). Proposal of parameter range that offered optimal performance in the coastal morphodynamic model (XBeach) through GLUE. *Journal of Ocean Engineering and Technology*, *36*(4), 251–269.

Battjes, J. A. (1974). Surf similarity. In *Coastal Engineering 1974: Coastal Engineering 1974* (pp. 466–480).

Bernier, N. B., Hemer, M., Mori, N., Appendini, C. M., Breivik, O., Camargo, R. de, Casas-Prat, M., Duong, T. M., Haigh, I. D., Howard, T., & others. (2024). Storm surges and extreme sea levels: Review, establishment of model intercomparison and coordination of surge climate projection efforts (SurgeMIP). *Weather and Climate Extremes*, *45*, 100689.

Beven, K., & Binley, A. (1992). The future of distributed models: model calibration and uncertainty prediction. *Hydrological Processes*, *6*(3), 279–298.

Bosboom, J., & Stive, M. J. (2023). *Coastal dynamics*. TU Delft OPEN Publishing.

Cazenave, A., & Cozannet, G. L. (2014). Sea level rise and its coastal impacts. *Earth's Future*, *2*(2), 15–34.

Ciavola, P., Ferreira, O., Dongeren, A. V., Vries, J. V. T. d., Armaroli, C., & Harley, M. (2014). Prediction of storm impacts on beach and dune systems. *Hydrometeorological Hazards*, 227–252.

Confalonieri, R., Bellocchi, G., Bregaglio, S., Donatelli, M., & Acutis, M. (2010). Comparison of sensitivity analysis techniques: a case study with the rice model WARM. *Ecological Modelling*, *221*(16), 1897–1906.

Daly, C. (2009). Low frequency waves in the shoaling and nearshore zone. *Unpublished M. Sc. Thesis. Delft: Technical University of Delft*.

Daly, C., Roelvink, D., Dongeren, A. van, Vries, J. v. T. de, & McCall, R. (2012). Validation of an advective-deterministic approach to short wave breaking in a surf-beat model. *Coastal Engineering*, *60*, 69–83.

Dashtgard, S. E., MacEachern, J. A., Frey, S. E., & Gingras, M. K. (2012). Tidal effects on the shoreface: towards a conceptual framework. *Sedimentary Geology*, *279*, 42–61.

De Winter, R., & Ruessink, B. (2017). Sensitivity analysis of climate change impacts on dune erosion: case study for the Dutch Holland coast. *Climatic Change*, *141*(4), 685–701.

Dudzińska-Nowak, J. (2022). Coastal erosion, protection structures, and subsequent shoreline effects. A case study from the western Polish coast (southern Baltic Sea). *Assessing the Baltic Sea Earth System*, *94*.

Earle, S. (2015). *Physical geology*. BCcampus.

Fleischer, D. ResCAD-Neue Planungswerkzeuge für Dünensysteme an der deutschen Ostseeküste. *Wasserbau Und Wasserwirtschaft Im'stresstest'*, 113.

Fleming, K., Johnston, P., Zwartz, D., Yokoyama, Y., Lambeck, K., & Chappell, J. (1998). Refining the eustatic sea-level curve since the Last Glacial Maximum using far-and intermediate-field sites. *Earth and Planetary Science Letters*, *163*(1–4), 327–342.

Furmańczyk, K., & Dudzińska-Nowak, J. (2009). Extreme storm impact on the coastline changes–South Baltic example. *Journal of Coastal Research SI*, *56*, 1637–1640.

Gai, Y., Li, L., Li, Z., & Shi, H. (2025). The Optimization of Four Key Parameters in the XBeach Model by GLUE Method: Taking Chudao South Beach as an Example. *Journal of Marine Science and Engineering*, *13*(3), 555.

Galappatti, G., & Vreugdenhil, C. (1985). A depth-integrated model for suspended sediment transport. *Journal of Hydraulic Research*, *23*(4), 359–377.

Groll, N., Gaslikova, L., & Weisse, R. (2024). Recent Baltic Sea Storm Surge Events From A Climate Perspective. *Egusphere*, *2024*, 1–25.

Hibbard, K. A., Meehl, G. A., Cox, P. M., & Friedlingstein, P. (2007). A strategy for climate change stabilization experiments. *Eos, Transactions American Geophysical Union*, *88*(20), 217–221.

Hinkel, J., Feyen, L., Hemer, M., Le Cozannet, G., Lincke, D., Marcos, M., Mentaschi, L., Merkens, J. L., De Moel, H., Muis, S., & others. (2021). Uncertainty and bias in global to regional scale assessments of current and future coastal flood risk. *Earth's Future*, *9*(7), e2020EF001882.

Hoffmann, G., & Lampe, R. (2007). Sediment budget calculation to estimate Holocene coastal changes on the southwest Baltic Sea (Germany). *Marine Geology*, *243*(1–4), 143–156.

Holthuijsen, L., Booij, N., & Herbers, T. (1989). A prediction model for stationary, short-crested waves in shallow water with ambient currents. *Coastal Engineering*, *13*(1), 23–54.

Jensen, J., Klein, B., Kusche, J., Latif, M., Ratter, B., Rhein, M., Rovere, A., Schlurmann, T., Schulz, M., Stammer, D., & others. (2019). *Zukunft der Meeresspiegel: Fakten und Hintergründe aus der Forschung*.

Kaehler, C., Cantré, S., Schweiger, C., & Saathoff, F. (2022). Dune Erosion at the German baltic coast—Investigation and analysis of a large-scale field experiment compared to life dunes. *Journal of Marine Science and Engineering*, *10*(11), 1605.

Kiesel, J., Lorenz, M., König, M., Gräwe, U., & Vafeidis, A. T. (2023). Regional assessment of extreme sea levels and associated coastal flooding along the German Baltic Sea coast. *Natural Hazards and Earth System Sciences*, *23*(9), 2961–2985.

Kinsman, B. (1984). *Wind waves: their generation and propagation on the ocean surface*. Courier Corporation.

Kirezci, E., Young, I. R., Ranasinghe, R., Muis, S., Nicholls, R. J., Lincke, D., & Hinkel, J. (2020). Projections of global-scale extreme sea levels and resulting episodic coastal flooding over the 21st Century. *Scientific Reports*, *10*(1), 11629.

Komar, P. D., & Miller, M. C. (1975). On the comparison between the threshold of sediment motion under waves and unidirectional currents with a discussion of the practical evaluation of the threshold: Reply. *Journal of Sedimentary Research*, *45*(1).

Kurowicka, D., & Cooke, R. M. (2006). *Uncertainty analysis with high dimensional dependence modelling*. John Wiley & Sons.

McKay, M. D., Beckman, R. J., & Conover, W. J. (2000). A comparison of three methods for selecting values of input variables in the analysis of output from a computer code. *Technometrics*, *42*(1), 55–61.

Meinke, I., & Reckermann, M. (2012). *Ostseeküste im Klimawandel-Ein Handbuch zum Forschungsstand*.

Munk, W. H. (1951). *Origin and generation of waves*.

Phillips, O. (1977). The dynamics of the upper ocean, Cambridge Univ. *Press, Cambridge*.

Puleo, J., Beach, R., Holman, R. A., & Allen, J. (2000). Swash zone sediment suspension and transport and the importance of bore-generated turbulence. *Journal of Geophysical Research: Oceans*, *105*(C7), 17021–17044.

Reusch, T. B., Dierking, J., Andersson, H. C., Bonsdorff, E., Carstensen, J., Casini, M., Czajkowski, M., Hasler, B., Hinsby, K., Hyytiäinen, K., & others. (2018). The Baltic Sea as a time machine for the future coastal ocean. *Science Advances*, *4*(5), eaar8195.

Rijn, L. C. van, Walstra, D. J., Grasmeijer, B., Sutherland, J., Pan, S., & Sierra, J. (2003). The predictability of cross-shore bed evolution of sandy beaches at the time scale of storms and seasons using process-based profile models. *Coastal Engineering*, *47*(3), 295–327.

Roelvink, D., Reniers, A., Van Dongeren, A., De Vries, J. V. T., McCall, R., & Lescinski, J. (2009). Modelling storm impacts on beaches, dunes and barrier islands. *Coastal Engineering*, *56*(11–12), 1133–1152.

Roelvink, J. (1993). *Surf beat and its effects on cross-shore profiles*.

Rutgersson, A., Kjellström, E., Haapala, J., Stendel, M., Danilovich, I., Drews, M., Jylhä, K., Kujala, P., Guo Larsén, X., Halsnæs, K., & others. (2021). Natural hazards and extreme events in the Baltic Sea region. *Earth System Dynamics Discussions*, *2021*, 1–80.

Saathoff, F., Kaehler, C., & Fürst, S. (2020). Untersuchung, Analyse und Bewertung von Dünenerosionen an der deutschen Ostseeküste. *Bautechnik*, *97*(12), 856–867.

Schmidt, A., Striegnitz, M., & Kuhn, K. (2014). Integrating regional perceptions into climate change adaptation: a transdisciplinary case study from Germany's North Sea Coast. *Regional Environmental Change*, *14*(6), 2105–2114.

Schweiger, C., Kaehler, C., Koldrack, N., & Schuettrumpf, H. (2020). Spatial and temporal evaluation of storm-induced erosion modelling based on a two-dimensional field case including an artificial unvegetated research dune. *Coastal Engineering*, *161*, 103752.

Schönthaler, K., Andrian-Werburg, S., Zebisch, M., & Becker, D. (2017). *Welchen Beitrag können Satellitenfernerkundung und insbesondere Copernicus-Daten und–Dienste für die Ermittlung ausgewählter Indikatoren des Indikatoren-Sets der Deutschen Anpassungsstrategie an den Klimawandel (DAS) leisten*.

Shields, A. (1936). Anwendung der Aehnlichkeitsmechanik und der Turbulenzforschung auf die Geschiebebewegung. *Mitteilungen Der Preussischen Versuchsanstalt Für Wasserbau Und Schiffbau*, *26*, 5.

Simmons, J. (2018). *Improved model calibration techniques for predicting coastal storm erosion*.

StALU, M. (2009). Regelwerk Küstenschutz Mecklenburg-Vorpommern. *Übersichtsheft: Grundlagen, Grundsätze, Standortbestimmungen Und Ausblick. Ministerium Für Land-*

wirtschaft, Umwelt Und Verbraucherschutz Mecklenburg-Vorpommern (Hrsg.). Ostseedruck Rostock, Rostock.

Sutherland, J., Peet, A., & Soulsby, R. (2004). Evaluating the performance of morphological models. *Coastal Engineering*, *51*(8–9), 917–939.

Team, B. A. (2008). *Assessment of climate change for the Baltic Sea basin*. Springer Science & Business Media.

Thorndahl, S., Beven, K., Jensen, J. B., & Schaarup-Jensen, K. (2008). Event based uncertainty assessment in urban drainage modelling, applying the GLUE methodology. *Journal of Hydrology*, *357*(3–4), 421–437.

Tiede, J., Jordan, C., Siewert, M., Sommermeier, K., & Schlurmann, T. (2024). Evolution of beach profiles at the German Baltic Sea during and after large-scale beach nourishment: bar formation and sand redistribution. *Frontiers in Marine Science*, *11*, 1473237.

Vousdoukas, M. I., Mentaschi, L., Voukouvalas, E., Verlaan, M., & Feyen, L. (2017). Extreme sea levels on the rise along Europe's coasts. *Earth's Future*, *5*(3), 304–323.

Walstra, D., Roelvink, J., & Groeneweg, J. (2000). 3D calculation of wave-driven cross-shore currents. *Proceedings 27th International Conference on Coastal Engineering*, 1050–1063.

Walstra, D., Van Rijn, L., Van Ormondt, M., Brière, C., & Talmon, A. (2007). The effects of bed slope and wave skewness on sediment transport and morphology. In *Coastal Sediments' 07: Coastal Sediments' 07* (pp. 137–150).

Weisse, R., Dailidiene, I., Hünicke, B., Kahma, K., Madsen, K., Omstedt, A., Parnell, K., Schöne, T., Soomere, T., Zhang, W., & others. (2021). Sea level dynamics and coastal erosion in the Baltic Sea region. *Earth System Dynamics Discussions*, *2021*, 1–40.

Wolski, T., & Wiśniewski, B. (2021). Characteristics and long-term variability of occurrences of Storm surges in the Baltic Sea. *Atmosphere*, *12*(12), 1679.

Wolski, T., Wiśniewski, B., Giza, A., Kowalewska-Kalkowska, H., Boman, H., Grabbi-Kaiv, S., Hammarklint, T., Holfort, J., & Lydeikaitė, Ž. (2014). Extreme sea levels at selected stations on the Baltic Sea coast. *Oceanologia*, *56*(2), 259–290.

Zeidler, R. B., Wróblewski, A., Miętus, M., Dziadziuszko, Z., & Cyberski, J. (1995). Wind, wave, and storm surge regime at the Polish Baltic coast. *Journal of Coastal Research*, 33–55.

Appendices

Appendix A: Script used for generating LHS samples

```
% Number of LHS samples
N = 50;
% Parameter names and their ranges
param_names = {'facua', 'por', 'gamma', 'gamma2'};
param_min   = [0.0,     0.35,   0.4,    0.0];
param_max   = [1.0,     0.45,   0.9,    0.5];
param_default = [0.175,   0.4,   0.46,   0.34];
% Latin Hypercube Sampling in [0,1]
lhs_unit = lhsdesign(N, numel(param_names));
% Scale to actual parameter ranges
lhs_scaled = lhs_unit .* (param_max - param_min) + param_min;
% Append default values as row 51
lhs_with_default = [lhs_scaled; param_default];
% Convert to table for clarity
T = array2table(lhs_with_default, 'VariableNames', param_names);
% Save to CSV (optional)
writetable(T, 'C:
\Users\khatr\Desktop\Thesis\04_Simulations\lhs_parameter_combinations.csv');
```

Appendix B: Script used for setting up the model

```
% Input
datafolder = 'Z:\02_DATA';
P_name = '_F181495_loop';
simnr  = 'V_01_01';

% path to the simulation folder
folderPath = ['C:\SIMULATIONS\_PNr', num2str(P_name), '\'];
tide_source_path = 'Z:
\10_Modelling\DATA\Bathymetry\V9_Standardprofil\CLEAN\tide.txt';
wave_source_path = 'Z:
\10_Modelling\DATA\Bathymetry\V9_Standardprofil\CLEAN\waves.txt';

% Create base simulation subfolders
mkdir([folderPath, '_PLOTS\']);
grid_dir = [folderPath, '_GRID\'];
mkdir(grid_dir);
mkdir([folderPath, '_DEP\']);

% Define number of simulation runs
numSubfolders = 31;
```

```
% Create run-specific folders
for i = 1:numSubfolders
    runnr = sprintf('01_%03d', i);
    run_dir = ['C:\SIMULATIONS\_PNr', num2str(P_name), '\RUN_', runnr];
    mod_dir = ['C:\SIMULATIONS\_PNr', num2str(P_name)];
    bc_dir = ['C:\SIMULATIONS\_PNr', num2str(P_name), '\RUN_', runnr, '\BC\'];
    destout_plt = ['C:\SIMULATIONS\_PNr', num2str(P_name), '\RUN_', runnr,
'\PLOTS\'];

    mkdir(run_dir);
    mkdir([run_dir, '\CLEAN\']);
    mkdir([run_dir, '\OUTPUT\']);
    mkdir([run_dir, '\Postprocessing\']);
    mkdir(bc_dir);
    mkdir(destout_plt);

    tide_dest_path = fullfile(bc_dir, 'tide.txt');
    copyfile(tide_source_path, tide_dest_path);

    wave_dest_path = fullfile(bc_dir, 'waves.txt');
    copyfile(wave_source_path, wave_dest_path);

    if exist(tide_dest_path, 'file')
        fprintf('Successfully copied tide.txt to %s\n', bc_dir);
    else
        fprintf('Failed to copy tide.txt to %s\n', bc_dir);
    end
end

disp(['Directory structure created under: ', folderPath]);

%% 3-B) - Basic Grid for KKM
P_name = '_F181495';

BdPt1 = 302;  % nearest point to the reference profile
BdPt2 = 305;

BdPts = zeros(2,3);
BdPts(1,:) = [332624.0 6030322.2 BdPt1];
BdPts(2,:) = [333229.0 6030917.9 BdPt2];

% Choose Central Profile
KKM    = readtable([datafolder, '\202310_AH_post-storm_profiles\202310_AH',
num2str(P_name), '.csv']);
Profil = KKM{:,1:3};
```

```
ldb_coords  = zeros(1, 2);
offb_coords = zeros(1, 2);

% For north oriented coastlines (otherwise swap min/max)
[~, idx] = min(Profil(:,2));
ldb_coords(1,:) = Profil(idx,1:2);
ldb_coords(1,1) = Profil(idx,1) - 33000000;

[~, idx] = max(Profil(:,2));
offb_coords(1,:) = Profil(idx,1:2);
offb_coords(1,1) = Profil(idx,1) - 33000000;

Elev_0_2 = table2array(readtable([datafolder
'\Contours\Elevation\Waterline_by_ALS202309_0_2 _mNHN_Pts.csv'], 'ReadVariableNames',
true));

% Check if the profile is still OK
figure; set(gcf, 'Position', [200, 300, 1000, 500]);
plot(ldb_coords(1,1)/1000, ldb_coords(1,2)/1000, 'r*'); hold on;
plot(offb_coords(1,1)/1000, offb_coords(1,2)/1000, 'b*');
plot([ldb_coords(1,1), offb_coords(1,1)]/1000, [ldb_coords(1,2),
offb_coords(1,2)]/1000, 'g-');
plot([offb_coords(1,1), ldb_coords(1,1)]/1000, [offb_coords(1,2),
offb_coords(1,2)]/1000, 'k--');
plot(Elev_0_2(:,2)/1000, Elev_0_2(:,3)/1000, 'b.', 'markersize', 2);
plot(BdPts(:,1)/1000, BdPts(:,2)/1000, 'kx', 'markersize', 5);

% Angle alfa relative to x-axis and cross-shore profile
dx_alf = ldb_coords(1,1) - offb_coords(1,1);
dy_alf = offb_coords(1,2) - ldb_coords(1,2);
alfa   = -360 + rad2deg(atan(dy_alf / dx_alf));
text(gca, ldb_coords(1,1)/1000 + 0.3, ldb_coords(1,2)/1000, ['alfa\' P_name
sprintf(' = %0.2f°', alfa)], 'EdgeColor', 'none');

% Shift towards land boundary
ldb_shift = 50;
dx_x = ldb_shift * sind(-270-alfa);
dx_y = ldb_shift * cosd(-270-alfa);
ldb_coords(1,1) = ldb_coords(1,1) + dx_x;
ldb_coords(1,2) = ldb_coords(1,2) - dx_y;

% Grid characteristics
nx = 52;    % cross-shore cells
ny = 140;   % alongshore cells
```

```
dx = 10;    % cross-shore size
dy = 10;    % alongshore size

% Grid vectors
x = (1:nx+1) * dx;
y = (1:ny+1) * dy;

% Distance of extended origin to initial origin
dy_c = y(end-1)/2 + dy;
dx_c = x(end);

gridcorners = zeros(1, 2);

dx_x  = dx_c * sind(-270-alfa);
dx_y  = dx_c * cosd(-270-alfa);
xori_c = ldb_coords(1,1) - dx_x;
yori_c = ldb_coords(1,2) + dx_y;

dy_x = dy_c * cosd(-270-alfa);
dy_y = dy_c * sind(-270-alfa);

xori  = xori_c - dy_x;
yori  = yori_c - dy_y;
xoffb = xori_c + dy_x;
yoffb = yori_c + dy_y;

plot(xori/1000, yori/1000, 'ro');
plot(xori_c/1000, yori_c/1000, 'g*');
plot([xori_c, ldb_coords(1,1)]/1000, [yori_c, ldb_coords(1,2)]/1000, 'g--');

gridcorners(1,1:2) = [xori, yori];
gridcorners(2,1:2) = [xori_c + dy_x, yori_c + dy_y];
gridcorners(3,1:2) = [ldb_coords(1,1) + dy_x, ldb_coords(1,2) + dy_y];
gridcorners(4,1:2) = [xori + dx_x, yori - dx_y];
gridcorners(5,1:2) = [xori, yori];

plot(gridcorners(:,1)/1000, gridcorners(:,2)/1000);
hold off;

title('Profile Orientation');
xlabel('X-Coordinate (km)');
ylabel('Y-Coordinate (km)');
legend('Land-Points','Offshore-Points','Profile','alfa=0°','Coastline (0.2 m
üNHN)','BdPts MIKE21','location','northwest');
axis equal; grid minor;
```

```
print(gcf, [folderPath, '_PLOTS\' , sprintf('_Matlab_Base_Axis.png')], '-dpng', '-
r300');

disp(['Plot Base Grid for KKM ', P_name, ' complete!']);
profile_length = sqrt(dx^2 + dy^2);
fprintf('Length of profile %s: %.2f meters\n', P_name, profile_length);

% Load measured bathymetry
bathy_file = fullfile(datafolder, 'Bathymetrie_V7_EOMAP202210_ALS202310.csv');
bathy_data = readmatrix(bathy_file);

bathy = zeros(size(bathy_data,1), 3);
bathy(:,1) = bathy_data(:,2);
bathy(:,2) = bathy_data(:,3);
bathy(:,3) = bathy_data(:,1);
fprintf('\nLoad Measured Bathymetry complete!\n');

%% Settings for Profile (local transform)
bathy_t = [bathy(:,1) - xori, bathy(:,2) - yori, bathy(:,3)];
bathy_r = [ ...
    bathy_t(:,1)*cosd(alfa) - bathy_t(:,2)*sind(alfa), ...
    bathy_t(:,1)*sind(alfa) + bathy_t(:,2)*cosd(alfa), ...
    bathy(:,3) ...
];
fprintf('\nTranslation and Rotation of Grid Origin complete!\n');

%% Construct rectangular grid and interpolate
x = (1:nx+1) * dx;
y = (1:ny+1) * dy;
[x, y] = meshgrid(x, y);

invalidIdx = ~isfinite(bathy_r(:,1)) | ~isfinite(bathy_r(:,2)) |
~isfinite(bathy_r(:,3));
bathy_r_clean = bathy_r(~invalidIdx, :);
disp(['Removed values: ', num2str(sum(invalidIdx))]);

XY = round(bathy_r_clean(:,1:2), 6);
Z  = bathy_r_clean(:,3);
[uniqueXY, ~, ic] = unique(XY, 'rows');
Z_avg = accumarray(ic, Z, [], @mean);

z = griddata(uniqueXY(:,1), uniqueXY(:,2), Z_avg, x, y);
fprintf('\nConstruction of Grid complete!\n');

%% Plot measured bathymetry (2D/3D)
```

```
figure; set(gcf, 'Position', [1000, 100, 600, 800]);
pcolor(x, y, z); shading interp; colormap(jet);
cb = colorbar; cb.Label.String = 'Elevation (m üNHN)'; cb.Label.FontSize = 16;
cb.FontSize = 12;
title(sprintf('measured bathymetry KKM\\%s (2D)\n', P_name));
xlabel('x (m)'); ylabel('y (m)'); zlabel('z (m ü NHN)');
set(gca,'YTick', x(1,1):100:y(end,1), 'TickDir','out'); axis equal;
print(gcf, [folderPath, '_PLOTS\', sprintf('Bathy2D_measured_KKM%s_dx_%d_m.png',
P_name, dx)], '-dpng', '-r300');

figure; set(gcf, 'Position', [1000, 300, 1100, 500]);
surf(x, y, z, 'EdgeColor', 'none'); colormap(jet);
cb = colorbar(); cb.Label.String = 'Elevation (m üNHN)'; cb.Label.FontSize = 16;
cb.FontSize = 12;
title(sprintf('measured bathymetry KKM\\%s (3D)\n', P_name));
xlabel('x (m)'); ylabel('y (m)'); zlabel('z (m ü NHN)');
print(gcf, [folderPath, '_PLOTS\' ,
sprintf('Bathy3D_measured_KKM%s_dx_%d_original_length_m.png', P_name, dx)], '-dpng',
'-r300');
fprintf('\nPlot of 2D and 3D coarse bathymetry complete!\n');

%% Cross-shore varying grid
mn_y  = round(0.5 * numel(x(:,1)));
dxmin = 2;
[xgr, zgr] = xb_grid_xgrid(x(mn_y,:), z(mn_y,:),
{'CFL',0.7,'Tm',10,'dxmin',dxmin,'vardx',1});

% Mean sea level
MW = zeros(1, numel(xgr));
MW(1, :) = 5.07 - 4.98;

f1 = @(xx) interp1(xgr, zgr, xx);
f2 = @(xx) interp1(xgr, MW,  xx);

st_val = 400.;
schnittpunkt_x = fzero(@(xx) f1(xx) - f2(xx), st_val);
schnittpunkt_y = f1(schnittpunkt_x); %#ok<NASGU>
[~, index_x1] = min(abs(xgr - schnittpunkt_x));
fprintf('\nCross-Shore Varying Grid complete!\n');

figure; set(gcf, 'Position', [1000, 300, 1000, 500]);
plot(x(mn_y,:), z(mn_y,:), 'b*'); hold on;
plot(xgr, zgr, 'r-o');
plot(xgr(1:index_x1), MW(1:index_x1), 'b-');
title(sprintf('cross-shore profile grid fitting KKM\\%s', P_name));
```

```
xlabel('crossshore distance (m)'); ylabel('elevation (m üNHN)');
ylim([-12, 7]); set(gca,'Fontsize',12);
legend('original','fitted','MSL','location','northwest'); grid minor;
print(gcf, [folderPath, '_PLOTS\' ,
sprintf('_Matlab_Grid_Fitting_KKM%s_dxmin_%d_m_original.png', P_name, dxmin)], '-
dpng', '-r300');

%% Longshore varying grid
dymin = 2;
ygr = xb_grid_ygrid(y(:,5), 'dymin', dymin, 'dymax', dy, 'area_size', 0.2);

% Interpolate bathymetry to new grid, translate to a grid
[x_neu, y_neu] = meshgrid(xgr, ygr);
z_neu = griddata(bathy_r_clean(:,1), bathy_r_clean(:,2), bathy_r_clean(:,3), x_neu,
y_neu);
bathy_r2 = interp2(x_neu, y_neu, z_neu, xgr, ygr');
mn_y_neu = round(0.5*numel(x_neu(:,1)));

figure; set(gcf, 'Position', [1000, 300, 1000, 500]);
plot(x(mn_y,:), z(mn_y,:), 'b*'); hold on;
plot(xgr, zgr, 'r-o');
plot(x_neu(mn_y_neu,:), z_neu(mn_y_neu,:), 'g-o');
plot(xgr(1:index_x1), MW(1:index_x1), 'b-');
title(sprintf('cross-shore profile grid fitting (retrofit) KKM\\%s', P_name));
xlabel('crossshore distance (m)'); ylabel('elevation (m üNHN)');
ylim([-12, 7]); set(gca,'Fontsize',12);
legend('original','fitted old','fitted new','MSL','location','northwest'); grid
minor;
print(gcf, [folderPath, '_PLOTS\',
sprintf('_Matlab_Grid_Fitting_KKM%s_dxmin_%d_m_retrofit.png', P_name, dxmin)], '-
dpng', '-r300');
fprintf('\nRetrofitted Grid complete!\n');

%% Size-varying grid to mesh
[xgr, ygr] = meshgrid(xgr, ygr);

figure; set(gcf, 'Position', [1000, 100, 600, 800]);
pcolor(xgr, ygr, bathy_r2); colormap(jet);
cb = colorbar; cb.Label.String = 'Elevation (m üNHN)'; cb.Label.FontSize = 16;
cb.FontSize = 12;
title(sprintf('measured bathymetry with (size varying) grid KKM\\%s (2D)', P_name));
xlabel('x (m)'); ylabel('y (m)');
ylim([0, ygr(end,1)]); set(gca,'TickDir','out'); axis equal;
print(gcf, [folderPath, '_PLOTS\', sprintf('Bathy2D_GridVar_KKM%s_dxmin_%d.png',
P_name, dxmin)], '-dpng', '-r300');
```

```
figure; set(gcf, 'Position', [1000, 300, 1100, 500]);
surf(xgr, ygr, bathy_r2, 'EdgeColor', 'none'); colormap(jet);
cb = colorbar(); cb.Label.String = 'Elevation (m üNHN)'; cb.Label.FontSize = 16;
cb.FontSize = 12;
title(sprintf('measured bathymetry with (size varying) grid KKM\\%s (3D)', P_name));
xlabel('x (m)'); ylabel('y (m)'); zlabel('z (m üNHN)');
print(gcf, [folderPath, '_PLOTS\', sprintf('Bathy3D_GridVar_KKM%s_dxmin_%d_new.png',
P_name, dxmin)], '-dpng', '-r300');
fprintf('\nSize-varying bathymetry plots complete!\n');

%% Finalise model domain
ny_extd = 3;
slope   = 1/20;

[X, Y, Z] = xb_grid_finalise2(xgr, ygr, bathy_r2, 'actions', {'seaward_flatten'},
'slope', slope);
fprintf('\nseaward_flatten slope=%d (%d, %d)\n', slope, size(X));

zmin = -20;
[X, Y, Z] = xb_grid_finalise2(X, Y, Z, 'actions', {'seaward_extend'}, 'zmin', zmin,
'slope', slope);
fprintf('\nseaward_extend zmin=%d (%d, %d)\n', zmin, size(X));

[X, Y, Z] = xb_grid_finalise2(X, Y, Z, 'actions', {'lateral_extend'}, 'n', ny_extd);
fprintf('\nlateral_extend n=%d (%d, %d)\n', ny_extd, size(X));

% Plot extended bathymetry
figure; set(gcf, 'Position', [1000, 100, 600, 800]);
pcolor(X, Y, Z); colormap(jet);
cb = colorbar; cb.Label.String = 'Elevation (m üNHN)'; cb.FontSize = 16;
title(sprintf('extended bathymetry KKM\\%s with grid', P_name));
xlabel('x (m)'); ylabel('y (m)');
ylim([Y(1,1), Y(end,1)]); set(gca,'TickDir','out'); axis equal;
print(gcf, [folderPath, '_PLOTS\', sprintf('Bathy2D_Extd_KKM%s.png', P_name)], '-
dpng', '-r300');

figure; set(gcf, 'Position', [1000, 300, 1100, 500]);
surf(X, Y, Z, 'EdgeColor', 'none'); colormap(jet);
cb = colorbar; cb.Label.String = 'Elevation (m üNHN)'; cb.FontSize = 16;
title(sprintf('extended bathymetry KKM\\%s', P_name));
xlabel('x (m)'); ylabel('y (m)'); zlabel('z (m üNHN)');
print(gcf, [folderPath, '_PLOTS\', sprintf('Bathy3D_Extd_KKM%s_orginal.png',
P_name)], '-dpng', '-r300');
fprintf('\nExtended bathymetry plots complete!\n');
```

```
%% New origin considering extension
dy_extd = ygr(end,1) - ygr(end-1,1);
dx_extd = X(1,2) - X(1,1);
nx_extd = size(X, 2) - size(xgr, 2);

dy_ori = (ny_extd-2) * dy_extd;
dx_ori = (nx_extd-0) * dx_extd - dx;

delta_x_y = dy_ori * cosd(-270-alfa);
delta_y_y = dy_ori * sind(-270-alfa);

xori_y = xori - delta_x_y;
yori_y = yori - delta_y_y;

delta_x_x = dx_ori * sind(-270-alfa);
delta_y_x = dx_ori * cosd(-270-alfa);

xori_ext = xori_y - delta_x_x;
yori_ext = yori_y + delta_y_x;

x_offb_ext = xori_ext + delta_x_y*2 + (2*dy_extd + dy * ny) * cosd(-270-alfa);
y_offb_ext = yori_ext + delta_y_y*2 + (2*dy_extd + dy * ny) * sind(-270-alfa);

figure;
plot(xori/1000, yori/1000, 'b*'); hold on;
plot(xori_y/1000, yori_y/1000, 'r*');
plot(xori_ext/1000, yori_ext/1000, 'k*');
plot(x_offb_ext/1000, y_offb_ext/1000, 'g*');
plot([xori/1000, xori_y/1000], [yori/1000, yori_y/1000], 'b-');
plot([xori_ext/1000, x_offb_ext/1000], [yori_ext/1000, y_offb_ext/1000], 'g-');
plot(BdPts(:,1)/1000, BdPts(:,2)/1000, 'kx', 'markersize', 5);
plot(ldb_coords(1,1)/1000, ldb_coords(1,2)/1000, 'r*');
plot(offb_coords(1,1)/1000, offb_coords(1,2)/1000, 'b*');
plot([ldb_coords(1,1), offb_coords(1,1)]/1000, [ldb_coords(1,2),
offb_coords(1,2)]/1000, 'g-');
plot([offb_coords(1,1), ldb_coords(1,1)]/1000, [offb_coords(1,2),
offb_coords(1,2)]/1000, 'k--');
plot(gridcorners(:,1)/1000, gridcorners(:,2)/1000);
plot(Elev_0_2(:,2)/1000, Elev_0_2(:,3)/1000, 'b.', 'markersize', 2);

ly_grd = abs(Y(1,1) - Y(end,1));
delta_x_y_ly = ly_grd * cosd(-270-alfa);
delta_y_y_ly = ly_grd * sind(-270-alfa);
```

```
xori_ly = xori_y + delta_x_y_ly;
yori_ly = yori_y + delta_y_y_ly;

plot([xori_y/1000, xori_ly/1000], [yori_y/1000, yori_ly/1000], 'm--');

y_shift = 1/2 * (sqrt((xori_ly-gridcorners(2,1))^2 + (yori_ly-gridcorners(2,2))^2) -
dy_ori);
fprintf('\nShift = %d\n', y_shift);

delta_x_y_cor = y_shift * cosd(-270-alfa);
delta_y_y_cor = y_shift * sind(-270-alfa);

xori_cor = xori_ext - delta_x_y_cor;
yori_cor = yori_ext - delta_y_y_cor;

plot([xori_ext/1000, xori_cor/1000], [yori_ext/1000, yori_cor/1000], 'b-');
legend('origin left','lateral ext. origin','seaward ext. origin','','','seaward ext.
boundary','MIKE21 BdPts');
axis equal; grid on; hold off;

% Write origin points
ori_pts = ['Ori_points_', simnr,'_', sprintf('%s_new', P_name), '.txt'];
fid = fopen([folderPath, '_GRID\', ori_pts], 'w');
fprintf(fid, '%f %f\n', xori, yori);
fprintf(fid, '%f %f\n', xori_y, yori_y);
fprintf(fid, '%f %f\n', xori_ext, yori_ext);
fprintf(fid, '%f %f\n', x_offb_ext, y_offb_ext);
fprintf(fid, '%f %f\n', xori_cor, yori_cor);
fclose(fid);

title('Final Grid Orientation');
xlabel('X-Coordinate (km)');
ylabel('Y-Coordinate (km)');
axis equal; grid minor;
print(gcf, [folderPath, '_PLOTS\',
sprintf('Grid_2D_Final_Orientation_KKM%s_original.png', P_name)], '-dpng', '-r300');
fprintf('\nOri_points.txt created successfully.\n');


%% for writing params.txt file
datafolder = 'Z:\02_DATA';
P_name     = '_F181495_loop';
simnr      = 'V_01_01';
% Fixed parameters (constant for all runs)
morfac = 15;
```

```
dtheta = 10;
% --- Parameter defaults used for variation
facua0  = 0.175;
gamma0  = 0.46;
gamma20 = 0.34;

% --- Source BC directory (must contain tide.txt, waves.txt, etc.)
% TODO: set this to your master BC path
bc_src_dir = 'Z:\10_Modelling\DATA\BC\_Sim_V8_05_Storm_20231020\_PNr_F181495_V8_05';
% --- Base simulation directories
base_dir = ['C:\SIMULATIONS\_PNr', P_name];

% Run index: 1 to 31
for i = 1:31
    % ---------------------------------------------------------------------
    % Compute run identifier and folders
    runnr   = sprintf('01_%03d', i);
    run_dir = fullfile(base_dir, ['RUN_', runnr]);
    clean_dir = fullfile(run_dir, 'CLEAN');
    bc_dir  = fullfile(run_dir, 'BC');  % run-specific BC location

    % Create directories if needed
    if ~exist(run_dir, 'dir'),  mkdir(run_dir);  end
    if ~exist(clean_dir, 'dir'), mkdir(clean_dir); end
    if ~exist(bc_dir, 'dir'),   mkdir(bc_dir);   end

    % ---------------------------------------------------------------------
    % Copy BCs into the run before reading tide
    if ~exist(bc_src_dir, 'dir')
        error('bc_src_dir does not exist: %s', bc_src_dir);
    end
    % Copy all files from bc_src_dir to bc_dir
    copyfile(fullfile(bc_src_dir, '*'), bc_dir);

    % ---------------------------------------------------------------------
    % Read tide after BCs are available in the run
    tide_path = fullfile(bc_dir, 'tide.txt');
    if ~exist(tide_path, 'file')
        error('Missing tide.txt in %s', tide_path);
    end
    tide  = readtable(tide_path);
    tstop = max(tide{:,1});
    zs0   = 0.1;

    % ---------------------------------------------------------------------
```

```
    % Start from defaults each run (one-at-a-time variation philosophy)
    facua  = facua0;
    gamma  = gamma0;
    gamma2 = gamma20;

    % Piecewise schedule (percent deviations)
    if i >= 1 && i <= 7
        pct = [-5, -10, +3, +4, +5, +6, +7];
        facua = facua0 * (1 + pct(i)/100);

    elseif i >= 8 && i <= 11
        pct = [1, 2, 3, 4];
        gamma = gamma0 * (1 - pct(i-7)/100);

    elseif i >= 12 && i <= 15
        pct = [1, 2, 3, 4];
        facua = facua0 * (1 - pct(i-11)/100);

    elseif i >= 16 && i <= 19
        pct = [1, 2, 3, 4];
        gamma2 = gamma20 * (1 - pct(i-15)/100);

    elseif i >= 20 && i <= 25
        pct = [11, 12, 13, 14, 15, 16];
        gamma2 = gamma20 * (1 + pct(i-19)/100);

    elseif i >= 26 && i <= 30
        pct = [1, 2, 3, 4, 5];
        gamma = gamma0 * (1 + pct(i-25)/100);

    elseif i == 31
        % all defaults
    end

    % --- Truncate (not round) to 4 decimals to reproduce your table exactly
    facua  = floor(facua  * 1e4) / 1e4;
    gamma  = floor(gamma  * 1e4) / 1e4;
    gamma2 = floor(gamma2 * 1e4) / 1e4;

    fprintf('RUN_%s → facua=%.4f, gamma=%.4f, gamma2=%.4f\n', runnr, facua, gamma,
gamma2);

    % ------------------------------------------------------------------------
    % Create bathymetry (assumes X, Y, Z in workspace)
    bathymetry = xb_grid_add('x', X, 'y', Y, 'z', Z, 'posdwn', 1);
```

```
    % Generate model parameters
    pars = xb_generate_settings( ...
        'xori', xori_cor, 'yori', yori_cor, 'alfa', -alfa, ...
        'wavemodel', 'surfbeat', ...
        'vardx', 1, 'epsi', -1, ...
        'gamma', gamma, ...
        'gamma2', gamma2, ...
        'nmax', 0.8, ...
        'front', 1, ...
        'lateralwave', 'neumann', 'cyclic', 1, ...
        'cyclicdiradjust', 1, 'back', 'abs_2d', ...
        'thetanaut', 1, 'thetamin', 220, 'thetamax', 20, ...
        'dtheta', dtheta, 'single_dir', 0, 'snells', 0, ...
        'wbctype', 'jonstable', 'bcfile', 'waves.txt', ...
        'zs0', zs0, 'tideloc', 1, 'zs0file', 'tide.txt', ...
        'sedtrans', 1, 'morphology', 1, ...
        'facua', facua, ...
        'morfacopt', 1, 'morfac', morfac, 'morstart', 900, ...
        'wetslp', 0.15, 'dryslp', 2, ...
        'D50', 0.00026, 'D90', 0.00045, 'por', 0.4, ...
        'bedfriccoef', 0.01, 'hswitch', 0.1, ...
        'outputformat', 'netcdf', ...
        'nglobalvar',
{'H','u','v','zs','zb','hh','theta','theta0','Susg','Svsg','sedero'}, ...
        'nmeanvar', {'H', 'zs', 'u', 'v', 'zb', 'hh'}, ...
        'tintg', 600, 'tintm', 3600, ...
        'tstart', 0, 'tstop', tstop, ...
        'npointvar', {'zs','u','v','zb'}, ...
        'npoints', {sprintf('%f %f', offb_coords(1,1), offb_coords(1,2)), ...
                    sprintf('%f %f', BdPts(1,1), BdPts(1,2))} );

    % Write model input
    xbm_si = xs_join(bathymetry, pars);
    xb_write_input(fullfile(clean_dir, 'params.txt'), xbm_si);
    copyfile(fullfile(bc_dir, '*'), clean_dir);
    fprintf(' RUN_%s created → facua = %.4f, gamma = %.4f, gamma2 = %.4f\n', runnr,
facua, gamma, gamma2);
end
```

Appendix C: Parameter Combinations obtained from Latin Hypercube Sampling

Table C.1: Generated values of LHS-based Parameter Combinations Used in the study

Run	facua	gamma	gamma2	por
001	0.175	0.46	0.34	0.4
002	0.188	0.606	0.112	0.362
003	0.002	0.417	0.07	0.421
004	0.073	0.837	0.163	0.36
005	0.109	0.427	0.435	0.361
006	0.036	0.635	0.089	0.364
007	0.238	0.71	0.027	0.4
008	0.034	0.776	0.255	0.394
009	0.175	0.641	0.07	0.389
010	0.172	0.448	0.227	0.434
011	0.115	0.491	0.054	0.406
012	0.204	0.432	0.418	0.415
013	0.124	0.821	0.188	0.398
014	0.331	0.534	0.283	0.382
015	0.009	0.809	0.344	0.373
016	0.201	0.665	0.334	0.449
017	0.136	0.573	0.38	0.374
018	0.144	0.529	0.134	0.431
019	0.024	0.46	0.047	0.399
020	0.241	0.557	0.325	0.376
021	0.192	0.561	0.101	0.41
022	0.278	0.675	0.45	0.352
023	0.288	0.851	0.122	0.358
024	0.098	0.816	0.407	0.444
025	0.078	0.861	0.143	0.441
026	0.126	0.695	0.201	0.434
027	0.255	0.871	0.303	0.442
028	0.062	0.659	0.465	0.417
029	0.156	0.488	0.097	0.428
030	0.02	0.783	0.494	0.42
031	0.05	0.736	0.427	0.369
032	0.245	0.71	0	0.392
033	0.307	0.586	0.446	0.429
034	0.32	0.617	0.36	0.35

035	0.323	0.476	0.273	0.407
036	0.221	0.508	0.173	0.384
037	0.067	0.408	0.15	0.355
038	0.049	0.894	0.031	0.386
039	0.283	0.764	0.242	0.437
040	0.269	0.888	0.358	0.412
041	0.212	0.621	0.292	0.423
042	0.265	0.599	0.215	0.447
043	0.085	0.728	0.477	0.379
044	0.3	0.755	0.195	0.424
045	0.346	0.682	0.482	0.439
046	0.148	0.749	0.015	0.384
047	0.091	0.461	0.237	0.403
048	0.161	0.846	0.376	0.414
049	0.229	0.799	0.398	0.394
050	0.31	0.543	0.266	0.367
051	0.342	0.517	0.318	0.371

Appendix D: Typical example of a `params.txt` file

```
%%%%%%%%%%%%%%%%%%%%%%%%%%%%%%%%%%%%%%%%%%%%%%%%%%%%%%%%%%%%%%%%%%%%%%%%%%%%%%%%
%%% XBeach parameter settings input file                                     %%%
%%%                                                                          %%%
%%% date:     13-Aug-2025 17:02:02                                           %%%
%%% function: xb_write_params                                                %%%
%%%%%%%%%%%%%%%%%%%%%%%%%%%%%%%%%%%%%%%%%%%%%%%%%%%%%%%%%%%%%%%%%%%%%%%%%%%%%%%%

%%% Bed composition parameters %%%%%%%%%%%%%%%%%%%%%%%%%%%%%%%%%%%%%%%%%%%%%%%%%

por             = 0.400000
D50             = 0.000260
D90             = 0.000450

%%% Flow boundary condition parameters %%%%%%%%%%%%%%%%%%%%%%%%%%%%%%%%%%%%%%%%%

front           = 1
back            = abs_2d
epsi            = -1

%%% General %%%%%%%%%%%%%%%%%%%%%%%%%%%%%%%%%%%%%%%%%%%%%%%%%%%%%%%%%%%%%%%%%%%%

bedfriccoef     = 0.010000
cyclic          = 1
```

```
cyclicdiradjust = 1
single_dir      = 0
snells          = 0
wavemodel       = surfbeat
wbctype         = jonstable

%%% Grid parameters %%%%%%%%%%%%%%%%%%%%%%%%%%%%%%%%%%%%%%%%%%%%%%%%%%%%%%%%%%%%

depfile         = bed.dep
posdwn          = 1
nx              = 176
ny              = 286
alfa            = 310.390101
vardx           = 1
xfile           = x.grd
yfile           = y.grd
xori            = 332086.093643
yori            = 6029838.576101
thetamin        = 220
thetamax        = 20
dtheta          = 14
thetanaut       = 1

%%% Initial conditions %%%%%%%%%%%%%%%%%%%%%%%%%%%%%%%%%%%%%%%%%%%%%%%%%%%%%%%%

zs0             = 0.100000

%%% Model time %%%%%%%%%%%%%%%%%%%%%%%%%%%%%%%%%%%%%%%%%%%%%%%%%%%%%%%%%%%%%%%

tstop           = 72000

%%% Morphology parameters %%%%%%%%%%%%%%%%%%%%%%%%%%%%%%%%%%%%%%%%%%%%%%%%%%%%

morfac          = 15
morfacopt       = 1
morstart        = 900
wetslp          = 0.150000
dryslp          = 2
hswitch         = 0.100000

%%% Physical processes %%%%%%%%%%%%%%%%%%%%%%%%%%%%%%%%%%%%%%%%%%%%%%%%%%%%%%%

sedtrans        = 1
morphology      = 1
```

```
%%% Sediment transport parameters %%%%%%%%%%%%%%%%%%%%%%%%%%%%%%%%%%%%%%%%%%%%%%

facua           = 0.175000

%%% Tide boundary conditions %%%%%%%%%%%%%%%%%%%%%%%%%%%%%%%%%%%%%%%%%%%%%%%%%%%

zs0file         = tide.txt
tideloc         = 1

%%% Wave boundary condition parameters %%%%%%%%%%%%%%%%%%%%%%%%%%%%%%%%%%%%%%%%%

nmax            = 0.800000
lateralwave     = neumann

%%% Wave breaking parameters %%%%%%%%%%%%%%%%%%%%%%%%%%%%%%%%%%%%%%%%%%%%%%%%%%%

gamma           = 0.600000
gamma2          = 0.340000

%%% Wave-spectrum boundary condition parameters %%%%%%%%%%%%%%%%%%%%%%%%%%%%%%%%

bcfile          = waves.txt

%%% Output variables %%%%%%%%%%%%%%%%%%%%%%%%%%%%%%%%%%%%%%%%%%%%%%%%%%%%%%%%%%%

outputformat    = netcdf
tintm           = 3600
tintg           = 600
tstart          = 0

nglobalvar      = 11
H
u
v
zs
zb
hh
theta
theta0
Susg
Svsg
sedero

nmeanvar        = 6
H
```

```
zs
u
v
zb
hh

npointvar       = 4
zs
u
v
zb

npoints         = 2
333125.789000 6029743.074000
332624.000000 6030322.200000
```

Appendix E: Overview of simulation runs when facua, gamma and gamma2 were varied

Table E.1: Overview of simulation runs when facua, gamma and gamma2 were varied

run	facua	gamma	gamma2	BSS	Erosion (m^3/m)	Accretion (m^3/m)
001	0.166	0.46	0.34	0.5608	7.3997	1.8353
002	0.158	0.46	0.34	0.6145	7.8217	2.056
003	0.18	0.46	0.34	0.561	5.6824	2.7341
004	0.182	0.46	0.34	0.5204	6.2173	2.4681
005	0.184	0.46	0.34	0.5835	6.0317	2.6718
006	0.186	0.46	0.34	0.4445	6.3512	2.2407
007	0.187	0.46	0.34	0.4921	5.9141	2.7757
009	0.175	0.4554	0.34	0.551	6.822	2.0649
010	0.175	0.4508	0.34	0.5553	6.7809	2.0582
011	0.175	0.4463	0.34	0.5182	7.0254	1.9612
012	0.175	0.4419	0.34	0.5338	6.9979	1.95
013	0.173	0.46	0.34	0.5786	6.5055	2.444
014	0.172	0.46	0.34	0.5636	7.152	2.0686
015	0.17	0.46	0.34	0.6021	7.1352	2.2444
016	0.168	0.46	0.34	0.5917	6.9751	2.1201
017	0.175	0.46	0.3366	0.5589	6.693	2.2418
018	0.175	0.46	0.3332	0.5426	6.9332	1.8757
019	0.175	0.46	0.3299	0.538	6.9229	2.0064
020	0.175	0.46	0.3266	0.5301	7.1503	1.8096
021	0.175	0.46	0.3774	0.5312	6.7896	2.3439

022	0.175	0.46	0.3808	0.6126	6.5821	2.4217
023	0.175	0.46	0.3842	0.5384	6.882	2.0297
024	0.175	0.46	0.3876	0.5214	7.0577	1.9026
025	0.175	0.46	0.391	0.504	7.2091	1.8652
026	0.175	0.46	0.3944	0.6411	6.6525	2.4651
027	0.175	0.4646	0.34	0.5872	6.3332	2.3428
028	0.175	0.4692	0.34	0.5655	6.4991	1.9772
029	0.175	0.4738	0.34	0.5975	6.2412	2.4028
030	0.175	0.4784	0.34	0.5525	6.8857	1.8973
031	0.175	0.483	0.34	0.5486	7.1172	1.8872

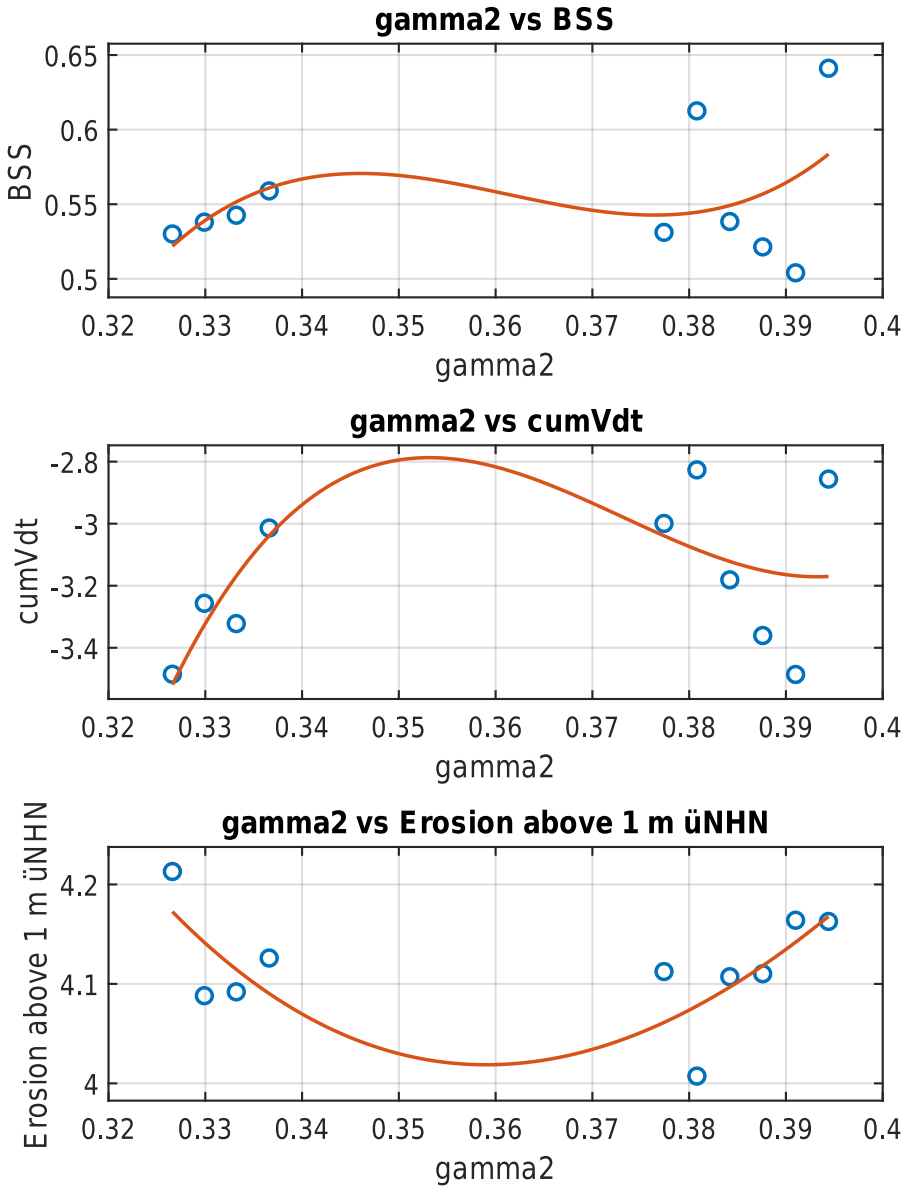

Figure E.1: Relationship between BSS and variation of input Parameters

Appendix F: Change of morfac to 20

Table F.1: Overview of simulation runs for morfac value of 20

run	facua	gamma	gamma2	BSS	RMSE	cumVdt
001	0.14	0.6	0.38	0.753	0.19	−2.947
002	0.142	0.6	0.38	0.754	0.19	−2.754
003	0.144	0.6	0.38	0.801	0.171	−2.128
004	0.146	0.6	0.38	0.764	0.186	−2.921
005	0.148	0.6	0.38	0.786	0.177	−2.469
006	0.15	0.6	0.38	0.771	0.183	−2.883
007	0.152	0.6	0.38	0.766	0.185	−3.067
008	0.154	0.6	0.38	0.808	0.168	−2.08
009	0.156	0.6	0.38	0.801	0.171	−2.558
010	0.158	0.6	0.38	0.787	0.176	−2.674
011	0.16	0.6	0.38	0.793	0.174	−2.528
012	0.14	0.6	0.39	0.772	0.183	−2.684
013	0.142	0.6	0.39	0.771	0.183	−2.626
014	0.144	0.6	0.39	0.785	0.177	−2.471
015	0.146	0.6	0.39	0.795	0.173	−2.369
016	0.148	0.6	0.39	0.796	0.173	−2.438
017	0.15	0.6	0.39	0.75	0.191	−3.234
018	0.152	0.6	0.39	0.786	0.177	−2.844
019	0.154	0.6	0.39	0.789	0.176	−2.796
020	0.156	0.6	0.39	0.799	0.172	−2.406
021	0.158	0.6	0.39	0.793	0.174	−2.402
022	0.16	0.6	0.39	0.795	0.173	−2.35
023	0.14	0.6	0.4	0.786	0.177	−2.385
024	0.142	0.6	0.4	0.794	0.174	−2.218
025	0.144	0.6	0.4	0.776	0.181	−2.594
026	0.146	0.6	0.4	0.786	0.177	−2.644
027	0.148	0.6	0.4	0.785	0.178	−2.711
028	0.15	0.6	0.4	0.76	0.188	−2.911
029	0.152	0.6	0.4	0.799	0.171	−2.625
030	0.154	0.6	0.4	0.79	0.175	−2.644

Appendix G: Overview of the Simulations for varying dtheta

Table G.1: Overview of simulation scenario for variation of dtheta

Run	BSS	Accretion(m^3/m)	Erosion above 1m üNHN (m^3/m)	dtheta(in degree)
001	0.3924	2.5313	6.6049	20
002	0.63	4.3678	6.2063	18
003	0.7954	5.949	5.6507	16
004	0.7807	7.9439	3.6661	14
005	0.7475	13.0172	3.124	12
006	0.7438	12.1438	3.1884	10
007	0.5593	10.2882	1.3465	8
008	0.7314	7.6728	3.4175	6
009	0.7214	6.9038	3.6355	4
010	0.6468	13.1443	2.5242	2

Appendix H: Results after varying angle of wave incidence (theta)

Table H.1: Overview of simulation scenario for variation of wave incidence angle theta

Run	Erosion(m^3/m)	Accretion(m^3/m)	Erosion > 1m üNHN (m^3/m)	theta (in degree)
093	36.7497	49.4111	35.42	−60
094	40.0466	57.4342	38.756	−50
095	43.7845	46.7115	42.68	−40
096	41.2264	49.1235	40.0668	−30
097	38.152	44.4046	37.0365	−25
098	36.7103	40.6213	36.0922	−20
099	34.5114	38.9944	34.1367	−15
100	28.8205	36.2764	27.983	−10
101	26.694	39.0523	26.1134	−5
102	26.3109	46.9882	25.7213	0
103	26.555	50.1081	25.8203	5
104	29.4149	41.66	28.3629	10
105	32.4027	43.0863	32.542	15
106	37.8979	48.5716	36.7462	20
107	43.8246	42.1823	43.6415	25
108	38.483	52.4026	37.365	30
109	47.1173	63.0113	46.7056	40
110	44.5781	64.8589	43.7548	50
111	40.7231	66.444	39.9378	60